Phase-Engineered Field-Effect Transistors Based on Two-Dimensional Transition Metal Dichalcogenides

A Dissertation
SUBMITTED TO THE FACULTY OF
UNIVERSITY OF MINNESOTA
BY

Rui Ma

IN PARTIAL FULFILLMENT OF THE REQUIREMENTS
FOR THE DEGREE OF DOCTOR OF PHILOSOPHY

Professor Steven J. Koester

August 2020

ACKNOWLEDGEMENTS

The completion of my dissertation would not have been possible without the support and nurturing of a lot of people. First of all, I would like to express my deepest appreciation to my advisor, Professor Steven Koester, for his unparalleled support and profound belief in my abilities. He has inspired me to become an independent researcher and gave me freedom to pursue my own research interests and explore ideas. He also helped me develop a solid knowledge in semiconductor devices, useful experimental skills, and professional verbal and written communication skills. I could not have asked for a better advisor.

I would also like to extend my gratitude to the members of my committee, Professors Stephen Campbell, Tony Low, Chris Leighton, and Sachin Sapatnekar for generously giving their time, support, and valuable comments throughout the review of this dissertation. In particular, Professor Tony Low along with his student Javad Azadani have done great theoretical work to support my research.

I am also grateful to the collaborators for lending me their expertise. My work could never have gotten this far without mentioning Professor James Johns and his students Professor Youngdong Yoo and Dr. Zach DeGregorio, who had developed a synthesis method for the fabrication of two-dimensional lateral TMDC junctions, which has been the core of my research. I must also thank Dr. Huairuo Zhang, Dr. Albert Davydov, and Dr. Leonid Bendersky at NIST for their excellent TEM/STEM work, which added valuable insights to my work. To all other collaborators, I very much appreciate your contribution.

Thanks should also go to my fellow group members. It was a great delight to have been a member of Koester NanoDevice Laboratory. The group has been filled with brilliant and kind people who inspired me over the years. Dr. Eric Olson directly mentored me in my first year and made my initial transition to the field successful. Other senior members Dr. Nazila Haratipour, Dr. Yang Su, Dr. Yulong Li, Dr. Chaitanya Kshirsager, Dr. Yoska Anugrah, and Dr. Mona Ebrish always taught me numerous experiment skills I needed throughout my graduate studies. Peers Dr. Matthew Robbins, Dr. Jiaxi Hu, and Dr. Yao Zhang have encouraged me and helped my research through collaboration and conversation. The interactions with the postdocs Dr. Jing Li, Dr. Seon Namgung, Dr. Mahmoud Atalla, and Dr. Sandhaya Koirala have also been very beneficial and pleasant. I would also like to thank the recently graduated and current members of the group: Dr. Saran Chaganti, Dr. Andrew Stephen, Lun Jin, Qun Su, Praful Golani, Jiaxuan Wen, Nyssa Capman, Prakash Sundaram, Dr. Dongjea Seo, Chin Hsiang Liao, and Ruixue Li for their help and support. I express special thanks to Lun Jin for his help synthesizing the materials that were needed throughout my work.

Finally, I wish to thank my friends, family, and host family in Minnesota for their support, unconditional trust, and constant encouragement. Special thanks to my parents, without whom I would not have enjoyed so many opportunities.

DEDICATION

This dissertation is dedicated to my academic advisor Professor Steven Koester who

guided me in this process and the committee who kept me on track.

TABLE OF CONTENTS

LIST OF TABLES

LIST OF FIGURES

CHAPTER 1   INTRODUCTION

Since the first exfoliation of graphene (GR) from graphite using a mechanical cleavage method in 2004 by Novoselov and Geim [1], the study of two-dimensional (2D) atomically thin layered materials has opened a new era. New materials, device topologies and processor architectures have been researched to extend Moore's law, which originated in 1965 when Gordon Moore predicted that the number of transistors on a microchip would double every two years [2]. The chip industry had kept up with the law for many decades with continuously shrinking dimensions of conventional field-effect transistors (FETs). However, in the past decade, the technology scaling trend has started to slow down (Figure 1.1) due to the ever-worsening short-channel effects (SCEs) that cause high OFF-state leakage currents (I_{OFF}) leading to higher static power consumption.
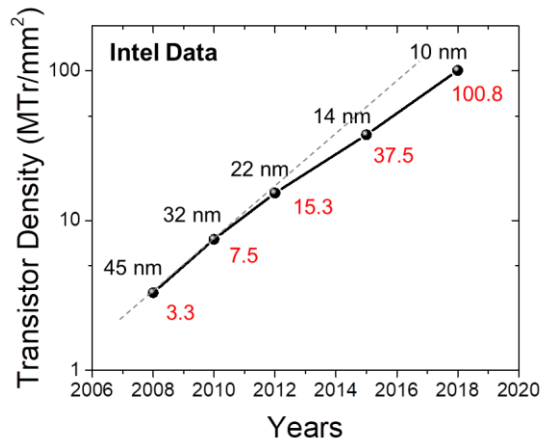
Figure 1.1: Transistor density in the unit of millions transistors per square millimeter as a function of the high-volume manufacturing start year for each technology node [3]. The transistor density is calculated based on the transistor density of a 2-input NAND cell (NAND2) and a scan flip-flop (SFF) and includes weighting factors that account for typical designs: Transistor density = 0.6 x (NAND2 Transistor Count / NAND2 Cell Area) + 0.4 x (SFF Transistor Count / SFF Cell Area). The grey dash line is fitted to the first three data points. The slowing of Moore's law is observed at 14 nm and 10 nm nodes due to the challenges rose from the ever-worsening short-channel effects.

13

With continued scaling of the device channel length at more advanced technology nodes, the device gate loses more controllability over the charge carriers in the channel leading to more degradation of the subthreshold slope and the OFF-state leakage behavior. New device architectures, such as FinFETs, have been designed to enhance gate controllability; however, even FinFETs are nearing their scaling limit. Hence, there is a strong demand for new channel materials that allow improved gate controllability at ultra-small dimensions. While graphene has remarkable properties (high carrier mobilities and thermal conductivity, etc.) and its atomically thin thickness (0.335 nm [4]) can allow for excellent gate controllability, the absence of an electronic band gap prevents it from being utilized in future logic electronics. A moderate electronic band gap is necessary for any material to be used as a transistor channel to ensure sufficient I_{ON}/I_{OFF} current ratios and acceptable OFF-state leakage current. Although efforts have been made to open up an electronic band gap in graphene, the reported band gaps are no more than 0.3 eV in most cases [5-10], insufficient for most transistor applications. This shortcoming of graphene led to the search for alternative 2D materials, such as black phosphorus (BP), transition metal dichalcogenides (TMDCs), and hexagonal boron nitride (hBN) covering a wide range of electronic properties. During my PhD study, I worked on a variety of 2D material based applications, including graphene quantum capacitance based vapor sensors [11-14], molybdenum disulfide (MoS_2) based dynamic random access memory (DRAM) cells, radiation effect in BP FETs [15, 16], and molybdenum ditelluride ($MoTe_2$) phase-engineered FETs [17] (Figure 1.2).
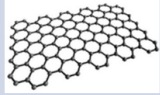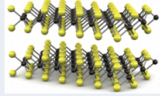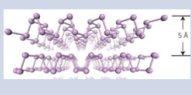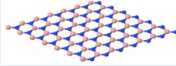
Material	Structure	Band Gap (eV)	Effective Masses	Mobility (cm²/Vs)	Applications
Graphene		0	"massless"	>10,000	RF FETs, Sensors, Photodetectors
TMDC (MX_2) M: W, Mo… X: S, Se, Te		0.5 – 2.5 depending on # layer	$m_e = 0.57m_0$ $m_h = 0.66m_0$ (MoS_2)	10 - 500	Low-power FETs, memories, sensors
Black Phosphorus (BP)		0.3 – 1.5 depending on # layer	$m_e = 0.15m_0$ $m_h = 0.14m_0$ (Armchair)	100 - 1000	Tunneling FETs, Photodetectors
h-Boron Nitride (BN)		~7.2 (indirect)	$m_e = 0.26m_0$ $m_h = 0.47m_0$	--	Gate dielectric, Encapsulation

Figure 1.2: The atomic structures, electrical properties, and applications of the 2D materials that I worked on during my PhD study.

1.1 Transition Metal Dichalcogenides

Among these 2D materials, the family of TMDCs has gained the most attention. TMDCs are crystals of the formula MX_2, where M is a transition metal atom (such as Mo, W, or Re) and X is a chalcogen atom (such as S, Se, or Te). About 40 different layered TMDCs exist. Figure 1.3a highlights the transition metals and the three chalcogen elements that predominantly crystallize in layered structure [18]. Figure 1.3b is a three-dimensional (3D) structure of the most widely studied TMDC, MoS_2, in a three-layer form [19]. TMDCs possess strong intra-layer chalcogen-metal covalent bonds where a layer of metal atoms are sandwiched between two chalcogen atomic layers. In the vertical direction, layers are connected through a week van der Waals force allowing them to be exfoliated into single- or few-layer forms from their bulk crystals [20]. TMDCs have a very long history. Their structure was first determined by Linus Pauling in 1923 [21], and the first production of ultrathin MoS_2 was achieved by Robert Frindt with the use of

adhesive tapes in 1963 [22]. It was not until recent years that the study of 2D TMDCs gained remarkable growth owing to the development in TMDC synthesis.
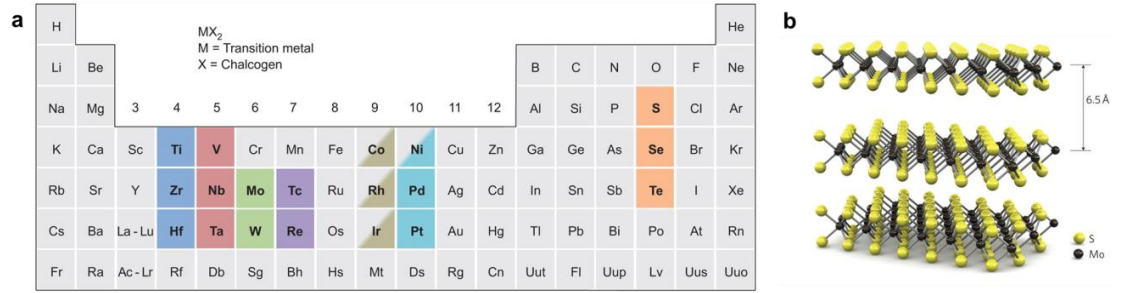
Figure 1.3: Chemical composition and 3D crystal structure of TMDCs. (a) The periodic table showing the transition metals and the three chalcogen elements that predominantly crystallize in layered structure. Reprinted with permission from reference [18]. (b) Three-dimensional representation of the structure of three-layer MoS_2. Single layer is 6.5 Å thick. Reprinted with permission from reference [19].

2D TMDCs span the full range of electronic properties including superconducting, metallic/semi-metallic, semiconducting, and insulating, thanks to its diverse chemical compositions and structural phases. 2D semiconducting (SC) TMDCs are of particular interest as they exhibit several superior properties compared to conventional 3D semiconductors (Si, Ge, and III-Vs). First, 2D SC TMDCs have a wide range of electronic band gaps and diverse band alignments [23, 24]. The predicted band gaps range from ~0.5 eV to ~2.5 eV [24]. The band gap increases monotonically as the number of layers decreases along with an indirect-to-direct band gap transition. For example, MoS_2 has an indirect bandgap of ~1.3 eV in bulk form but a direct bandgap of ~1.8 eV in single-layer form [25, 26]. Second, 2D SC TMDCs have ultra-thin body thicknesses enabling enhanced gate control and carrier confinement [27]. 2D SC TMDCs can be thinned down to a single layer with a typical thickness of 0.6-0.7 nm (such as MoS_2 in Figure 1.3b), while silicon can only be scaled down to 4-5 nm. Their ultra-thin body thickness allows significant reduction in the scaling length, λ, thus smaller channel

lengths. A minimum channel length of 3λ is required to minimize SCEs, such as drain induced barrier lowering (DIBL) (Figure 1.4). Third, 2D SC TMDCs have reduced degradation in their intrinsic electrical properties at ultra-thin body thickness, such as carrier mobility. Due to thickness variation, surface roughness and strain induced by lattice mismatch, their carrier mobilities in 3D semiconductors degrade substantially with decreasing body thickness in the sub-10 nm regime, while the degradation of mobilities in semiconducting 2D TMDCs is much less owing to reduced roughness and lack of dangling bonds (Figure 1.5) [28, 29]. These properties make 2D SC TMDCs promising alternatives to conventional 3D semiconductors for future scaled low-power and high-performance electronic applications.
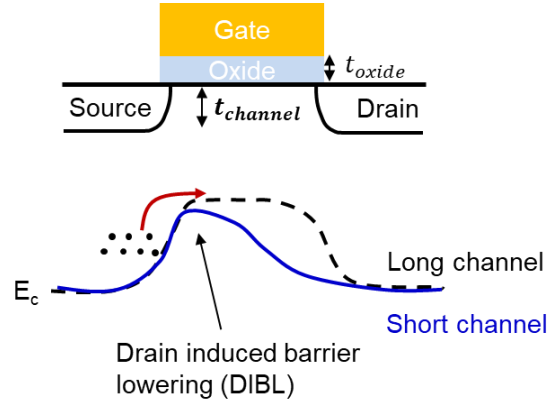
Figure 1.4: Schematic cross-section of a typical FET (top) and the corresponding conduction band of the channel underneath the gate dielectric (bottom). As channel length is reduced, the drain depletion region moves closer to the source deletion region, resulting in a lowering of the potential barrier at the source leading to increased injection of electrons, known as the drain induced barrier lowering (DIBL) effect. In order to mitigate the DIBL effect as well as other short-channel effects, a minimum channel length of 3 λ is required, where λ is the scaling length which can be estimated as $\sqrt{\varepsilon_{channel}/\varepsilon_{oxide} \cdot t_{channel} \cdot t_{oxide}}$. ε and t are the permittivity and thickness, respectively.
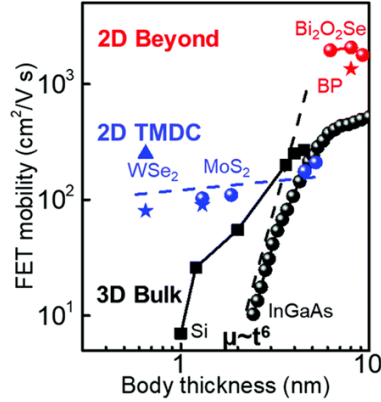
Figure 1.5: The field-effect mobilities of various 2D and 3D semiconductors as a function of channel thickness. In the sub-10 nm regime, the mobilities of 3D bulk semiconductors (black) decrease with thickness to the sixth power (mobility $\mu \sim t_b^6$), while the mobilities of 2D TMDCs (blue) vary little and demonstrate much higher values. Reprinted with permission from reference [29].

Despite these advances, replacement of conventional 3D semiconductors with 2D TMDCs faces several challenges including: (1) synthesis of large-scale high-quality films; (2) reduction of contact resistance at the metal/TMDC interfaces; (3) integration of high-quality high-κ top dielectrics; and (4) enhancement of charge carrier mobilities. This thesis aims to solve those issues for making high-performance 2D TMDC-based FETs.

1.1.1 Crystal Structure of TMDCs

2D TMDCs are layered materials in which each unit (MX_2) consists of a transition metal (M) layer sandwiched between two layers of chalcogen (X) atoms. They exist in several structural phases resulting from different coordination spheres of the transition metal atoms [30]. The three common phases are categorized as trigonal prismatic (hexagonal, 1H), octahedral (tetragonal, 1T) and the distorted octahedral phase (1T′, a.k.a. monoclinic phase), as illustrated in Figure 1.6 [31]. From the side views, monolayers of these structural phases can be viewed as different stacking orders of

18

chalcogen-metal-chalcogen atomic planes. The 1H phase has an ABA stacking, in which chalcogen atoms on the top and bottom planes are overlapping along z-direction. By contrast, the 1T phase has an ABC stacking, in which chalcogen atoms on the top plane are rotated by 180 degrees from the chalcogen atoms on the bottom plane. The high-symmetry 1T structure is unstable, at least in the absence of external stabilizing influences, and undergoes a spontaneous lattice distortion to form 1T′ phase [31, 32]. In the stable lower-symmetry 1T′ phase, transition metal atoms are shifted in the x-direction resulting in the modification of atomic displacement of the chalcogen atoms along the z-direction [33, 34]. Interestingly, monolayer 2H phase lacks inversion symmetry while monolayer 1T′ phase preserves it, allowing the discrimination of two phases using optical techniques, such as the second harmonic generation (SHG) and Raman spectroscopy. However, the inversion symmetry in 1T′ phase is broken for an even number of layers [35].
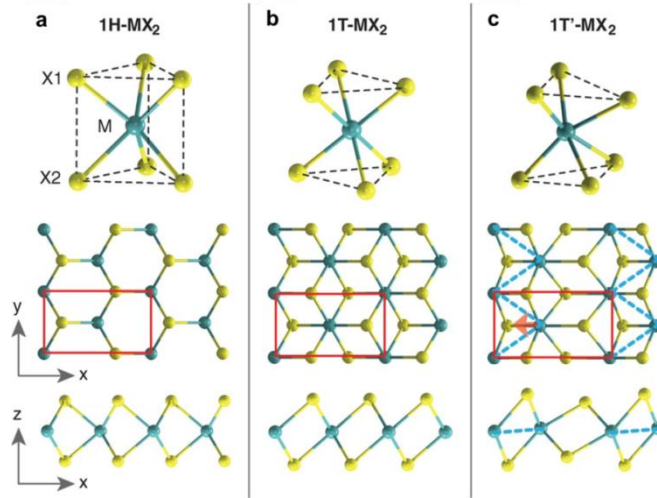
Figure 1.6: Atomic structures of monolayer 1H, 1T, and 1T′ MX_2. M and X represent a transition metal atom and a chalcogen atom, respectively. (a) 1H-MX_2 in ABA stacking with $p\bar{6}m2$ space group. (b) 1T-MX_2 in ABC stacking with $p\bar{3}m2$ space group. (c) 1T′-MX_2, where the distorted M atoms form 1D zigzag chains (dashed blue line). The unit cell is indicated by red rectangles. Reprinted with permission from reference [31].

Group-VI TMDCs in which the transition metal M is Mo or W (including MoS_2, $MoSe_2$, $MoTe_2$, WS_2, WSe_2, and WTe_2) have received the greatest amount of attention. Their thermodynamically stable phase is either the 2H (the prefix '2' refers to a bulk stacking mode) or 1T′ phase depending on the chemical composition. K.-A. N. Duerloo *et al.* calculated the equilibrium (stress-free) relative energies of the 2H, 1T, and 1T′ phases for all six possible group-VI TMDCs in monolayer form using density functional theory (DFT) [32]. The results (Figure 1.7) show that under ambient conditions five out of six group-VI TMDCs are thermodynamically stable in the 2H phase, except WTe_2 which is stable in the 1T′ phase, consistent with experimental observation [36]. The smallest energy difference between 2H and 1T′ phases among all group-VI TMDCs is observed in $MoTe_2$, approximately only 35 meV per unit cell [33]. This small energy difference allows the selective synthesis of high-purity 2H and 1T′ $MoTe_2$ and *in-situ* synthesis of their lateral homojunctions using a flux-controlled phase-engineering method [37]. More on the flux-controlled method is discussed in Chapter 2. It also allows the phase transition between 2H and 1T′ phase (discussed in Chapter 1.5 and Chapter 5).
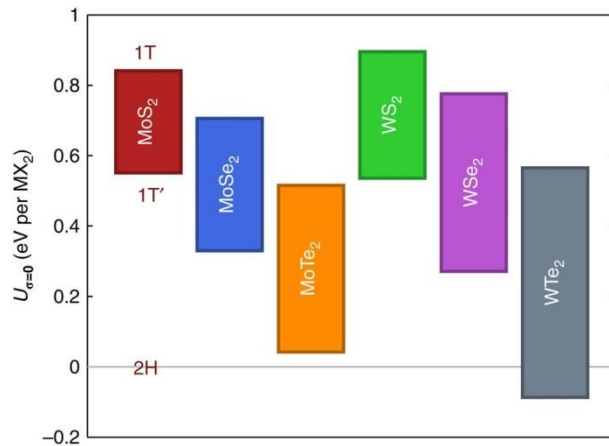
Figure 1.7: Ground-state energy differences between monolayer 2H, 1T, and 1T′ phases of group-VI TMDCs. The energy U is given per formula unit MX_2 and is computed at the equilibrium lattice parameters. Reprinted with permission from reference [32].

1.1.2 Electronic Band Structure of TMDCs

Here, I discuss the basic features of the band structures of 2H- and 1T′- $MoTe_2$ as a representative of other group-VI TMDCs. The band structure calculations were performed using DFT by Javad G. Azadani and Prof. Tony Low at the University of Minnesota. Computational details are provided in Appendix B.1. Figure 1.8 shows the evolution of the band structure of 2H-$MoTe_2$ calculated using Perdew−Burke−Ernzerhof (PBE) / generalized gradient approximation (GGA) with spin-orbit coupling (SOC) upon decreasing its thickness from five-layer to monolayer. 2H-$MoTe_2$ is semiconducting with a thickness-dependent band gap. The positions of the valence and conduction band edges change with decreasing thickness and the indirect band gap turns into a direct band gap in single-layer form. The band gap calculated by taking the difference between the conduction band minimum (CBM) and the valence band maximum (VBM) increases inversely with the thickness (0.73 eV, 0.82 eV, 0.91 eV, and 1.0 eV for quadrilayer, trilayer, bilayer, and monolayer, respectively). Overall, the calculated band gaps are smaller than the experimentally extracted values because it is well known that DFT simulation underestimates the band gap [38]. The SOC induced breaking of the band degeneracy is also observed in multi-layer forms. Moreover, the CBM and the VBM of the monolayer band structure are located at the two inequivalent high-symmetry points K and K´, which correspond to the corners of the hexagonal Brillouin zone, enabling potential valleytronics applications [39-41].

Figure 1.9 shows the evolution of the band structure of 1T′-$MoTe_2$. The band gap is closed and the CBM and VBM are overlapped. The states of the conduction band and the valence band are not separated completely; therefore 1T′-$MoTe_2$ is semi-metallic. The

SOC induced breaking of the band degeneracy points between the valence and conduction bands is found to be insufficient to open a band gap [42].
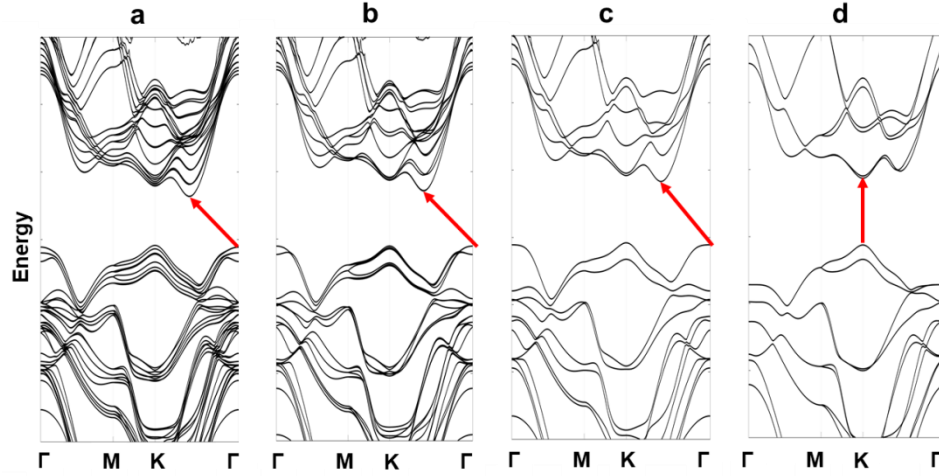
Figure 1.8: Calculated band structures of (a) quadrilayer, (b) trilayer, (c) bilayer, and (d) monolayer 2H-MoTe$_2$. The solid arrows indicate the lowest energy transitions. Multi-layer 2H MoTe$_2$ is characterized by an indirect band gap, while monolayer 2H-MoTe$_2$ is a direct band gap semiconductor. The band gap for quadrilayer, trilayer, bilayer, and monolayer is 0.73 eV, 0.82 eV, 0.91 eV, and 1.0 eV, respectively. The calculations were performed by Javad G. Azadani and Prof. Tony Low at the University of Minnesota.
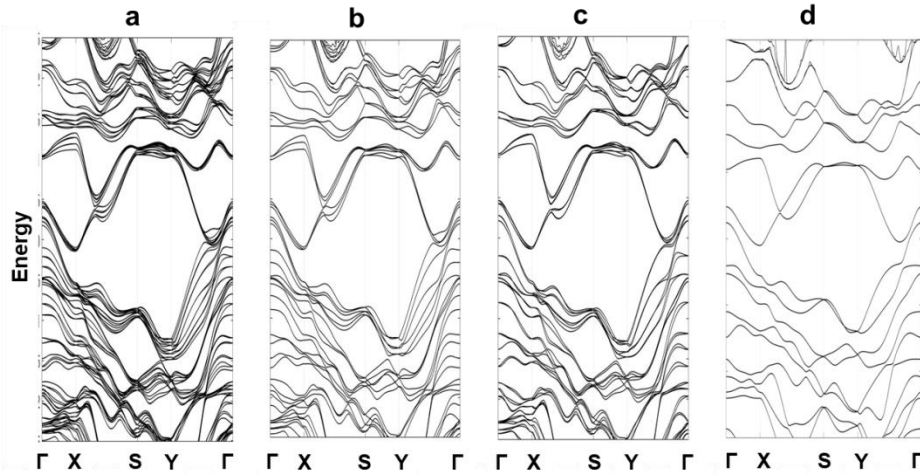
Figure 1.9: Calculated band structures of (a) quadrilayer, (b) trilayer, (c) bilayer, and (d) monolayer 1T′-MoTe$_2$. Multi-layer and monolayer 1T′-MoTe$_2$ are semi-conducting. SOC induces breaking of the band degeneracy points between the valence and conduction bands, but it is insufficient to open a band gap. The calculations were performed by Javad G. Azadani and Prof. Tony Low at the University of Minnesota.

1.2 Synthesis and Transfer of TMDCs

One of the major challenges that limit the application of 2D TMDCs for future high-performance electronics is the synthesis of wafer-scale high-quality films. In general, single- or few-layer TMDCs can be synthesized through two complementary strategies: the top-down and bottom-up approaches. The top-down approaches involve applying a peeling force to cleave thin layers from bulk crystals via mechanical exfoliation [43, 44, 45, 46], liquid sonication [47], chemical intercalation [48, 49], etc. or thinning down thicker films via layer-by-layer etching [50-52]. The bottom-up approaches, conversely, involve assembly of TMDCs atom-by-atom or molecule-by-molecule via the direct reaction of M^{n+} and nX^{2-} ions that are formed from precursors containing metal M and chalcogen X elements, such as molecular beam epitaxy (MBE) [53, 54], chemical vapor deposition (CVD) [55-62], metal-organic CVD (MOCVD) [63, 64], atomic layer deposition (ALD) [65-68], etc.

This chapter reviews the most popular top-down and bottom-up approaches for synthesizing 2D TMDCs, namely mechanical exfoliation and CVD. Methods for transferring the exfoliated flakes or as-grown films onto target substrates for device fabrications are also discussed.

1.2.1 Mechanical Exfoliation

In most fundamental studies, 2D TMDCs are obtained from mechanical exfoliation because exfoliation only requires a bulk crystal and commercial adhesive tape (e.g. 3M Scotch brand tape or "blue" tape) and produces high-purity flakes. The adhesion between the tape and the basal plane of the crystal is stronger than the weak interlayer

van der Waals forces, allowing for the cleavage of very thin flakes. Exfoliation can be

performed when the crystal or thick flake is sandwiched by a folded tape, which is then

peeled apart to obtain thinner flakes (Figure 1.10). Repeating this process on the freshly

peeled flakes can lead to single- or few-layer nanosheets that can then be transferred onto

a target substrate (quartz, SiO_2/Si, etc) for device fabrication using a

polydimethylsiloxane (PDMS) dry transfer method (Figure 1.11) [69]. Vertical TMDC

heterostructures can be created by transferring one TMDC over another using the same

transfer method [70, 71].
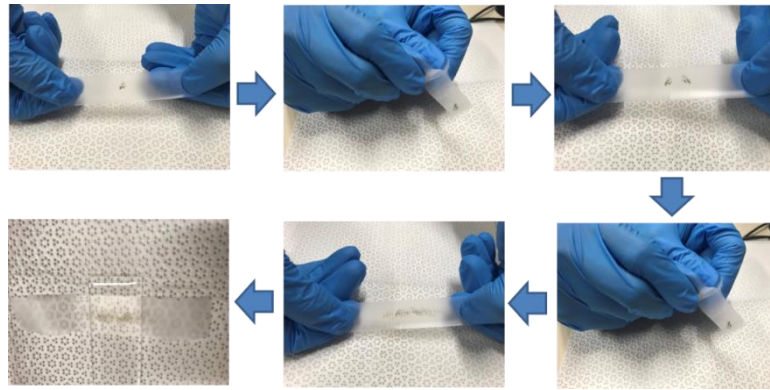
Figure 1.10: An illustrative procedure of the Scotch-tape based mechanical exfoliation. At the end, exfoliated flakes on the tap are transferred on a PDMS stamp on a glass slide.
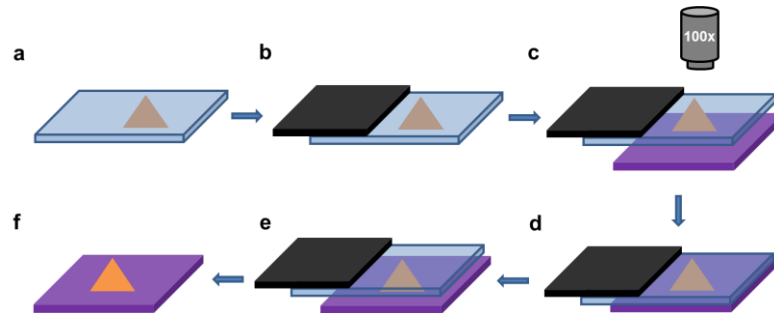
Figure 1.11: The procedure of the PDMS dry transfer method. (a) The flake is transferred onto a PDMS stamp on a glass slide. (b) The slide is then attached to a micromanipulator (black). (c) The flake is aligned with the final substrate using a microscope. (d) The PDMS stamp and the substrate are brought in contact. (e) The PDMS stamp is slowly peeled off. (f) The flake is transferred onto the substrate due to a stronger adhesion force with the substrate.

Although this method produces high-quality flakes, the flake sizes are usually 10's of microns or less and the flake surfaces are not uniform, typically containing numerous regions with different thickness. Substantial residues from tape and PDMS are also found to occur on TMDC surfaces [72, 73]. These issues make the mechanical exfoliation impractical as a scalable method for mass production. In an effort to improve the scalability of mechanical exfoliation, many strategies have been developed [74, 75, 76]. Notably, M. Velický *et al.* reported a facile gold-assisted mechanical exfoliation of extraordinarily large monolayer MoS_2, up to a centimeter size, limited only by bulk crystal sizes [75], but the etchant used to remove Au might induce defects in TMDCs.

1.2.2 Chemical Vapor Deposition

Chemical vapor deposition (CVD) is one of the most practical methods to obtain large-area single-phase TMDCs, as well as create vertical and lateral heterostructures. The CVD method can be classified into two categories: (1) the single vapor method (a.k.a. metal-sulfurization method) involving the thermal reaction of transition metal (M) thin films deposited on the substrates in a chalcogen (X) vapor environment, and (2) the double vapor method involving the co-evaporation of transition metal oxide (MO_3) and element chalcogen followed by the formation of TMDC films over the substrates by vapor phase reaction. Both methods are carried out under thermal treatment (300-700 ^{o}C) inside a furnace with inert gases. The process of forming TMDCs depends on the properties of the substrates (such as lattice parameter and surface energy), temperature, and atomic gas flux [34, 77, 78].

In the single vapor method, transition metals are deposited on the substrates and subsequently converted into TMDC layers by thermal reaction with chalcogen vapor (Figure 1.12a [34, 61]).

$$M(s) + 2X(g) \rightarrow MX_2(s) \tag{1.1}$$

The TMDC films grown by this method are usually large-scale continuous films that can cover the entire area where the metals are deposited, but they are often found to be polycrystalline with small grains and defects [60, 61, 62]. It is also difficult to systematically control wafer-scale thickness and uniformity.

In the double vapor method, transition metal oxide MO_3 is initially reduced into a sub oxide MO_{3-x}, which then reacts with vaporized chalcogen X to form a 2D layered MX_2 film (Figure 1.12b [55]).

$$MO_3(s) + X(g) \rightarrow MO_{3-x}(s) + XO_x(g) \tag{1.2}$$

$$MO_{3-x}(s) + X(g) \rightarrow MX_2(s) \tag{1.3}$$

Metal oxides are chosen as they are cheap and have relatively low melting and evaporation temperatures [56]. This method generally forms randomly distributed MX_2 domains (such as triangular flakes), rather than large-scale continuous films [55-59].

CVD-grown 2D TMDC films can be transferred onto target substrates using the PDMS dry transfer method (Figure 1.11), and wet transfer methods with the assistance of polymers such as polymethyl methacrylate (PMMA) (Figure 1.13) [79-81] or polystyrene (PS) [82].
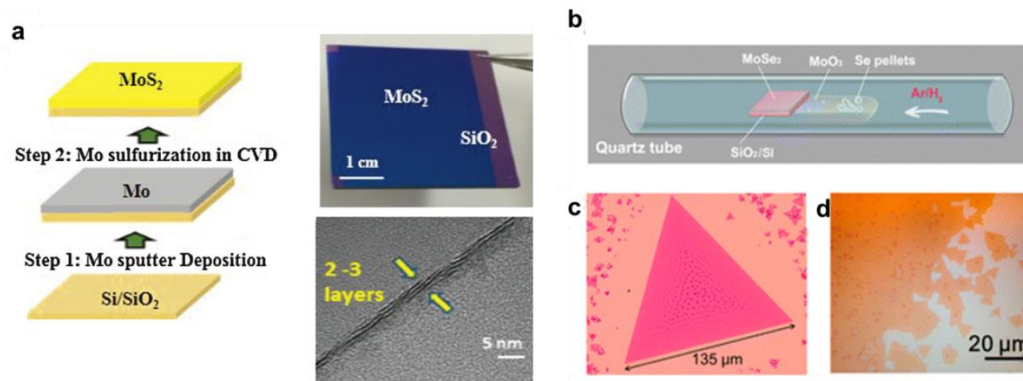
Figure 1.12: Two CVD methods: (a) the single vapor method and (b) the double vapor method. (a) Large area growth of 2–3 layers of MoS_2 using Mo seed layer sulfurized in a CVD furnace. Reprinted with permission from reference [34]. (b) Schematic of the synthesis of monolayer $MoSe_2$ using the co-evaporation MoO_3 and Se. Se pellets and MoO_3 powder are positioned in the same ceramic boat at the center of the tube furnace. (c, d) Typical optical images of monolayer triangles and emerged continuous films. Reprinted with permission from reference [55]. Copyright (2014) American Chemical Society.
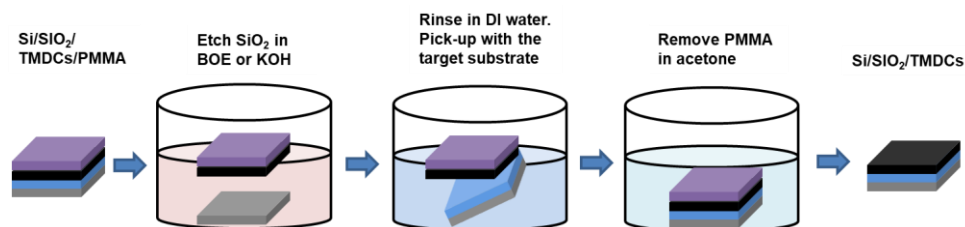
Figure 1.13: Schematic of the wet transfer method with PMMA. The SiO_2/Si substrate with TMDC flakes is coated with a thin layer of PMMA then submerged in BOE or KOH to remove the SiO_2. Once fully detached from the substrate, the film is transferred into DI water then picked up with the target substrate. The target substrate with the transferred film is baked or blown dry and then soaked in Acetone to remove PMMA.

1.3 Properties and Applications of TMDCs

The diverse chemical compositions and structural phases of 2D TMDCs result in a wide range of properties, making them promising materials for various applications such as nanoelectronics, nanophotonics, optoelectronics, flexible electronics, energy storage devices, various sensors, catalysis, spin- and valleytronics. This chapter extends the

discussion of the properties of 2D SC TMDCs in Chapter 1.1 and highlights several practical applications.

First, as discussed in Chapter 1.1, most 2D SC TMDCs have a sizable band gap larger than that of silicon (1.1 eV). The theoretically predicted mobility is also very high, up to 1,000 cm^2 V^{-1} s^{-1} at room temperature [83, 84, 85]. However, the experimental mobility is limited by disorder, the presence of scattering sources, and large contact resistance. With mobility engineering and process optimization such as the choice of appropriate substrates and metal contacts, mobility of a few hundred cm^2 V^{-1} s^{-1} has been achieved [19, 86]. For example, B. Radisavljevic *et al.* demonstrated a room-temperature mobility of 200 cm^2 V^{-1} s^{-1} in single-layer exfoliated MoS$_2$ with HfO$_2$ top-gate dielectric [19]. S. Das *et al.* reported a room-temperature mobility of 700 cm^2 V^{-1} s^{-1} in 10-nm-thick exfoliated MoS$_2$ flake with scandium contacts and Al$_2$O$_3$ encapsulation [86]. The large band gap ensures low OFF-state leakage current and large mobility ensures high ON-state drive current. Hence, TMDC-based FETs exhibit high current I_{ON}/I_{OFF} ratio (Figure 1.14). I have fabricated FETs based on 10-nm-thick exfoliated MoS$_2$ flakes on 300 nm SiO$_2$/Si substrates. Even gated through the 300 nm SiO$_2$ dielectric, the devices exhibit room-temperature current I_{ON}/I_{OFF} ratios up to 10^8 and high drive currents in the µA/µm range (Figure 1.15).

Second, 2D SC TMDCs have larger effective masses in comparison with silicon. For example, MoS$_2$ has effective mass m^* ~$0.5m_0$ for both electrons and holes [87], where m_0 is the free electron mass, while silicon has tunneling-relevant m^* ~$0.2m_0$ [88]. For this reason, combined with its large band gap and ultra-thin body thickness, short-channel effects (such as gate-induced drain leakage, GIDL, and drain-induced barrier

28

lowering, DIBL) are expected to be substantially suppressed in MoS$_2$, making it suitable for extremely low-power applications. I have demonstrated MoS$_2$ based dynamic memory random access (DRAM) cells in two-transistor (2T) grain-cell configuration (Figure 1.6a). The current leakage from the access transistor is largely reduced by using MoS$_2$ as the channel material. Under certain bias conditions, the device can achieve a retention time up to ~ 1 s, far more than the required retention time for DRAM cells (64 ms [89]), corresponding to a leakage current as low as a few fA/μm, far below the noise floor of conventional DC measurements (Figure 1.6b).
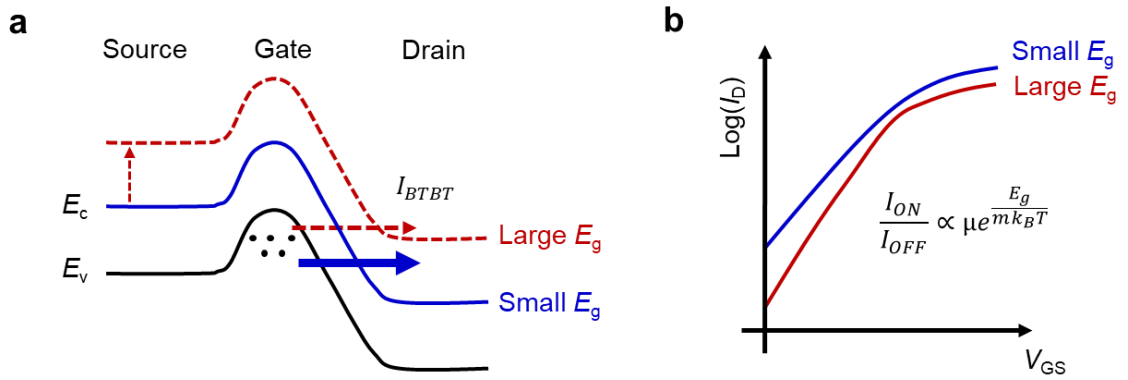
Figure 1.14: (a) Energy band diagram along the channel of a FET in the OFF state and (b) drain current (I_D) in log scale as a function of gate-to-source voltage (V_{GS}) for small and large energy band gaps (E_g). The OFF-state current (I_{OFF}), such as band-to-band tunneling (BTBT) current (I_{BTBT}), is proportional to exp(-E_g/mk_BT) where m is a factor of 2 or larger depending on the transistor design, k_B is the Boltzmann constant, and T is the temperature. Larger E_g suppresses I_{OFF}. The ON-state current (I_{ON}) is proportional to carrier mobility μ. Thus, current I_{ON}/I_{OFF} ratio follows μ exp(E_g/mk_BT). Hence, larger E_g and μ lead to higher current I_{ON}/I_{OFF} ratio.
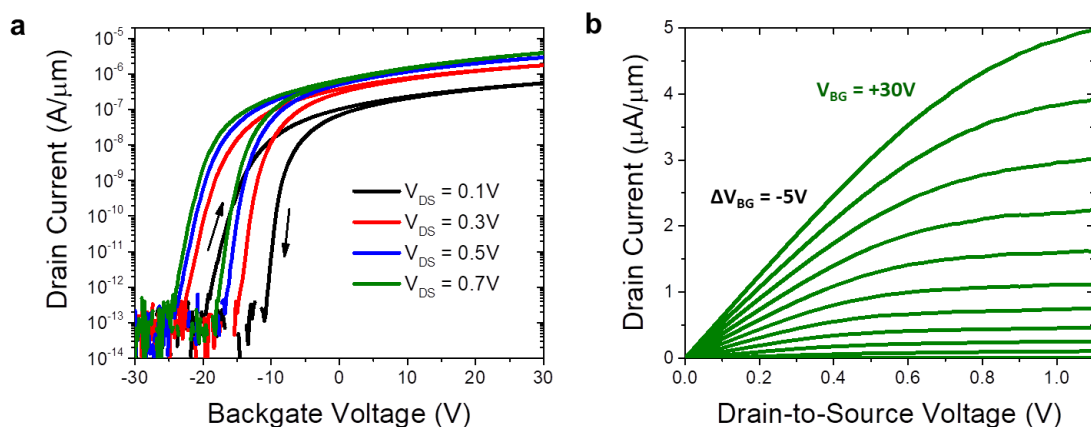
Figure 1.15: (a) Transfer and (b) output characteristics of a MoS$_2$ FET under substrate gating (300 nm SiO$_2$) under different bias conditions. The device has a gate length of 2 um and width of 3.5 um. The thickness of the exfoliated MoS$_2$ flake is ~ 10 nm. V_{DS} is the drain-to-source voltage and V_{BG} is the voltage applied at the back substrate.
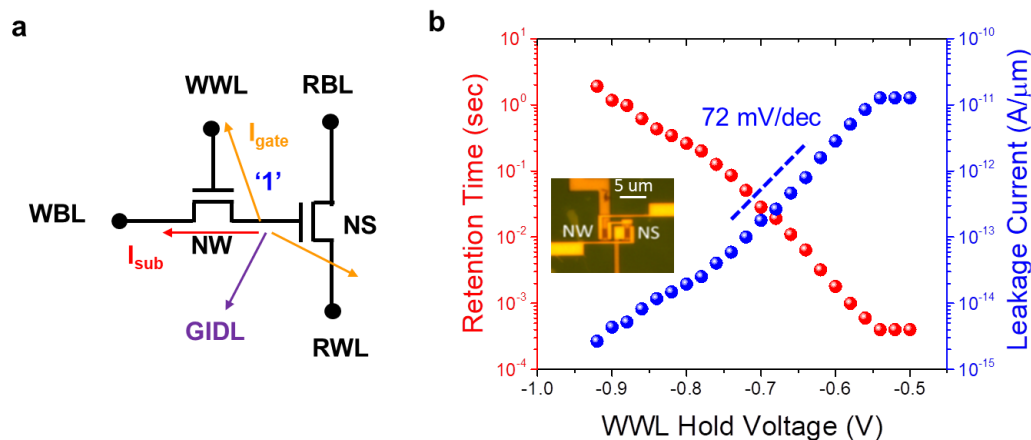
Figure 1.16: (a) Schematic of a DRAM cell in the two-transistor (2T) grain-cell configuration. WBL, WWL, RBL, and RWL stand for write bitline, write wordline, read bitline, and read wordline, respectively. NW and NS are the n-type write and read access transistor, respectively. The arrows represent various leakage currents when the storage node is at logic '1'. (b) Retention time and corresponding leakage current of a MoS$_2$ based 2T DRAM cell in the hold mode as a function of WWL voltage. The inset is an optical image of the device. The scale bar is 5 μm.

Third, 2D SC TMDCs are promising electrode materials for energy storage, such as Li-ion batteries and supercapacitors, because (1) their large interlayer spacing (0.6-0.7 nm) allows for Li$^+$/Na$^+$ intercalation, (2) high surface to volume ratio provides large

capacity for storing Li^+/Na^+, and (3) excellent conductivity facilitates the transport of electrons [90, 91]. K. Chang *et al.* developed nanostructured MoS_2-graphene composites that exhibit extraordinary capacity, up to 1300 mA hg^{-1}, and excellent rate capability and cycling stability as an anode material for Li-ion batteries [92].

Moreover, 2D SC TMDCs outperform traditional semiconductors (such as organic materials) for flexible electronics as they can afford both high electronic performance and high mechanical flexibility, and have the ability to be transferred onto arbitrarily large substrates. The Young's modulus of MoS_2 is extremely high (E = 0.33 TPa), comparable to that of graphene oxide [93]. H.-Y. Chang *et al.* demonstrated flexible CVD-grown MoS_2 thin film transistors (TFTs) with intrinsic transit frequencies of 5.6 GHz and maximum oscillation frequencies of 3.3 GHz [94]. The devices were mechanically robust for 10,000 bending cycles.

1.4   Contact Engineering in TMDCs Based FETs

Although TMDCs based FETs have shown better subthreshold behaviors and less OFF-state leakage compared to that of silicon and III-V semiconductors based FETs, the large contact resistance at the metal/TMDC interface limits their drive current for high-performance applications. The contact resistance becomes more dominant while the channel resistance quickly decreases as the device dimension shrinks at more advanced technology nodes. The typical experimental contact resistance of TMDCs based FETs are on the order of kΩ·μm to MΩ·μm [95]. However, the theoretical quantum limit of the contact resistance, R_c, is determined by the number of conducting modes within the semiconducting channel, which is related to the 2D charge carrier density, n_{2D}, as

$R_cW \sim h/2e^2k_F \sim 0.026/\sqrt{n_{2D}}$ kΩ·μm [96, 97], where W is the width of the channel, h is

Planck's constant, e is the electron charge, k_F is the Fermi wavevector, and n_{2D} is in the

units of 10^{13} m^{-2}. Figure 1.17 depicts this quantum limit for various conventional

crystalline semiconductors [98]. For TMDCs with a sheet electron density of 10^{13} m^{-2},

the predicted minimum contact resistance is 0.026 kΩ·μm, which is well below the

projected maximum allowable contact resistances for high-performance multiple-gate

FET technology (0.08 kΩ·μm) as per the ITRS requirements for the year 2026 [99].

Hence, there is a need to improve the metal/TMDC contact resistance, making it highly

desirable to understand the nature of the electronic contact between metals and TMDCs

and find effective solutions to lower the contact resistance. This chapter discusses the

major challenges to achieving low contact resistance in TMDCs based FETs.
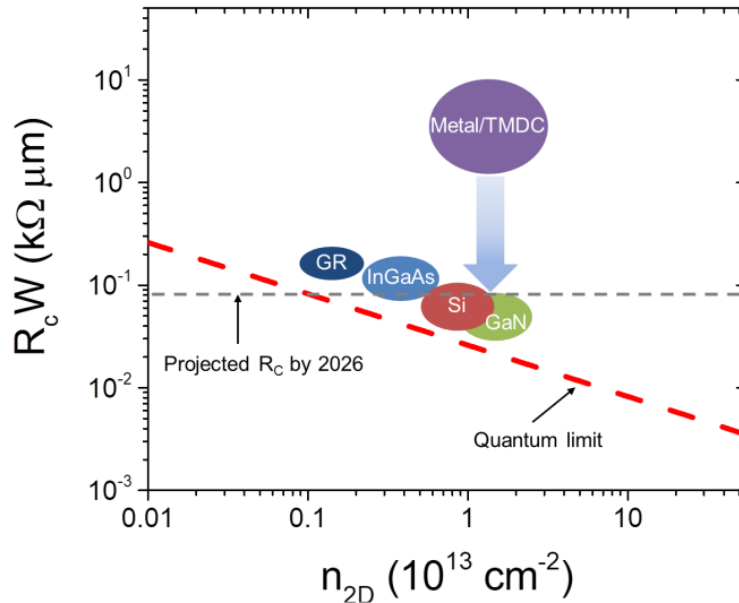
Figure 1.17: Contact resistances against the quantum limits for various semiconductor materials: graphene (GR), InGaAs, Si, GaN and TMDC with metal contacts. Reproduced with permission from reference [98].

1.4.1 Contact Topology

There are two fundamental contact topologies between bulk metals and 2D TMDCs: top contact (Figure 1.18a) and edge contact (Figure 1.18b). It has been shown that edge contacts can lead to much better charge injections than top contacts thanks to the stronger hybridization (orbital overlapping) and the reduction of tunnel barriers at the edge surface [100-104]. However, because close proximity is required, it is difficult to realize pure metal edge contacts (e.g. without interfacial voids), especially to thicker TMDCs using conventional lithographic techniques. In most situations, metal contacts to TMDCs are in the top-contacted topology or a combination of the top-contacted and edge-contacted topologies (Figure 1.18c). In the combined configuration, contribution from the top surface to the resistance is greater than that from the edge surface due to the large surface-area-to-edge-area ratio. Therefore, it is more important to optimize the contact resistance from the top surface.

Figure 1.18: Contact topologies between bulk metals and 2D TMDCs. (a) top contact, (b) edge contact, and (c) combined contact.

The high contact resistance from the top surface is mainly due to two factors: (i) large Schottky barrier height (SBH) resulting from strong Fermi-level pinning (FLP) [101, 105-108], and (ii) existence of a van der Waals (vdW) gap [101, 106, 109] at the metal/TMDC interfaces. The high contact resistance results in a long transfer length

causing a increase in contact resistance while scaling the contact length [110-112]. The following sections discuss each term in detail.

1.4.2   Schottky Barrier (SB)

In bulk metal/2D TMDC top contacts, work function difference between the contact metals and underneath 2D TMDCs results in a Schottky barrier (SB) that reduces the charge injection from metals into the device channel leading to non-Ohmic contacts, just like in bulk metal/3D conventional semiconductor contacts (Figure 1.19a) [113]. The SBH is enlarged due to TMDCs' wide bandgaps and strong FLP effects at the metal/TMDC interface (discussed in Chapter 1.4.3) leading to large contact resistance and performance degradation [105, 106].

Many methods have been used to extract the Schottky barrier height (SBH) in 2D TMDCs. The most popular approach is to extract the SBH from the activation energy in the thermionic regime. The SBH at the reverse-biased contact of a FET (e.g. source contact of an n-type FET) causes most of the voltage drop. The current injected through the reverse-biased SB, I_D, can be modeled using the thermionic emission equation [114-117], as shown below (where typical units are given for the relevant parameters):

$$I_D = A^{**}T^{\alpha}e^{[-\frac{1}{k_BT}(\Phi_{SB}-\frac{qV_{DS}}{\eta})]} \tag{1.4}$$

where A^{**} is the effective Richardson constant (A/K$^{\alpha}$) which can be derived for 3D and 2D semiconductors, T is the temperature (K), α is an exponent equal to 2 for 3D semiconductors and 1.5 for 2D semiconductors [118, 119], k_B is Boltzmann's constant (eV/K), Φ_{SB} is the effective Schottky barrier height for holes (eV), qV_{DS} is the product of the electronic charge and drain-to-source voltage (eV), and η is the ideality factor

accounting for barrier lowering due to image charges. The term $(\Phi_{SB} - qV_{DS}/\eta)$ is the activation energy, E_A. E_A at a fixed gate voltage (V_{GS}) is extracted from the slope of an Arrhenius plot, where $\ln(I_D/T^\alpha)$ is plotted $vs.$ $1/k_BT$, at different values of V_{DS} (Figure 1.19b). The activation energy at zero V_{DS}, which is the SBH, is linearly extrapolated from the plot of activation energies vs. V_{DS} (Figure 1.19c). The flat-band SBH under the flat-band condition ($V_{DS} = V_{FB}$) can be extracted from the plot of SBH vs. V_{GS} (Figure 1.19d). The SBH can also be extracted in the thermionic field emission regime [120, 121] or through ultraviolet and X-ray photoelectron spectroscopy [122-125], etc.
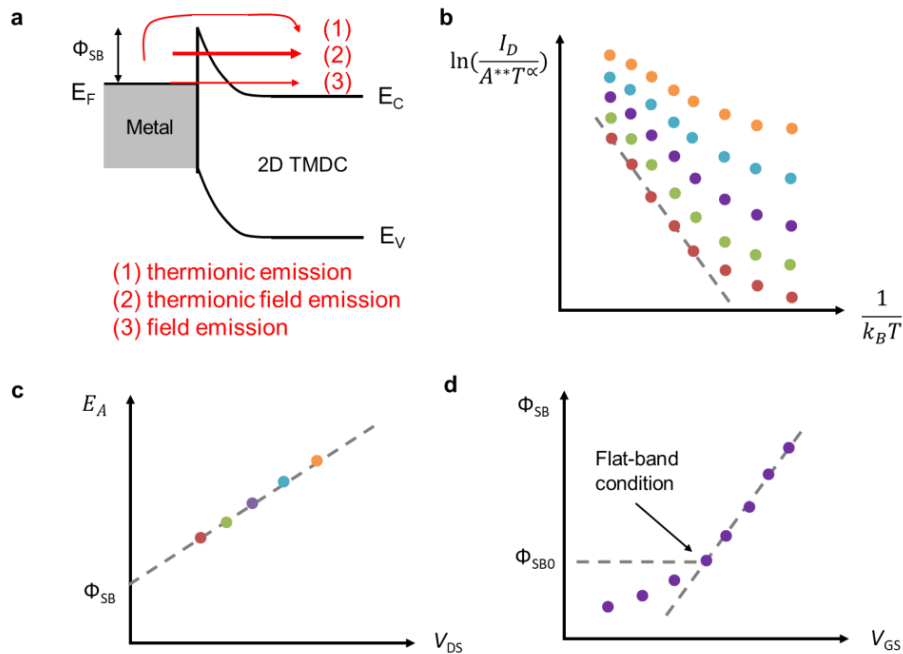
Figure 1.19: Schottky Barrier Band Diagram and Extraction. (a) Band diagram of a bulk metal/2D TMDC interface without van der Waals gap. The red arrows (from top to bottom) represent the different injection mechanisms: thermionic emission, thermionic field emission and field emission (tunneling). (b) The Arrhenius plot for different V_{DS} values at a given V_{GS}. The slope is $-E_A = -(\Phi_{SB} - qV_{DS}/\eta)$. (c) Activation energy E_A extracted from (b) vs. V_{DS}. The y-intercept is when $E_A = \Phi_{SB}$ for the given V_{GS}. (d) Φ_{SB} vs. V_{GS}. The flat-band Schottky barrier, Φ_{SB0}, can be extracted from the point where E_A stops depending linearly on V_{GS}.

35

The most intuitive approach to lower SBH is through work function engineering of the contact metals. Metals with Fermi level closer to the CBE of TMDCs can be chosen to reduce the SBH for electron injection whereas metals with Fermi level closer to the VBE of TMDCs can be used to lower the SBH for hole injection. This is known as the Schottky-Mott rule, which states that the SBH is the difference between the metal's work function and the semiconductor's electron affinity [109, 118, 126]. In reality, however, this approach would not work well due to the presence of interfacial energy states in the band gaps of TMDCs that pin the metal's work function (a.k.a FLP effects). A more effective strategy would be to degenerately dope source/drain contact regions causing a large band-bending in TMDCs leading to a significant reduction of the SBH and Schottky barrier width (SBW), thus a higher carrier tunneling probability. In conventional CMOS technology, substitutional doping (e.g. ion implantation) is commonly used to degenerately dope source/drain regions of MOSFETs to realize Ohmic n- and p-type contacts; however, this has been found to cause surface damage [127-131]. The thin nature of 2D TMDCs makes them more vulnerable to ion implantation as it is much easier to induce a significant amount of surface damage, interface traps and impurities, and etching of the TMDC layers. Promisingly, several substitutional n- and p-type doping of TMDCs have been achieved by incorporating dopant atoms to replace either cation and anion during the bottom-up synthetic growth process (e.g. CVD) or during chemical immersion [132-140]. Substitutional n-type/p-type doping have been demonstrated by replacing the Mo cations with rhenium (Re) /niobium (Nb) atoms [132-137] wherein the Re/Nb atoms act as electron donors/acceptors because Re/Nb has one more/less valence electron than the Mo atoms. H.-J. Chuang *et al.* obtained degenerately

p-doped MoS_2 by substitutional doping of MoS_2 using Nb during the chemical vapor transport process and then used the mechanical exfoliation method to transfer the degenerately p-doped MoS_2 and undoped MoS_2 to form a vertical heterostructure contacts that exhibit low contact resistance of ~ 0.3 kΩ·μm [136]. Substitutional n-type/p-type doping has also been achieved by replacing the S anions with chlorine (Cl)/nitrogen (N) atoms wherein the Cl/N atoms act as electron donors/acceptors because Cl/N has one more/less valence electron than the S atoms [138-140]. L. Yang *et al.* reported a chloride molecular doping technique wherein the Cl atoms occupy the sulfur vacancy sites in MoS_2 and WS_2, achieving contact resistance as low as 0.5 kΩ·μm [138].

Other strategies that have been employed to induce n-type or p-type doping include: (i) surface charge transfer doping via adsorption or encapsulation of "donor" or "acceptor" species, such as chemical reagents and sub-stoichiometric high-κ oxides (due to interfacial oxygen vacancies). N-type charge transfer doping has been achieved using benzyl viologen [141], TiO_x [142], MoO_x [143]. HfO_x [144], AlO_x [145], poly(vinyl-alcohol) [146], etc, while p-type charge transfer doping has been realized using $AuCl_3$ [147], wide band-gap n-type InGaZnO [148], etc; (ii) phase engineering via chemical doping [95]; and (iii) electrostatic doping via ionic electrolyte gating [149-152].

1.4.3 Fermi-Level Pinning (FLP)

The possible origin of FLP has been ascribed to many causes: (i) intrinsic defects (such as transition metal or chalcogen vacancies) and elemental impurities introduce mid-gap states that pin the metal's Fermi level [153-155]; (ii) a result of two simultaneous interface behaviors: first by a modification of the metal's work function by interface

dipole formation due to the charge redistribution at the interface, and second by the formation of mid-gap states originating from transition metal d orbitals, that result from the weakening of the intralayer transition metal-chalcogen bonding due to the interfacial contact metal-chalcogen interaction [101, 107, 156, 157], etc. We collaborated with R. Wu *et al.* to study the structure of the Ti/MoS$_2$ interface. Ti/Au contacts were first made to few-layer MoS$_2$ films using high-vacuum electron beam evaporation (EBE) and then cross-sectional annular dark-field (ADF)-scanning transmission electron microscopy (STEM) were used to elucidate the interface. The results are shown in Figure 1.20 [157]. The high-magnification ADF-STEM results (Figure 1.20c) showed that along the Ti-MoS$_2$ interface, there are areas where the Ti contacts the MoS$_2$ and alters the structure of the topmost layer and areas where small void pockets (similar to vdW gaps) are visible, leaving the topmost MoS$_2$ layer pristine. In the altered regions, Ti atoms tend to not only bond but also cluster on the MoS$_2$ surface. The presence of Ti atoms in deeper MoS$_2$ layers was also observed (Figure 1.20e). The formation of clusters and the penetration of Ti atoms into deeper MoS$_2$ layers degrade the crystal structure of MoS$_2$ leading to many localized mid-gap states.

DFT simulation suggested that mid-gap states can be reduced by using metals possessing a low affinity for the chalcogen atoms (such as Au or In) or their alloys (Figure 1.21 [157]), but the resulting interface is more likely to be a vdW type. Due to those localized mid-gap states, FLP leads to fixed SBHs, independent or weakly dependent on the metal's work function for many metal/TMDC contacts, which has been reported theoretically and experimentally [108]. This effect prevents the SBH from being

reduced by selecting metals with work function closer to CBE/VBE of the TMDCs (a.k.a. work function engineering, discussed in Chapter 1.4.2)
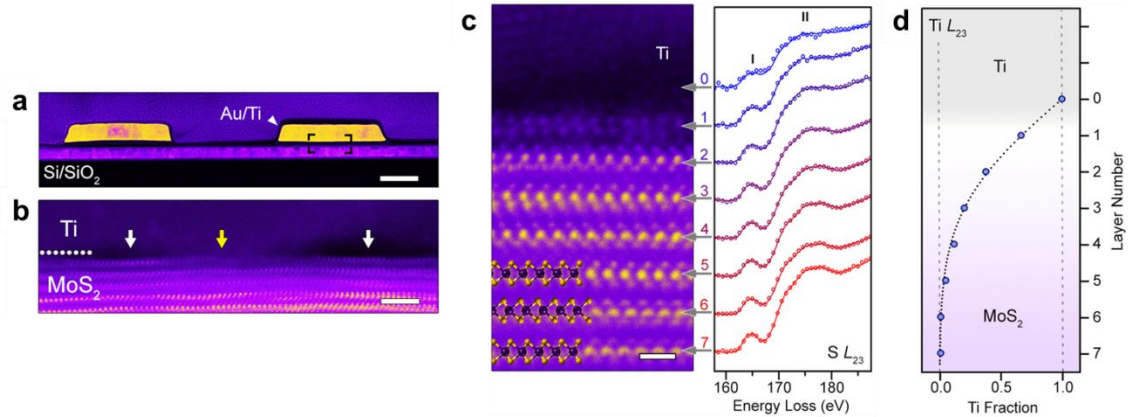
Figure 1.20: Cross-sectional ADF-STEM image of the Ti/MoS$_2$ interface. (a) Low-magnification cross-sectional ADF-STEM image of the FET. The protective amorphous C/Pt layers are also visible here. Scale bar is 0.2 μm. (b) High-magnification image of the Ti-MoS$_2$ interface from the boxed area in (b). An area where Ti is clustered is indicated by a yellow arrow and areas with void pockets by white arrows. Scale bar is 2 nm. (c) Atomic-resolution ADF-STEM image of the MoS$_2$ layers (left) and EELS S L_{23} edge measured from the layers (right). Scale bar is 5 Å. Measured spectra are shown as scatter points and fitted spectra are shown as lines. (d) The fraction of Ti in MoS$_2$ layers. A $y =$ erf (x) fit through the data points. The ADF-STEM characterizations were performed by Ryan Wu at the University of Minnesota.

Theoretical calculation showed that the interface states, thus the FLP, can be eliminated by enlarging the physical separation between the metal and the TMDC [158]. Experimentally, this can be achieved by inserting ultra-thin insulating materials, such as 2D materials (graphene [159, 160] and hBN [161]) and oxides (TiO$_2$ [162-164], MgO [114], and Ta$_2$O$_5$ [165]), in-between the metal and the TMDC. This interfacial layer minimizes the interaction between the metal and the TMDC responsible for the creation of mid-gap states that cause FLP. Once the FLP is mitigated, metals with work function closer to CBE/VBE of the TMDC can be used for n-type/p-type carrier injections,

respectively. However, one downside of this approach is that the thickness of the interfacial layer needs to be carefully controlled. It should be thick enough to suppress FLP but also thin enough to ensure a high current tunneling probability (carriers need to tunnel through the barrier induced by the interfacial layer) [166, 167]. Besides, inserting the interfacial layer increases fabrication complexity.
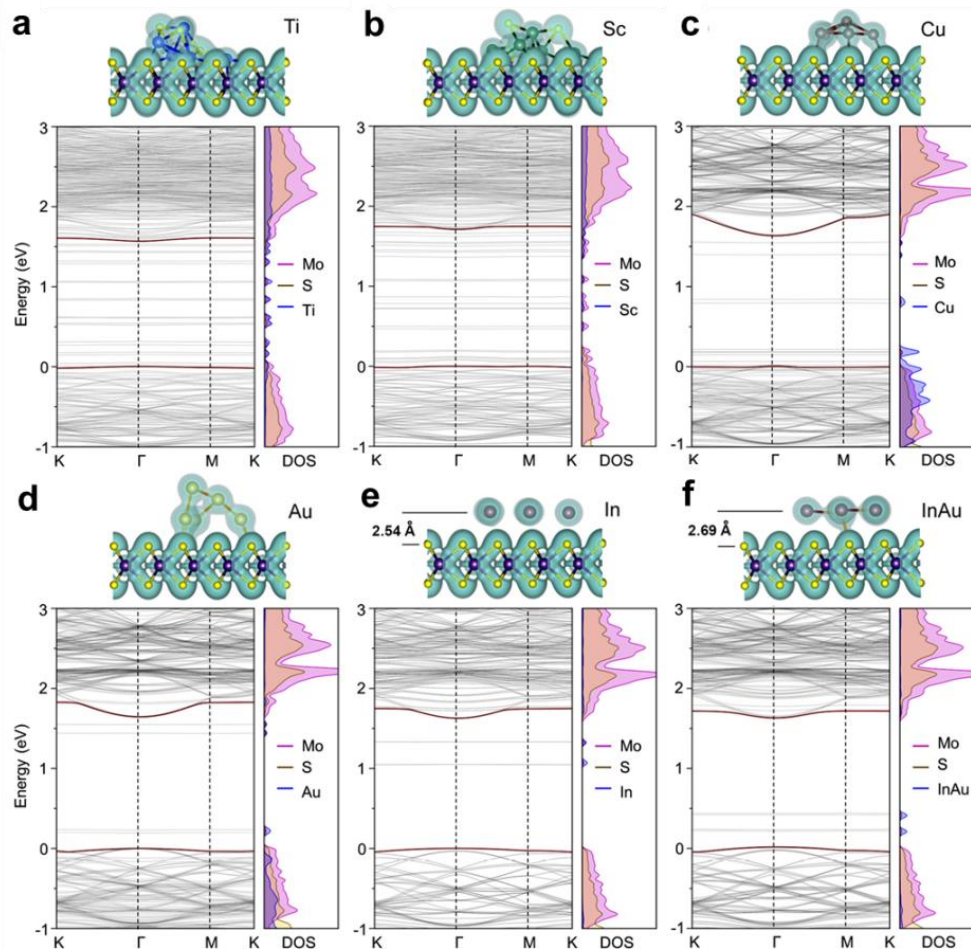
Figure 1.21: The atomic and electronic band structure of monolayer MoS_2 with five atoms of (a) Ti, (b) Sc, (c) Cu, (d) Au, (e) In, and (f) InAu alloy (3 In atoms and 2 Au atoms). The charge densities for all structures are shown in transparent green on the top of the corresponding band structure. The CBM and VBM are highlighted by maroon colors. The calculations were performed by Sagar Udyavara and Prof. Matthew Neurock at the University of Minnesota.

1.4.4 van der Waals (vdW) Gap

Due to a dearth of dangling bonds on the surfaces, high-quality TMDCs, such as mechanically exfoliated flakes, do not tend to form covalent bonds with specific metals (especially for those having low affinity to chalcogen elements) resulting in a vdW gap at the metal/TMDC interface. The vdW gap has been observed experimentally using transmission electron microscopy (TEM) [157, 168, 169], as illustrated in Figure 1.22a [168]. The vdW gap acts like an additional tunneling barrier in series with the inherent Schottky barrier (Figure 1.22b), which makes it more difficult for charge carriers to move into the channel, resulting in higher contact resistance [101, 106, 109]. Moreover, this issue is more prominent in multi-layer TMDCs because the interlayer vdW gaps act as additional resistors.
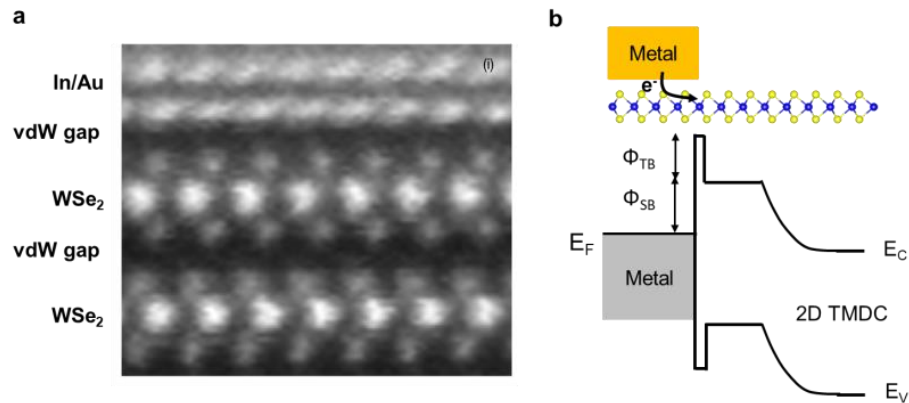
Figure 1.22: (a) Scanning transmission electron microscopy (STEM) image of an In/Au–WSe$_2$ interface, showing a clear van der Waals (vdW) gap between WSe$_2$ and In/Au metal atoms, and a vdW gap between two WSe2 layers. Reprinted with permission from reference [168]. (b) Schematic and corresponding band diagram of a bulk metal/2D TMDC interface with vdW gap for a carrier injected from the metal into the 2D TMDC. E_F, E_C and E_V represent the Fermi level of the metal, and the conduction and valence bands of the 2D TMDC, respectively. Φ_{TB} and Φ_{SB} indicate the tunnel barrier (introduced by the vdW gap) and Schottky barrier heights, respectively.

One approach to avoid this vdW gap is using contact metals that can form covalent bonding or hybridize with the underlying TMDC surface to form a more intimate contact interface [103]. Contact metals having a lower lattice mismatch with TMDCs can result in strong hybridization by maximizing orbital overlapping (covalent bonding) between the contact metal and the chalcogen atoms. Strong hybridization can also be induced by metals having d orbital electrons as they allow for a higher degree of orbital overlapping with the d orbital of the transition metals in TMDCs; for example Ti/Mo/W for MoS_2 [101, 103, 170, 171] and Pd/Mo/W for WSe_2 [101, 103]. However, theory [101] and experiment [157] have shown that strong hybridization can lead to FLP, which might result in a larger SBH.

Another approach to overcome this vdW gap could be to make edge contacts to TMDCs. Due to the presence of unsaturated bonds, edges of TMDCs (made up of transition metal d orbitals) are more chemically active so they can form stronger bonding with the contact metals, thus minimizing the tunnel barrier induced by the vdW gap [101, 103]. Edge contacts also reduce the overall contact volume and area enabling ultimate scalability. Moreover, this approach is particularly effective for multi-layer TMDCs based FETs as each individual layer can be independently contacted from the sides allowing for simultaneous lateral carrier injections, eliminating the interlayer resistances associated with the vertical carrier injections across the interlayer vdW gaps [172, 173]. Due to the difficulty in forming metal edge contacts, edge contacts directly formed between metallic and semiconducting TMDCs (TMDC edge contacts) have been investigated via phase engineering (discussed in Chapter 1.5). R. Kappera *et al.* reported a formation of MoS_2 edge contacts by converting the semiconducting MoS_2 in the contact

regions into its metallic phase via Li ion intercalation [95]. S. Cho *et al.* created 2H/1T′

MoTe$_2$ edge contacts using laser irradiation [174]. However, those methods showed

damage or etching to TMDCs. I demonstrated a MoTe$_2$ FET with low contact resistance

(less than 0.5 kΩ·μm) based on 2H/1T′ MoTe$_2$ edge contacts [17] that are formed through

a phase-selective synthesis process [37]. This synthesis process is also facile and practical

for making other TMDC edge contacts. More on the synthesis and material and electrical

characterizations of the CVD-grown lateral MoTe$_2$ edge contacts is discussed in Chapter

2-4.

1.4.5   Transfer Length

"Current crowding" is a well-known effect in silicon [175, 176] and 2D material

devices [177, 112]. It occurs as the current transfers between metals and underneath

semiconductors over a finite length, leading to a non-uniform current density that is

higher at the edge of the metal contact and decreases exponentially to zero deeper into the

contact [178]. The length from the edge of the contacts to where the current drops to $1/e$

of the current value at the edge is defined as the transfer length, L_T, where e is the base of

the natural logarithm. As the majority of the injected carriers are scattered many times

before entering the channel, this effect can be modeled as a resistor network ([179, 180]),

as illustrated in Figure 1.23.
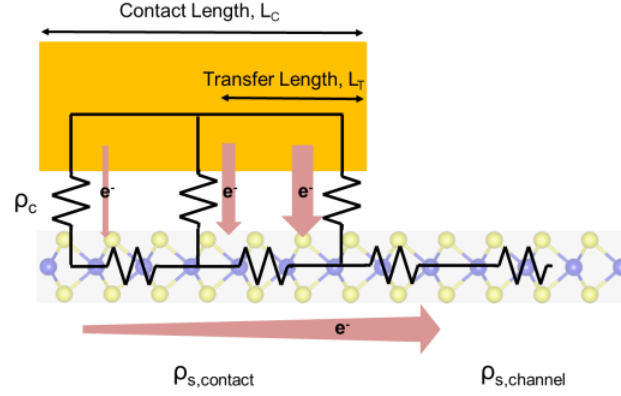
Figure 1.23: Transmission line model of the resistor network near the contact edge. The arrows depict the current density. ρ_c is the specific contact resistivity at the metal/TMDC interface. $\rho_{s,contact}$ and $\rho_{s,channel}$ are the sheet resistivity under the contact and in the channel, respectively.

Due to the large contact resistance at the metal/TMDC interface, the L_T values in metal/TMDC contacts are often long. H. Liu *et al.* reported a 600 nm L_T for monolayer MoS$_2$ with Ti/Au contacts [177] and Y. Guo *et al.* reported a 218 nm L_T for five-layer MoS$_2$ with Au contacts [112]. The contact length, L_C, shrinks with continued scaling of the channel length. However, shrinking the channel length decreases channel resistance, while shrinking L_C increases R_C if L_T is long. For short L_T ($L_C \gg L_T$), $R_C = \sqrt{\rho_C R_S}$ is independent of L_C, where ρ_C is the specific contact resistivity. For long L_T ($L_C \ll L_T$), $R_C = \rho_C/L_C$ increases with decreasing L_C [109, 180]. Therefore, for future scaled FETs based on 2D TMDCs, it is extremely important to minimize L_T to mitigate the effect of contact scaling. As $L_T = \sqrt{\rho_C/R_S}$ where R_S is the sheet resistance of the channel semiconductor, to minimize L_T is to minimize ρ_C. Hence, the solutions for eliminating the SBH, the vdW-induced tunnel barrier, and the FLP effects should all result in shorter transfer length. Particularly, lateral edge contacts made of metallic-semiconducting TMDC junctions (Figure 1.24) could be the ultimate solution for all the aforementioned

issues, as it offers several advantages: (i) no hybridization (FLP effects) at the lateral TMDC interface and the contact metal/metallic TMDC interface; (ii) metallic TMDCs with a Fermi level close to the conduction band or valence band of semiconducting TMDCs can be chosen to lower SBH; (iii) edge contacts to each individual channel layer allowing for lateral carrier injections, thus eliminating interlayer vdW gaps associated resistance; and (iv) the high conductivity of metallic TMDCs results in a small specific contact resistivity, hence a small transfer length.
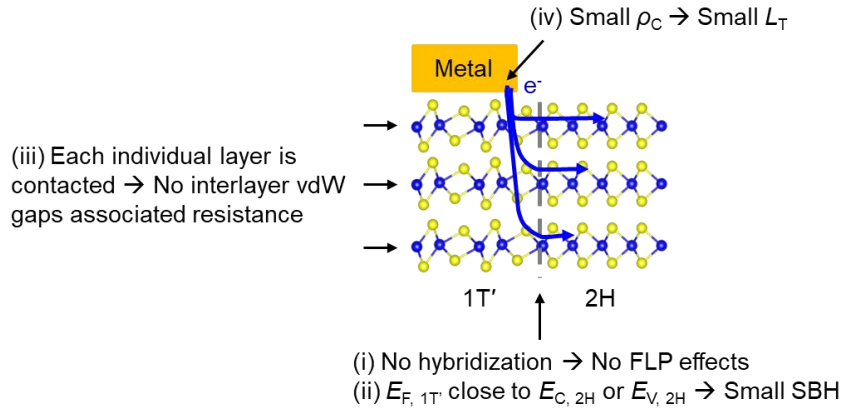
Figure 1.24: Lateral 2D edge contacts made of metallic-semiconducting (1T′-2H) TMDC junctions. It eliminates the SBH, the vdW-induced tunnel barrier, and the FLP effects, resulting in ultra-low contact resistance.

The widely adopted approach to extract the contact resistance and transfer length is the transfer length method (TLM). In a TLM experiment, the total resistances of FETs with different channel lengths (Figure 1.25a) are measured from the output characteristic. Considering one single FET (Figure 1.25b), the measured total resistance consists of two components:

$$R_T = 2R_C + R_{CH} \tag{1.5}$$

where R_C is the contact resistant at source/drain terminal, a combination of the resistance due to the contact metal, the resistance associated with the metal/semiconductor interface, and the resistance of the semiconductor underneath the contact. R_{CH} is the resistance of the device channel, which is related to the sheet resistance of the channel semiconductor, R_S ($\Omega/\square$), as

$$R_{CH} = R_S \frac{L}{W} \tag{1.6}$$

where W and L are the width and length of the channel. R_T then can be expressed as

$$R_T = \frac{R_S}{W} L + 2R_C \tag{1.7}$$

If the total resistance is plotted as a function of channel length (Figure 1.25c), the slope will be the normalized sheet resistance and the y-intercept will be two times the contact resistance. L_T is modeled as $L_T = \sqrt{\rho_C/R_S}$ under the assumption that the effective area of the contact is $L_T W$ [175]. Then the contact resistance and total resistance are:

$$R_C = \frac{\rho_C}{L_T W} = \frac{R_S L_T}{W} \tag{1.8}$$

$$R_T = \frac{R_S}{W} L + 2R_C = \frac{R_S}{W} L + 2 \frac{R_S L_T}{W} = \frac{R_S}{W} (L + 2L_T) \tag{1.9}$$

Therefore, L_T can be extracted from the x-intercept in the plot of R_T vs L. Meanwhile, we have all the details to find the specific contact resistivity, which can be calculated as

$$\rho_C = R_S L_T{}^2 \tag{1.10}$$
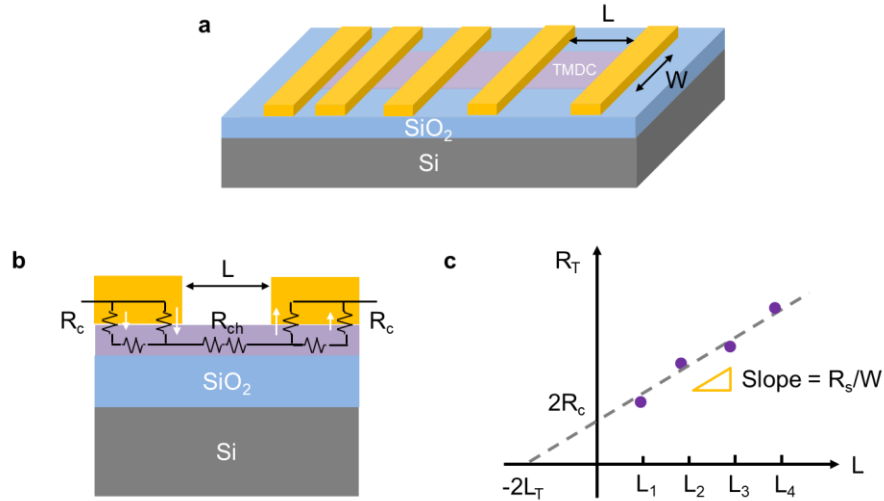
Figure 1.25: Extraction of contact resistance and transfer length using TLM. (a) Device structures for the TLM measurement. (b) Schematic of the resistances in a FET. (c) The plot of total resistance as a function of channel length. The contact resistance R_C, transfer length L_T and sheet resistance of the channel R_S can be extracted.

This method is valid under the assumption that the sheet resistance underneath the contact is the same as that in the channel ($\rho_{s,contact} = \rho_{s,channel}$), which is not always the case due to hybridization at the metal/TMDC interface [101, 181]. For more accurate analysis, parallel 4-probe measurements [182] and fixed channel length method [183] can be considered.

1.5 Phase Engineering

Phase engineering is a viable technique for obtaining metastable phase TMDCs that do not exist or are rarely attained under ambient conditions. Phase engineering mostly includes phase transition and phase-selective synthesis. Phase transition involves the conversion from one phase to another, generally from a stable phase to a metastable phase. The phase transition can be either reversible or irreversible. Phase-selective synthesis involves the direct fabrication of high-purity phase TMDCs or their lateral or

vertical heterostructures. The as-obtained phases by phase-selective synthesis are normally irreversible. More on the phase-selective synthesis is discussed in Chapter 2.

Phase transition between semiconducting 2H and metallic 1T/1T′ phases in several TMDCs (such as MoS_2, $MoSe_2$, $MoTe_2$, and WS_2) has been theoretically predicted and experimentally demonstrated. It has shown promising potential in many applications. For example, unidirectional phase transition from semiconducting phase to metallic phase in the contact regions of TMDCs based FETs can be utilized to form 2D edge contacts for achieving ultra-low contact resistance. Conversely, reversible phase transition in the channel regions can be employed to realize phase-change-based memristive devices (discussed in Chapter 5). Additionally, phase transition has been used to promote hydrogen evolution reaction (HER) activity [184 - 186], enhance energy storage performance of electrode materials in Li-ion batteries [187 - 189], generate higher photocurrent in optoelectronic devices [190], etc.

Understanding the mechanisms of phase transition in TMDCs can lead to better utilization in the future. This chapter reviews three main mechanisms for inducing phase transition between 2H and 1T/1T′ phases in TMDCs: (i) charge doping, (ii) thermal treatment, and (iii) strain engineering.

1.5.1 Charge Doping

Theoretical calculation shows that charge doping can effectively lower the transition barrier between the 2H and 1T′ phases [191, 192]. Excessive electrons injected into the 2H phase occupy the lowest available energy states in the conduction band lifting the total energy of the 2H phase above that of the 1T′ phase, leading to the destabilization

of the 2H phase, hence a structural phase transition from 2H to 1T′ [192, 193]. Even for

monolayer $MoTe_2$ which has the smallest free energy difference between its 2H and 1T′

phase (~35 meV per unit cell [33]) among all group-VI TMDCs, the theoretically

calculated charge doping concentration for the 2H/1T′ phase transition is ~10^{13}-10^{14} cm^{-2}

[192], which is one order magnitude higher than the highest value that can be achieved by

conventional high-κ dielectrics (such as HfO_2). However, this high level of charge

concertation can be induced by electrostatic [194] or chemical doping [95]. The electron-

double-layer (EDL) surface gating using polymer electrolytes can induce an electrostatic

doping concentration up to 10^{15} cm^{-2} at a few volts [195-197]. Y. Wang *et al.* has realized

a reversible electrostatic-doping-driven 2H/1T′ phase transition in exfoliated monolayer

$MoTe_2$ through an ionic liquid (DEME-TFSI) (Figure 1.26a-b) [194]. Chemical doping

has been shown to be able to induce higher charge concentrations than electrostatic

doping. Kappera *et al.* used n-butyl lithium solution to chemically induce 2H to 1T′ phase

transition in monolayer 2H-MoS_2 (Figure 26c-d) [95], which requires higher charge

doping than that needed for the phase transition in monolayer $MoTe_2$. Alkali ions (A),

such as Li^+, K^+, Na^+, can be intercalated into the layer interval of certain layered TMDCs

to from A_xMX_2 during which electrons are transferred from alkali ions into TMDCs

[198]. This intercalation is due to the large interval spacing (0.6-0.7 nm) of layered

TMDCs and the strong interaction between alkali ions and TMDCs. Theoretically, alkali

ions can intercalate between every layer interval and dope each individual layer for thick

TMDCs.
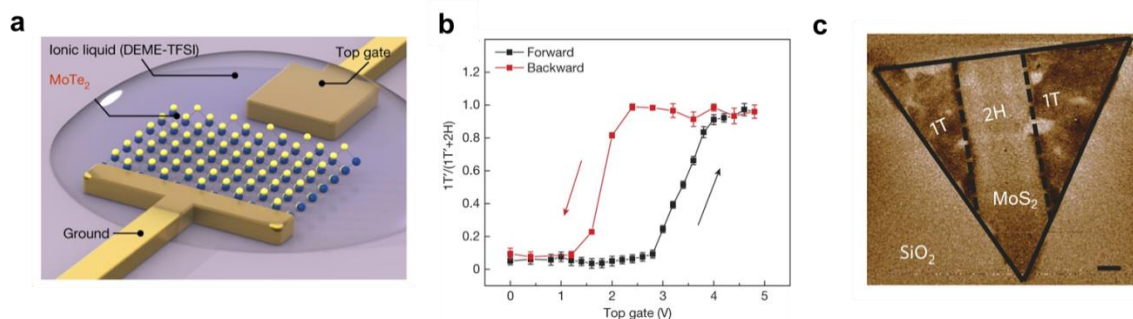
Figure 1.26: Phase transition by charge doping: (a-b) electrostatic doping and (c) electrochemical doping. (a) Schematics of a MoTe$_2$ monolayer FET covered with an ionic liquid electrolyte. (b) Gate-dependent Raman intensity ratios of the 1T′(A$_g$) mode over the sum of the 1T′(A$_g$) and 2H(A_1') modes under an electrical field scan showing a reversible phase transition. Reprinted with permission from reference [194]. (c) Electrostatic force microscopy phase image of a monolayer MoS$_2$ nanosheet showing different contrast between locally patterned 2H and 1T′ phases. The scale bar is 1 μm. Reprinted with permission from reference [95].

1.5.2　Thermal Treatment

Te vacancies are common in thin layer weak-bonded TMDC films, such as MoTe$_2$, due to the close electronegativity of the transition metal and chalcogen atoms [199]. These vacancies or defects act as precursors leading to phase transition at elevated temperatures due to the frequent vibrations of atoms and the formation of new chemical bonds. Te vacancies can also be induced by laser irradiation [174, 200]. S. Cho *et al.* reported phase transition from 2H to 1T′ in few-layer MoTe$_2$ via laser irradiation (Figure 1.27a-b) [174]. Te vacancy induced by laser irradiation is identified as the key origin of the phase transition at high temperature (400 ^{o}C) elevated by laser irradiation itself. S. Kim *et al.* demonstrated the reversed phase transition from 1T′ to 2H using the same laser treatment. Both experiments show a thinning effect and unidirectional phase transition from one phase to another [200].

1.5.3 Stress Engineering

It has been proven theoretically and experimentally that tensile strain can lower the activation energy of the phase transition (Figure 1.27c) [32, 201, 202]. DFT simulation results by Duerloo *et al.* showed that an equibiaxial tensile strain of more than 10 N m^{-1} is needed to induce phase transition for most monolayer TMDCs, for example 12.8 N m^{-1} for MoS_2, which is near their breaking threshold. However, $MoTe_2$ requires a considerably less tensile strain, less than 6.9 N m^{-1} [32]. Experimentally, S. Song *et al.* observed reversible phase transition in suspended 2H $MoTe_2$ flakes (thickness of ~20 nm) under a small tensile strain of 0.2% applied through an atomic force microscopy (AFM) tip (Figure 1.27d) [201]. However, the converted regions are not uniform with coexistence of 2H and 1T′ phases. Theoretical calculation by A. P. Nayak *et al.* revealed that phase transition can also be achieved under compressive stress [203].
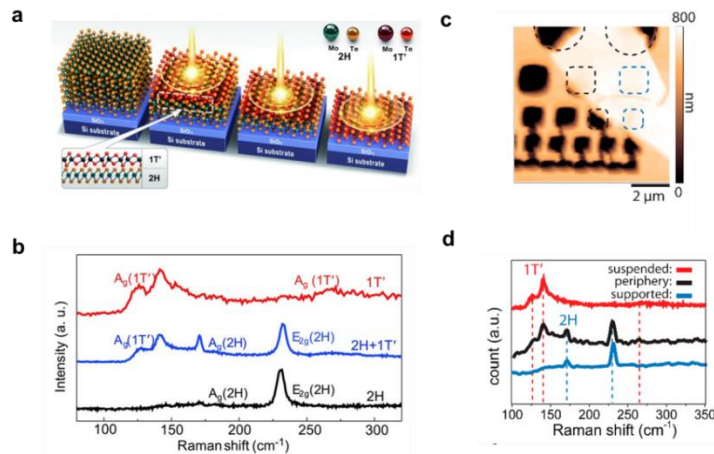
Figure 1.27: Phase transition by (a-b) laser irradiation and (c-d) tensile strain. (a) Schematic representation of the laser-irradiation process. (b) The evolution of Raman spectroscopy from 2H phase (bottom) to 1T' phase (top). Reprinted with permission from reference [174]. (c) AFM height image (left) of a suspended 2H-$MoTe_2$ flake. (d) Raman spectra (right) taken at the outside (supported), periphery, and the center (suspended) of the cavities showing different Raman signatures of 2H and 1T′ under 0.2% strain. Reprinted with permission from reference [201]. Copyright (2016) American Chemical Society.

1.6 Dissertation Outline

This thesis is organized as following. Chapter 2 discusses the *in-situ* synthesis of lateral 2H/1T′ MoTe$_2$ homojunctions using a flux-controlled phase-engineering method and the detailed material characterizations of the *in-situ*-grown MoTe$_2$ homojunctions. Chapter 3 discusses the detailed electrical characterizations of the *in-situ*-grown MoTe$_2$ homojunctions. Chapter 4 demonstrates a two-step lithographic synthesis technique based on the flux-controlled method for the fabrication of various lateral TMDC junctions. Chapter 5 demonstrates a reversible phase transition in pre-lithiated few-layer MoS$_2$ fakes by gate-controlled lithium intercalation through a solid lithium-ion based electrolyte.

CHAPTER 2 *IN-SITU* SYNTHESIS OF LATERAL MOTE$_2$ HOMOJUNCTION

Lateral metallic-semiconducting (MS) TMDC junctions are of particular interest as they are ideal edge contacts for achieving ultra-low contact resistance for TMDC-based FETs, owing to the mitigation or elimination of SBH, vdW gap, FLP and current crowding. The diverse work functions of metallic and semiconducting TMDCs also allows for work function engineering to achieve complementary FET applications. Furthermore, their thin body nature enables ultimate scalability. In order to use them in future scaled logic electronics, facile and scalable synthetic strategies are needed. Lateral MS TMDC junctions can be obtained through the phase transition strategies including charge doping, thermal treatment and strain engineering (discussed in Chapter 1.5). However, those strategies are not scalable and have several shortcomings with regard to the quality of the as-obtained materials: (i) They may induce vacancies or cause damages, such as electrochemical reaction by ionic electrolyte, etching by laser irradiation, and exfoliation by lithium intercalation; (ii) The as-obtained phases may not be homogenous, such as a mixed of 2H and 1T′ MoTe$_2$ phases obtained by tensile strain; and (iii) The as-obtained phases may not preserve their phases when the external force is withdrawn (reversible transition), such as the transition induced by electrostatic doping.

Recently, phase-selective synthesis (mostly based on CVD) has been developed to fabricate large-scale single-phase films [204] or lateral polymorphic heterostucture (also called homojunction) films [37, 205-208]. Most of the reported syntheses are on MoTe$_2$,

as it has the smallest free energy difference between its semiconducting 2H and metallic 1T′ phases among all group-VI TMDCs, allowing for easy controllability of the phase and the in-situ formation of homojunctions. The *in-situ* synthesis of lateral 2H/1T′ MoTe$_2$ homojunctions have been achieved by various means including tellurization-velocity-dependent phase evolution [205, 206], post-growth annealing to induce a 2H to 1T′ phase transition [207], temperature-selective phase stabilization in the presence of NaCl [208], and flux-controlled phase engineering [37].

The flux-controlled phase engineering method by tellurization of Mo nanoislands is of particular interest given its robustness and ability to form large grains [209]. In this method, chalcogen flux plays a key role in determining the phase of as-obtained MoTe$_2$. For example, a sufficient amount of Te will lead to 2H phase whereas an insufficient supply of Te will result in 1T′ phase [37, 210]. However, a comprehensive study combining detailed microstructural and electrical properties of 2H/1T′ MoTe$_2$ interfaces formed via the flux-controlled growth technique has not been reported. This chapter introduces a flux-controlled phase engineering method [37] and discusses detailed material characterizations of the as-synthesized 2H/1T′ MoTe$_2$ homojunctions including Raman spectroscopy, AFM, and TEM. The material synthesis was done by Youngdong Yoo and Lun Jin at the University of Minnesota, and the TEM was done by Huairuo Zhang at NIST. The results present in this chapter are from one of my publications [17].

2.1 Flux-Controlled Phase Engineering Method

Few-layer 2H, lateral 2H/1T′ homojunctions and 1T′-MoTe$_2$ are synthesized by the flux-controlled tellurization of Mo nanoislands in a horizontal hot-wall single-zone

54

furnace (Figure 2.1a). The phase of few-layer MoTe$_2$ is controlled by changing Te atomic flux controlled by the temperature of the reaction vessel. Few-layer 2H-MoTe$_2$ is formed with high Te flux, while few-layer 1T′-MoTe$_2$ is obtained with low Te flux. With medium flux, few-layer in-plane 2H/1T′ MoTe$_2$ homojunctions is achieved.

The synthesis starts by depositing Mo nanoislands on SiO$_2$/Si substrates through electron beam evaporation (EBE) under high vacuum. The deposited Mo nanoislands have heights of about 1-3 nm and widths of about a few hundred nanometers (Figure 2.1b). Then, the Mo nanoislands on SiO$_2$/Si substrates are placed face down on a 5 cm × 2 cm × 2 cm alumina boat containing a Te lump placed at the center of the heating zone in a 3-in. quartz tube, followed by annealing in Ar/H$_2$ (5 sccm/5 sccm) environment at atmospheric pressure. The annealing temperature determines Te flux, thereby the final phase of the film. The furnace was ramped to 635 ˚C (high Te flux), 585 ˚C (medium Te flux), and 535 ˚C (low Te flux) in 15 minutes and was kept at the temperatures for an hour for the synthesis of few-layer 2H, lateral 2H/1T′, and 1T′-MoTe$_2$, respectively. After the reactions, Ar was turned to the flow rate of 100 sccm and the furnace was rapidly cooled down to room temperature with the furnace lid open. The thickness of the film was in the range of 3.5 to 15 nm depending on the variations in growth conditions and the initial Mo thickness. More details of the synthesis are provided in Appendix C.1.

Optical images (Figure 2.1c-e) of few-layer 2H-, lateral 2H/1T′, and 1T′-MoTe$_2$ show that the films have high uniformity. A sharp optical contrast between 1T′- and 2H-domains is due to the change in visible absorption spectrum of 2H- and 1T′- MoTe$_2$.
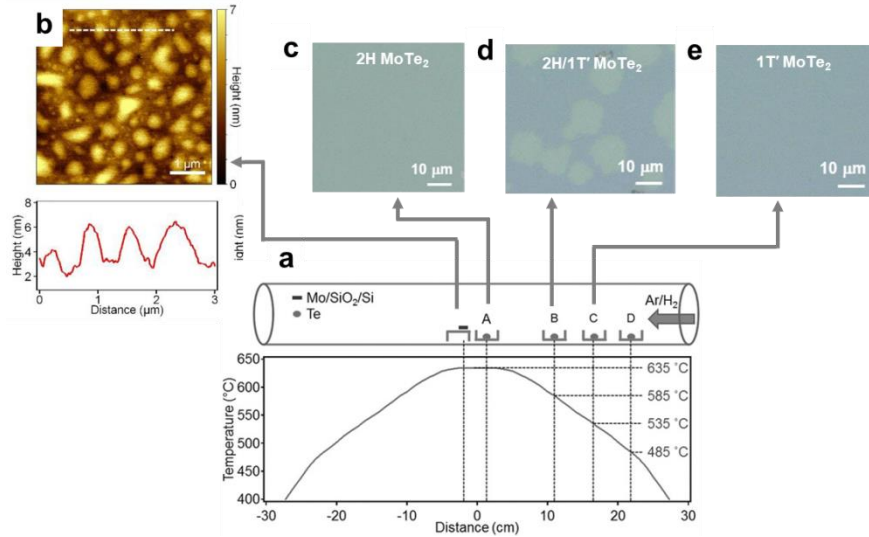
Figure 2.1: (a) Schematic illustration showing the experimental setup for the flux-controlled phase-engineering synthesis (top) and the temperature profile of the furnace (bottom). The center of the furnace is heated at 635 °C. For the syntheses of few-layer 2H-, lateral 2H/1T′, and 1T′-MoTe$_2$, Te lump is placed at positions of A (635 °C), B (585 °C), and C (535 °C), respectively. (b) AFM height image (top) and line profile (bottom) of Mo nanoislands deposited on SiO$_2$/Si substrates. (a) and (b) are reprinted with permission from reference [37]. (c-e) Optical images of as-synthesized few-layer 2H-, lateral 2H/1T′, and 1T′-MoTe$_2$ films.

2.2 Material Characterizations of 2H/1T′ MoTe$_2$ Homojunctions

As-synthesized MoTe$_2$ is characterized by Raman Spectroscopy, AFM, and TEM. More characterizations including X-ray photoelectron spectroscopy (XPS), and X-ray powder diffraction (XRD) are provided in Appendix B.2 [37].

2.2.1 Raman Spectroscopy

An optical image of an as-synthesized few-layer 2H/1T′ MoTe$_2$ homojunction is shown in Figure 2.2a. Raman spectra (Figure 2.2b) taken from the 2H- and 1T′- MoTe$_2$ regions exhibit phase-specific characteristic Raman peaks, which are the A$_{1g}$ (170.9 cm^{-1}) and E$_{2g}$ (233.5 cm^{-1}) modes for 2H-MoTe$_2$ and the B$_g$ (163.0 cm^{-1}) and A$_g$ (260.1

56

cm^{-1}) modes for 1T′-MoTe$_2$. The crystal structures of as-synthesized few-layer 2H- and 1T′- MoTe$_2$ were confirmed by XRD (Figure B.1). The elemental composition of few-layer 2H- and 1T′- MoTe$_2$ analyzed using XPS (Figure B.2) reveals that the Te/Mo atomic ratio of 1T′-MoTe$_2$ is about 1.86 when the value of the Te/Mo atomic ratio of 2H-MoTe$_2$ is normalized to 2.00. The Te deficiency in 1T′-MoTe$_2$ could be attributed to the insufficient Te supply during the growth.
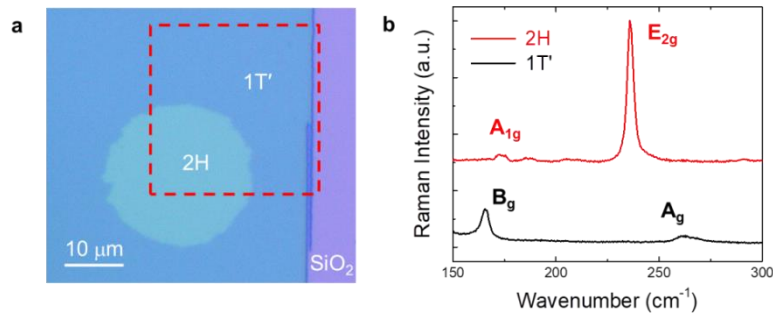
Figure 2.2: (a) Optical image of a MoTe$_2$ homojunction grown on a SiO$_2$/Si substrate. The right side was scratched off by tweezers. (b) Raman spectra taken from the 1T′ and 2H regions in (a) with an excitation laser with a wavelength of 633 nm and a power of 150 μW.

2.2.2 Atomic Force Microscope

AFM measurement was performed to verify the thickness and roughness of the as-synthesized few-layer 2H/1T′ MoTe$_2$ homojunction. The AFM height map of the region in the red dashed box in Figure 2.3a is shown in Figure 2.3a. The film possesses a root-mean-square (RMS) roughness of ~0.9 nm. Since the underlying SiO$_2$/Si substrates has a RMS of 0.5-1 nm, the surface of the film is quite smooth. The height profile across the film edge (line 1 in Figure 2.3a) shows that the thickness of the film is around 8 nm (Figure 2.3b). It should be noted that the thickness of the films can vary by a few nm from batch to batch due to variations in growth conditions and the thickness of the initial

deposited Mo. By optimizing the growth conditions, this method is capable of growing homojunction films with a thickness of down to 3.5 nm (five-layer) [37]. The height profile across the homojunction (line 2 in Figure 2.3a) indicates that there is no systematic change in height across the homojunction (Figure 2.3c). The boundary between two phases is still slightly visible in the height map, which could be attributed to the local variations in the texturing of the 1T′ and 2H regions (discussed in Chapter 2.2.4).
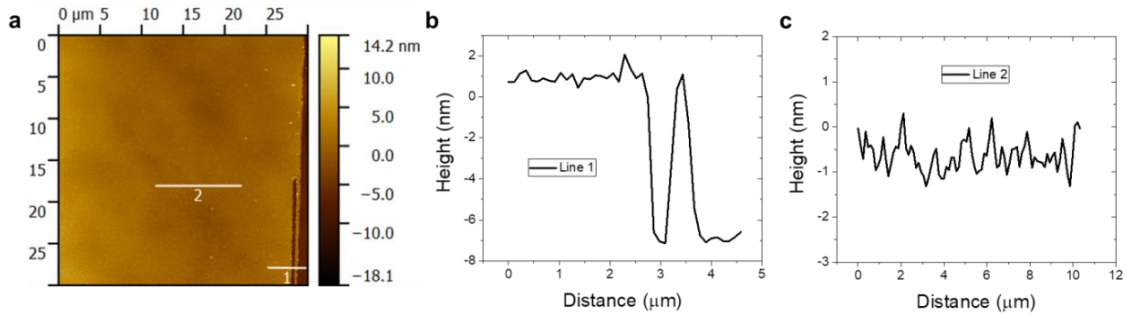
Figure 2.3: (a) AFM height map of the region in the red dashed box in Figure 2.2a. (b) Height profile along the horizontal white line 1 in (a) showing that the thickness of the film is 8 nm. (c) The height profile along the horizontal white line 2 showing no significant height difference across the homojunction.

2.2.3 Transmission Electron Microscopy

TEM was employed to gain insight into the microstructural details of the 2H/1T′ MoTe$_2$ homojunction. Sample preparation is provided in Appendix C.2. Figure 2.4a shows a low-magnification bright-field (BF) TEM image of the plan-view sample supported on lacey carbon. The round region of darker contrast is identified as having a 2H structure, and the surrounding brighter matrix is identified as having the 1T′ structure. Selected area electron diffraction pattern (SAEDP) analysis taken from regions of a diameter of 600 nm shows the 2H region being a near single-crystal oriented with the

[001]$_{2H}$ normal to the plane of the film (Figure 2.4b), and the 1T′ matrix is polycrystalline but textured so that the [001]$_{1T'}$ direction is out of the film plane (Figure 2.4c). Detailed analysis of the polycrystalline diffraction rings supporting the strong [001]$_{1T'}$ texture is given in Figure B.3 and Table B.1 of Appendix B.3.
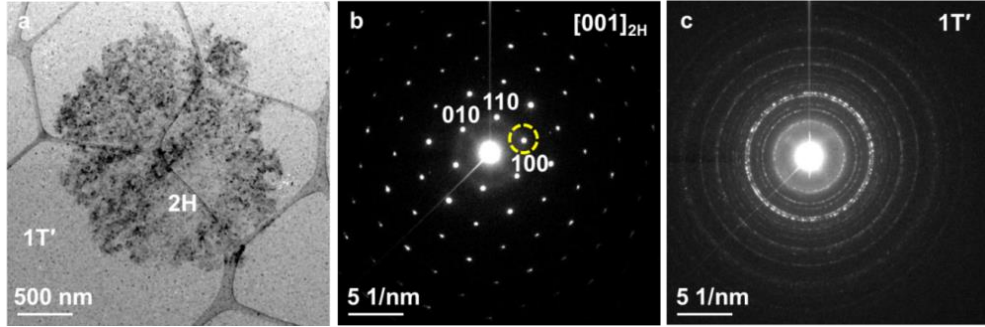
Figure 2.4: Plan-view bright-field TEM characterization results of as-synthesized 2H/1T′ MoTe$_2$ homojunction. (a) Low-magnification bright-field TEM image showing the round region of 2H phase surrounded by the 1T′ phase matrix. (b,c) Selected-area electron diffraction patterns (SAEDPs) from the round region and matrix showing the near-single-crystal pattern of the 2H phase and polycrystalline diffraction rings of the 1T′ phase, respectively.

Figure 2.5a shows a dark-field (DF) TEM image taken with an aperture at the (100) diffraction spot shown in Figure 2.4b with a yellow circle. Most of the round region is bright and consistent with the SAEDP analysis of near-single-crystallinity of the 2H phase. The dark areas shown by the yellow circles have a smaller thickness than the surrounding area (discussed in Appendix B.4). The speckling contrast (Figure 2.5b) is due to the thickness variation and slight local misorientation of the 2H domains. Figure 2.5c shows a dark-field image taken from the 2H/1T′ interface region with a large aperture (placed as shown in the inset), evidencing the polycrystalline 1T′ grains.
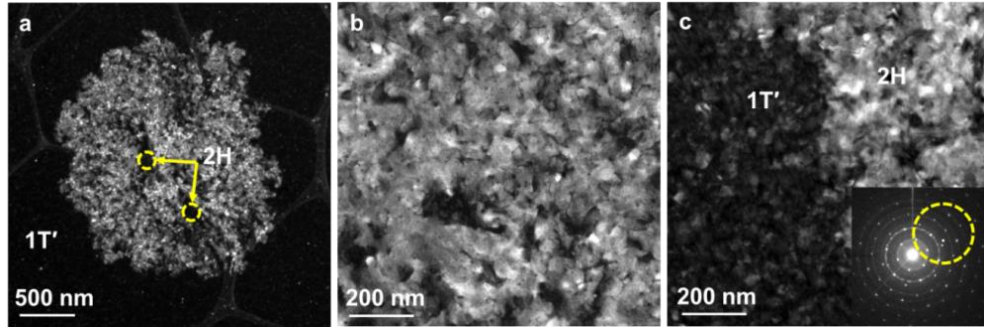
Figure 2.5: Plan-view dark-field TEM characterization results of as-synthesized 2H/1T′ MoTe$_2$ homojunction. (a) Dark-field image with an aperture at the (100) diffraction spot in Figure 2.4(b) showing the well-defined 2H/1T′ interface and (b) zoomed-in image demonstrating local structural variation in the 2H phase. (c) Dark-field image taken from the 2H/1T′ interface region with a large aperture (placed as shown in the inset) showing the polycrystalline 1T′ grains.

High-resolution TEM (HRTEM) observation shows a structural continuity at the 2H/1T′ interface region (Figure 2.6a). Figure 2.6b,c show typical HRTEM images taken from the 2H region and the 1T′ matrix, respectively. The insets of projected atomic models and corresponding simulated HRTEM images show a good match with the hexagonal and orthorhombic structures of 2H and 1T′ along their [001] zone axes, respectively.
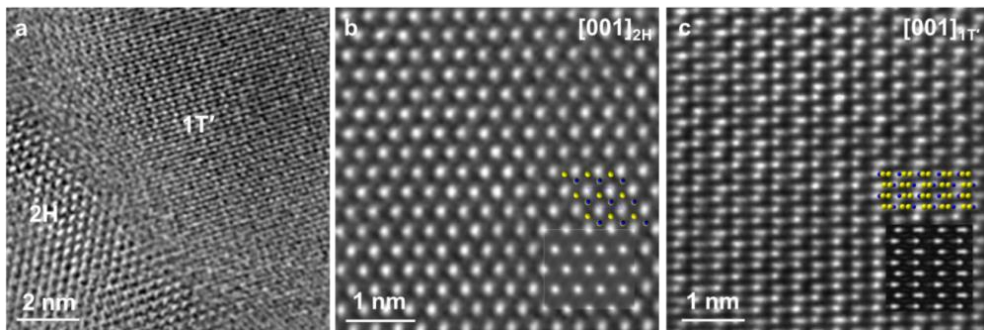
Figure 2.6: Plan-view high-resolution TEM characterization results of as-synthesized 2H/1T′ MoTe$_2$ homojunction. (a) HRTEM image showing structural continuity at the homojunction. (b,c) HRTEM images with insets of projected atomic models and corresponding simulated HRTEM images showing a good match with the hexagonal and orthorhombic structures of 2H and 1T′ along their [001] zone axis, respectively.

2.2.4 Scanning Transmission Electron Microscopy

Aberration-corrected STEM was further employed to characterize the homojunction film. Sample preparation is provided in Appendix C.3. Figure 2.7a shows a low-magnification low-angle annular dark-field (LAADF) STEM image of a round 2H region surrounded by a 1T′ matrix in the plan-view sample. The 2H region has a stronger intensity than the 1T′ matrix, apparently due to electron channeling effect along the $[001]_{2H}$ direction. A zoomed-in LAADF-STEM image shows mottled contrast in the near-single-crystalline 2H region and nanosize polycrystalline particles in the 1T′ matrix (Figure 2.7b), which arises due to the thickness variations and slight local misorientations of the 2H domains and the polycrystalline 1T′ matrix. Figure 2.7c,d shows typical high-resolution STEM (HRSTEM) images taken from 2H and 1T′ regions along the [001] zone axis, respectively. The typical honeycomb structure of the 2H phase is identified in the entire round region, and no presence of other structures such as 1T′ and 3R [211] is observed. Figure 2.8a shows an HRSTEM image of a large area from the mottled 2H region, with the corresponding fast Fourier transform (FFT) image in the inset showing the single crystallinity. This image confirms the thickness variation and slight misorientation in local areas. The apparent downtrend of the intensity profile from A➔B suggests a decreasing thickness in this region (Figure 2.8b). Figures 2.8c-e show the zoom-in images of the selected areas SA-1, SA-2 and SA-3 shown in Figure 2.8a, as well as their corresponding FFTs, evidencing the local misorientation in SA-2.
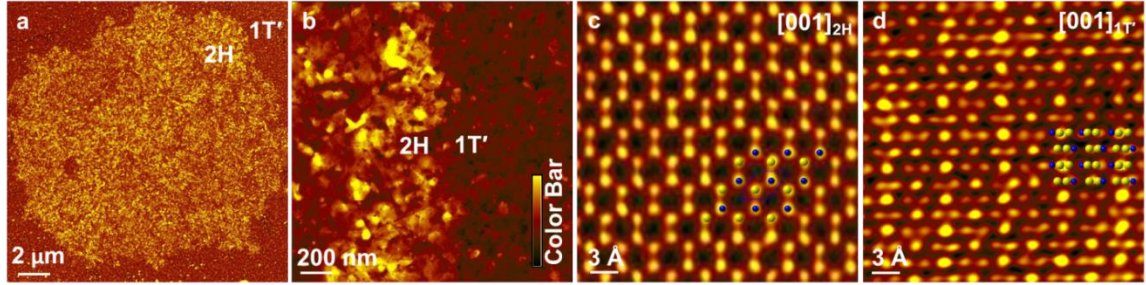
Figure 2.7: STEM characterization of plan-view samples of as-synthesized 2H/1T′ MoTe$_2$ homojunction. (a) Low-magnification LAADF-STEM image showing the round 2H region surrounded by the 1T′ matrix in the plan-view sample. (b) Zoomed-in LAADF-STEM image showing mottled contrast in the 2H region and the polycrystalline 1T′ matrix. (c,d) Typical HRSTEM images with matching atomic projections of the corresponding 2H and 1T′ phases, respectively.
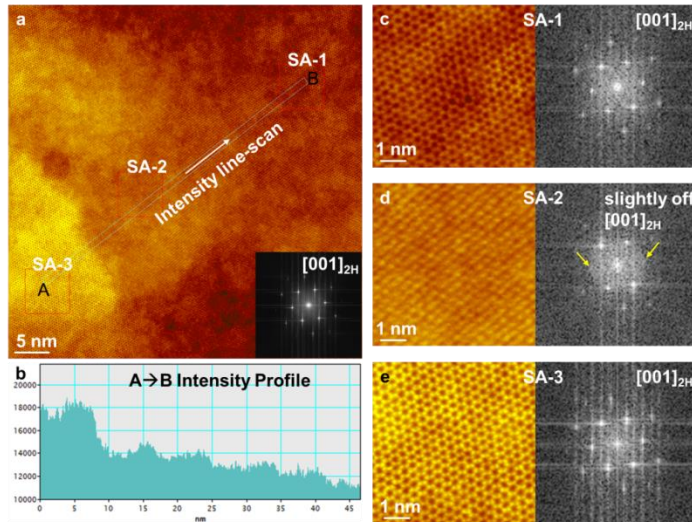
Figure 2.8: HRSTEM image of a large area from the mottled 2H region with the corresponding FFT image in the inset. The positions of an intensity line-scan A→B, and three selected areas for FFT are illustrated (SA-1, SA-2, SA-3). (b) Intensity profile showing the thickness variation from A→B. (c-e) The zoom-in images of the selected areas and their corresponding FFTs showing the local misorientation in SA-2.

Figure 2.9a-c shows HRSTEM images of the 2H/1T′ interface region, demonstrating the 2H phase connecting seamlessly with the neighboring randomly orientated 1T′ grains.
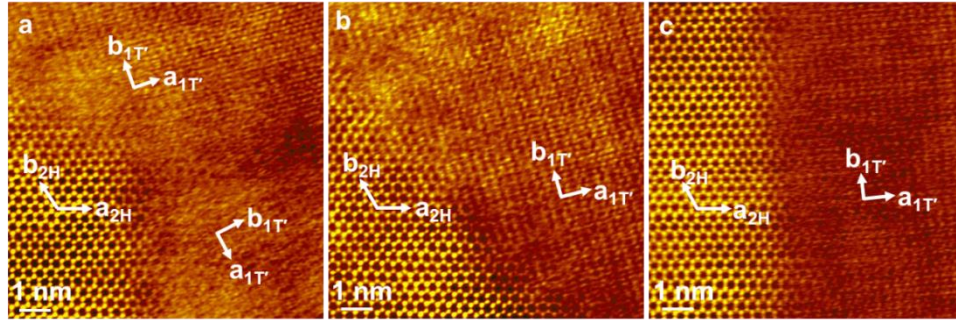
Figure 2.9: (a-c) HRSTEM images showing the 2H connecting seamlessly with the neighboring randomly orientated 1T′ grains.

The homojunction film was further characterized with cross-sectional STEM. Figure 2.10a shows a cross-sectional STEM image capturing both the 2H and 1T′ regions. The film thickness varies between 8.5 and 12.9 nm along a 20 μm long TEM lamellar sample. As shown by the yellow arrows in Figure 1.10a, the 1T′ region is composed of nanosized grains which were identified as randomly textured along the $[001]_{1T'}$ out-of-plane direction. In contrast, the film in the 2H region is continuous, and very few domain boundaries were observed; some thickness variations are shown by the purple arrows. Figure 2.10b-e shows typical HRSTEM images taken from the 2H region (Figure 2.10b,c) and 1T′ region (Figure 2.10d,e) which are well matched with the atomic models of 2H and 1T′, respectively.
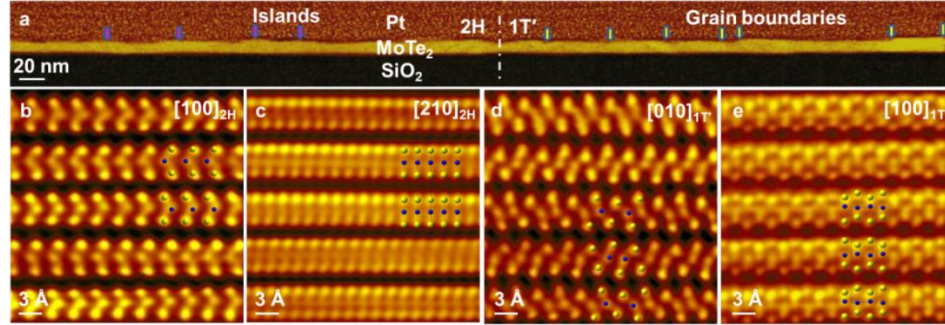
Figure 2.10: STEM characterization of cross-sectional samples of as-synthesized 2H/1T′ MoTe$_2$ homojunction. (a) Low-magnification cross-sectional STEM image showing the thickness variations in the 2H region and grain boundaries in the 1T′ region. (b-e) Typical HRSTEM images taken from the 2H (b,c) and 1T′ (d,e) regions. False colors are added to aid the eye.

2.3 Summary

A flux-controlled phase engineering method by tellurization of Mo nanoislands to form large-area MoTe$_2$ films has been demonstrated. Using this method, few-layer 2H-, lateral 2H/1T′ homojunctions and 1T′-MoTe$_2$ are obtained with high, medium, and low Te flux, respectively. The as-obtained lateral 2H/1T′ MoTe$_2$ homojunction films are composed of randomly distributed round 2H-MoTe$_2$ domains stitching seamlessly to the 1T′-MoTe$_2$ matrix with no significant thickness difference across the junctions. The 2H-MoTe$_2$ domains are near-single-crystalline whereas the 1T′-MoTe$_2$ matrix is polycrystalline with nanosized grains.

CHAPTER 3   ELECTRICAL CHARACTERIZATIONS OF *IN-SITU*-GROWN 2H/1T′ MOTE$_2$ HOMOJUNCTION

Whether the lateral 2H/1T′ MoTe$_2$ homojunction synthesized by the flux-controlled phase engineering method can be used an ideal 2D edge contacts for achieving low contact resistance depends on the band alignment at the 2H/1T′ interface. In order to investigate the carrier transport at the 2H/1T′ interface, MoTe$_2$ FETs with phase-engineered 1T′ contacts are fabricated and characterized using the *in-situ*-grown 2H/1T′ MoTe$_2$ homojunctions. This chapter compares the room-temperature and temperature-dependent carrier transports at the metal (Ti)/2H, metal (Ti)/1T′, and 2H/1T′ interfaces through detailed electrical characterizations. Contact resistance at the metal (Ti)/2H and metal (Ti)/1T′ interfaces are extracted. Bias-dependent Schottky barrier behaviors at the metal/2H and 2H/1T′ interfaces are also discussed. The results present in this chapter are from one of my publications [17].

3.1   Fabrication of *in-situ*-Grown MoTe$_2$ Homojunction FETs

Few-layer 2H/1T′ MoTe$_2$ homojunction film was synthesized on Si substrates with 300 nm thermal oxide using the flux-controlled phase engineering method discussed in Chapter 2. The thickness of the as-synthesized film was ~8 nm, confirmed by AFM measurements (Figure 2.3b). To fabricated MoTe$_2$ homojunction FETs, alignment marks were first patterned, and Ti (10 nm)/Au (35 nm) metal was deposited to form alignment marks for subsequent process steps. Next, mesa regions were patterned and etched into the MoTe$_2$ to form rectangular areas consisting of 2H, 1T′, and 2H/1T′ nanosheets. Contacts to the MoTe$_2$ were formed by patterning and lifting off Ti (10 nm)/Au (80 nm)

metal. Details of the device fabrication are provided in Appendix C.4. Three types of devices were fabricated: (1) 2H-only devices where the channel consisted of 2H phase and the metal pads were contacted to the 2H phase; (2) 1T′-only devices where the channel consisted of 1T′ phase and the metal pads were contacted to the 1T′ phase; and (3) 2H/1T′ devices where the channel consisted of 2H phase and the metal pads were contacted to the 1T′ phase. An optical image of a 2H/1T′ MoTe$_2$ homojunction FET is shown in Figure 3.1a. Raman mapping of phase-specific phonons was used to further confirm phase identity in the channel of the FET. Raman maps of the 2H-MoTe$_2$ E$_{2g}$ peak (Figure 3.1b) and 1T′ MoTe$_2$ B$_g$ peak (Figure 3.1c) show a sharp interface between the 2H and 1T′ MoTe$_2$ regions.
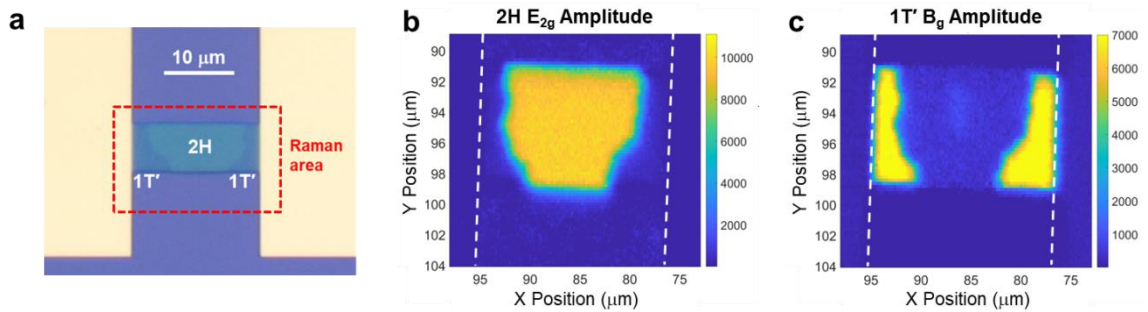
Figure 3.1: Raman mapping of 2H/1T′ MoTe$_2$. (a) Optical image of a 2H/1T′ device. Both the 1T′ and 2H-MoTe$_2$ films are ~6-nm thick in this region. (b)-(c) Raman intensity maps of the E$_{2g}$ mode of the 2H phase and the B$_g$ mode of the 1T′ phase of the region in the red rectangle in (b). White dashed lines are the borders of the contact fingers.

In the following chapters, I compare transport characteristics of all three types of devices and extract the contact resistances at the metal/2H and the metal/1T′ interface (Chapter 3.2) and the energy barrier at the metal/2H and the 2H/1T′ interface (Chapter 3.3 and 3.4).

3.2 Transport at Metal/2H and Metal/1T′ Interfaces

The contact resistances of 1T′-only and 2H-only devices were measured under vacuum using the transfer length method (TLM, discussed in Chapter 1.4.5), as shown in Figure 3.2a,b. The contact resistance of Ti/Au to the 1T′ MoTe$_2$ was found to be 0.47 ± 0.03 kΩ·μm, and the sheet resistance of 1T′ MoTe$_2$ was 2.65 ± 0.09 kΩ/□ at zero back-gate voltage, V_{BG}. The 1T′ contact resistance value is comparable to the best value reported so far for phase transitioned MoS$_2$-based FETs (200−300 Ω·μm) [95] and, to the best of our knowledge, is the lowest reported for MoTe$_2$. Conversely, the contact resistance of the Ti/Au metal to 2H-MoTe$_2$ was found to be 15.6 ± 0.58 MΩ·μm with a sheet resistance of the 2H phase of 4.67 ± 0.7 MΩ/□ at $V_{BG} = -100$ V. Thus, the contact resistance is reduced by 4 orders of magnitude by using the 1T′ contacts. The back-gate dependence of the contact resistance of the 2H-only device is shown as an inset in Figure 3.2b. The contact resistance increases with increasing back-gate voltage, V_{BG}, as the device turns off.

The room-temperature transport characteristics of 1T′-only and 2H-only devices. The room-temperature transfer characteristics showing drain current, I_D vs V_{BG}, of the 1T′-only and 2H-only devices are shown in Figure 3.2c. The 1T′-only device shows a high drive current of 245 μA/μm at $V_{DS} = -0.5$ V, but has no gate modulation, which confirms the metallic nature of the 1T′ MoTe$_2$. The 2H-only device shows a typical MOSFET transfer characteristic with a current on/off ratio of ∼20. The relatively small current on/off ratio can be attributed to the traps at the MoTe$_2$/SiO$_2$ interface. The calculated interface trap density in this device is on the order of 10^{13} cm^{-2}/eV at room

temperature, which significantly degrades the modulation efficiency of the gate electrode. Details of the trap density extraction are provided in Appendix B.5. The room-temperature output characteristics (I_D vs V_{DS}) of the 1T′-only and 2H-only devices are shown in Figure 3.2d. The current of the 1T′-only device is over 4 orders of magnitude larger than that of the 2H-only device at the same V_{DS}. Furthermore, the 1T′-only device has a linear relationship, whereas the 2H-only device displays nonlinear behavior, which is consistent with the metallic (semiconducting) nature of the 1T′ MoTe$_2$ (2H MoTe$_2$) material.
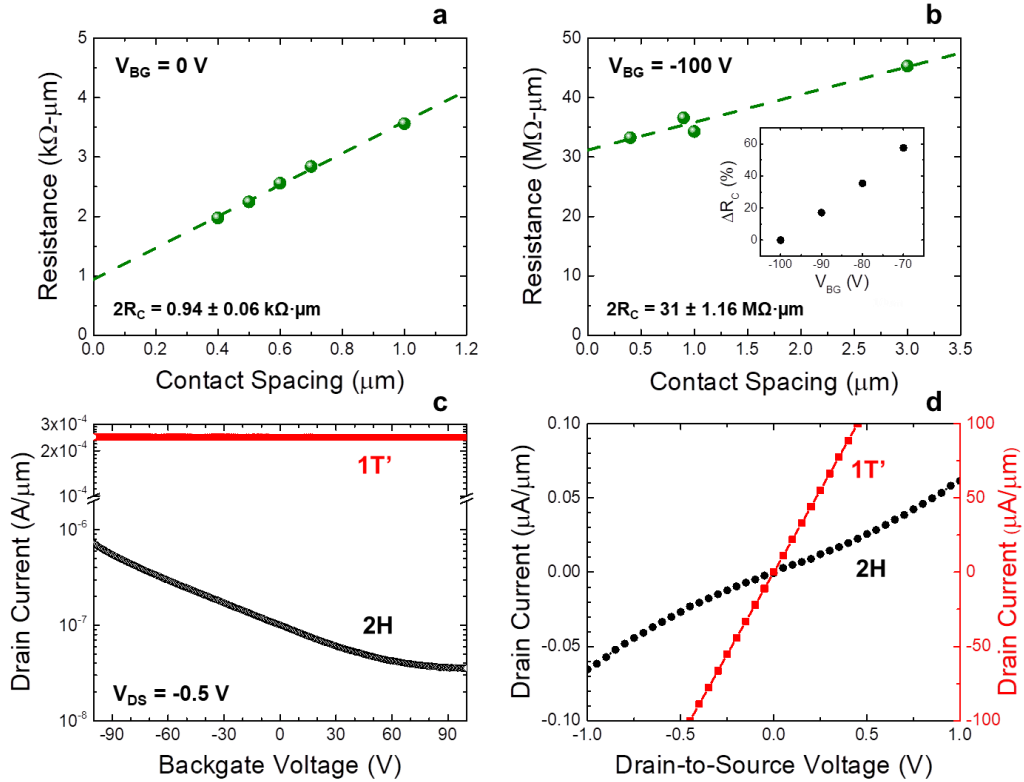
Figure 3.2: Transfer length measurements and device characteristics. (a) Resistance *vs* contact spacing for the 1T′-only device at V_{BG} = 0 V. (b) Resistance *vs* contact spacing for the 2H-only device at V_{BG} = −100 V. Inset is the percentage change of contact resistance at different V_{BG}. (c) Room-temperature transfer characteristics of the 1T′-only and 2H-only devices at V_{DS} = −0.5 V. (d) Room-temperature output characteristics of the 1T′-only device at V_{BG} = 0 V and the 2H device at V_{BG} = −100 V.

3.3 Transport at 2H/1T′ Interface

Figure 3.3 shows the temperature-dependent device behavior for the 2H-only and 2H/1T′ device geometries depicted schematically in Figure 3.3a,b. The I_D vs V_{BG} characteristics of these devices are shown in Figure 3.3c,d, respectively, for temperatures ranging from 77 to 300 K (optical images of these devices are insets in Figure 3.3e,d). As expected, the on-current, current on/off ratio, and subthreshold swing, SS, are improved by using 1T′ electrodes. For the 2H/1T′ device, the current on/off ratio I_{ON}/I_{OFF} increases and SS reduces with decreasing temperature, strongly suggesting that the current of the 2H/1T′ device is in the mobility-limited, as opposed to the thermionic-limited, regime. This improvement of the current on/off ratio is not prominent in the 2H-only device, showing that the current is limited by thermionic transport associated with the metal/2H-MoTe$_2$ interface. Table 3.1 provides a performance comparison of the 2H-only and 2H/1T′ devices.

Table 3.1. Comparison of 2H-only and 2H/1T′ device performance

Property	2H-only devices	2H/1T′ devices	Ratio
On-current (nA/µm) (at 300 K, V_{BG} = -100 V, V_{DS} = -0.1 V)	5.72	39.6	6.9
Transconductance (nS/µm) (at 300 K, V_{DS} = -0.1 V)	0.2	0.43	2.1
Field-effect hole mobility (cm^{2}V^{-1}s^{-1}) (at 300 K, V_{DS} = -0.1 V)	0.6-0.8	7-8	9-13
Current on/off ratio (at 77 K, V_{DS} = -0.1 V)	10	3.5×10^3	350
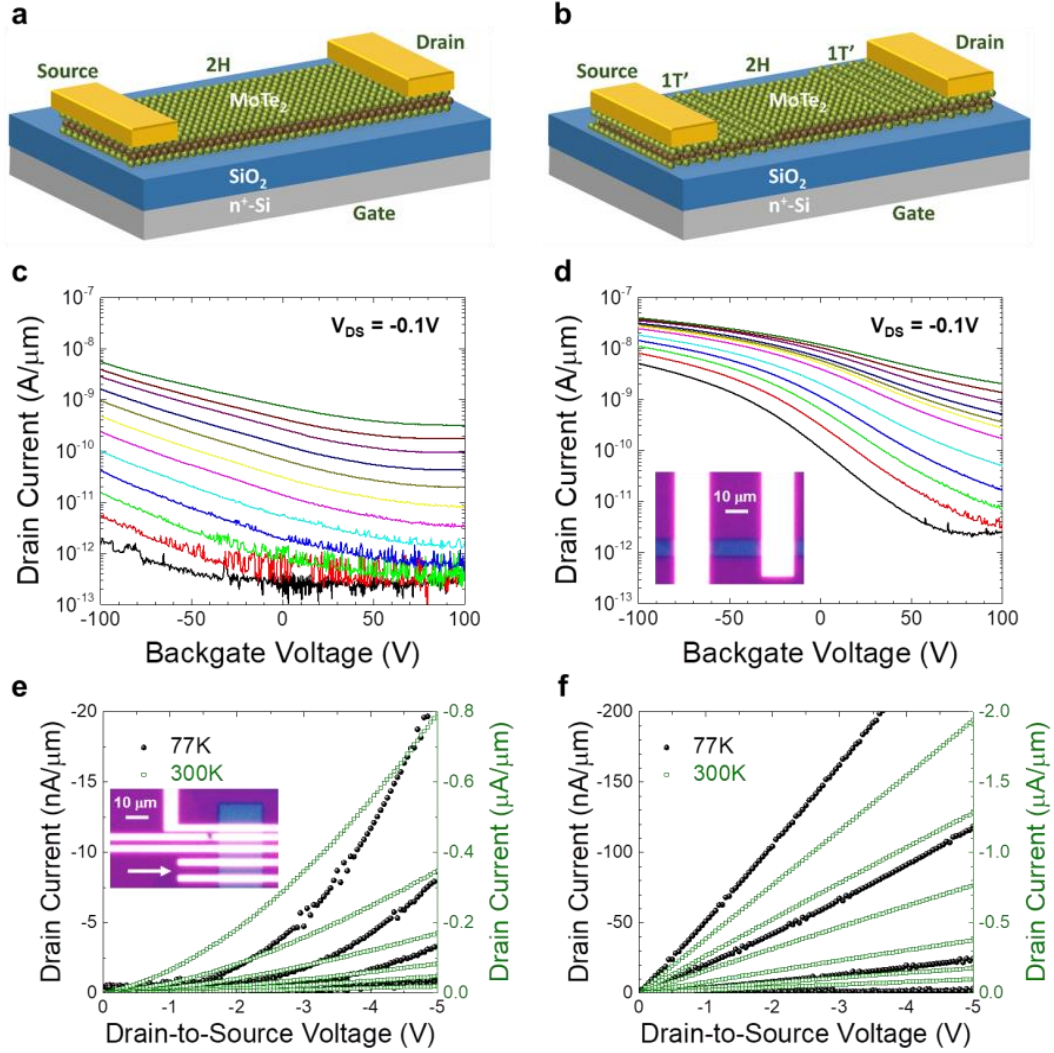
Figure 3.3: Temperature-dependent transport characteristics of the 2H-only and 2H/1T′ devices. (a, b) Schematic diagram of (a) 2H-only and (b) 2H/1T′ device structures. The dimensions of the 2H-only device are $L_{DS} = 3$ μm and $W = 21$ μm, while the 2H/1T′ device has $L_{DS} = 23$ μm and $W = 9$ μm (the length of the 2H region is about 18 μm). (c, d) Transfer characteristics ($I_D vs V_{BG}$) of (c) 2H-only device and (d) 2H/1T′ device at $V_{DS} = -0.1$ V for temperatures of 77 K (black curve) and from 100 K (red curve) to 300 K (olive curve), in steps of 20 K. (e, f) Output characteristics ($I_D vs V_{DS}$) of 2H-only and 2H/1T′ device for V_{BG} varying from -100 V (top curve) to $+100$ V (bottom curve) in steps of $+40$ V at $T = 77$K (black points) and $T = 300$ K (olive points). The optical images of the 2H-only and the 2H/1T′ devices are inset in (e) and (d), respectively, where the specific device is indicated by the arrow.

Once again, the relatively low on-current in our devices is consistent with the

presence of interface traps, which can occur despite the high crystal quality of the 2H-

MoTe$_2$ itself. The field-effect hole mobility of the 2H/1T′ device (7.4 cm^2/(V s)) is ∼10 times higher than that of the 2H-only device (0.8 cm^2/(V s)) and shows a dependence on temperature with a power factor of 1.5, confirming the ohmic contact at the metal/1T′ interface. Accounting for the effect of interface traps in our samples, these mobility values are comparable with previously reported values for CVD-grown MoTe$_2$ [205, 208, 212]. Additional details of the field-effect hole mobility extraction and its temperature dependency are provided in Appendix B.6.

The improvement in the contact resistance using the metal/1T′ electrode design is also observed in the output characteristics (I_D vs V_{DS}) of the devices as shown in Figure 3.3e,f. The linear output characteristics of the 2H/1T′ device at 300 and 77 K indicate ohmic-like behavior of the 1T′ electrode and the 2H/1T′ interface, whereas the output characteristics of the 2H device are nonlinear and this nonlinearity becomes severe at lower temperatures, implying the presence of a Schottky barrier at the metal/2H interface. Furthermore, the on-state drain current values (at $V_{BG} = -100$ V) in the 2H/1T′ device increase with decreasing temperature, whereas the drive current decreases in the 2H-only device with decreasing temperature, suggesting mobility-limited transport in the 2H/1T′ device and thermionic-limited transport in the 2H-only device. The temperature-dependent transport characteristics (Figure B.6) of another set of 2H-only and 2H/1T′ devices show nearly identical trends, suggesting the generality of the observed results. Histograms (Figure B.7) of normalized ON-state resistances for three types of devices fabricated on films from four different growths with slightly different thicknesses (99 devices in total, listed in Table B.2) further confirm the reproducibility of the observed trends.

3.4 Schottky Barrier at Metal/2H and 2H/1T′ Interfaces

Results of the temperature-dependent transfer characteristics were used to extract the SBHs, Φ_{SB}, for the three interfaces: (1) metal/2H phase, (2) metal/1T′, and (3) 2H/1T′. The thermionic emission equation (Equation 1.4 in Chapter 1.4.2) was utilized to model the temperature and bias dependence of the drain current and then the SBHs were extracted from the Arrhenius plots. More on the extraction method is discussed in Chapter 1.4.2.

The Arrhenius plots for a 1T′-only device at $V_{BG} = 0$ V for temperature ranging from 160 K to 260 K are shown in Figure 3.4a. The slopes of the Arrhenius plots are found to be positive, which indicates negative activation energy. Negative activation energy suggests that the conductivity of the 1T′ MoTe$_2$ decreases with increasing temperature, which implies that the 1T′ MoTe$_2$ has metallic-like conductivity. Figure 3.4b shows the Arrhenius plots for a 2H-only device at $V_{BG} = 0$ V for temperatures ranging from 220 K to 300 K. Here, a negative slope was found, indicating activated transport, and similar behavior was found for all values of V_{BG} measured in this study for the 2H-only device. Finally, Figure 3.4c shows the Arrhenius plot for the 2H/1T′ device at $V_{BG} = 0$ V for temperatures between 240 K and 300 K. Once again, a negative slope is observed, indicating thermally activated transport, though the slope is lower than that of the 2H-only device, indicating a lower energy barrier. However, as described above, since no thermally-activated transport was observed for the metal/1T′ interface, we conclude that the energy barrier associated with transport in the 2H/1T′ device is associated with the 2H/1T′ interface and not the metal/1T′ interface.
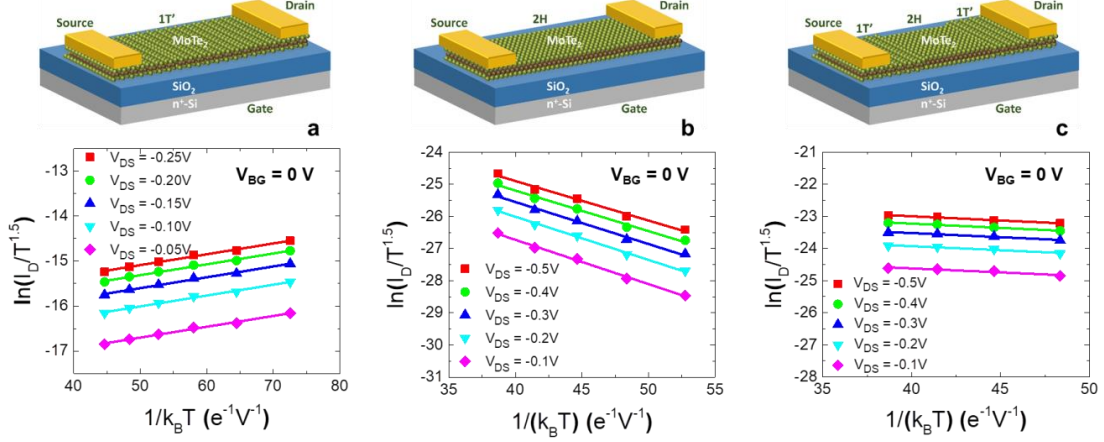
Figure 3.4: Arrhenius plots and bias-dependent effective barrier heights in the high-temperature regime. (a) Arrhenius plots of $\ln(I_D/T^{1.5})$ vs $1/k_B T$ for the 1T′-only device (depicted at the top) at $V_{BG} = 0$ for different values of V_{DS}. The positive slopes indicate the absence of an energy barrier at the metal/1T′ interface. (b) Arrhenius plots for the 2H-only device at $V_{BG} = 0$ V for different values of V_{DS}. (c) Arrhenius plots for the 2H/1T′ device at $V_{BG} = 0$ V for different values of V_{DS}. Given the absence of a barrier at the metal/1T′ interface, the slope is an indication of the barrier height at the 2H/1T′ interface

We performed analysis of the activation behavior of the carrier transport by investigating the dependence upon the backgate voltage, V_{BG}, at a fixed V_{DS}. The results are shown in Figures 3.5a and 3.5b for the 2H-only and 2H/1T′ devices, respectively, where the Arrhenius plots are shown for five different values of V_{BG}. For the 2H-only device, thermally activated transport was observed for all values of V_{BG}, as indicated by the negative slope, where the slope was found to increase with more positive V_{BG}, with only slight deviation of the slope at lower temperatures. However, the 2H/1T′ devices display very different behavior, with two distinct activation energies regimes, one at high temperature and another at low temperatures. First, in the high temperature regime (between 240 K and 300 K) we observe a positive slope at the most negative values of V_{BG}, indicating more metallic-like transport in the strong accumulation region. As V_{BG} increased, the slope was found to change signs and then sharply steepen as V_{BG} was made

more positive. In the low temperature regime (between 100 K and 160 K), a negative slope is observed under all conditions, which only changes slightly as V_{BG} is changed.

In order to determine the complete dependence of Φ_{SB} on V_{BG} for both devices, the effect of V_{DS} on the activation energy must be taken into account. To do this, the slopes from the Arrhenius curves at a particular value of V_{BG} can be plotted *vs.* V_{DS} and then extrapolated to $V_{DS} = 0$. An example of this extrapolation is shown in Figure B.8. This procedure was followed for all devices in order to determine Φ_{SB} as a function of V_{BG}. The results are shown in Figure 3.5c for both the 2H-only device in the high-temperature regime (red squares) and the 2H/1T′ device in the high- and low-temperature regimes (close and open blue circles, respectively). Similar results are observed in other devices from the same substrate, as shown in Figure B.9.

Several interesting trends are observable from Figure 3.5c. First, the overall barrier height for the 2H/1T′ device in the high-temperature regime is dramatically lower than that of the 2H-only device over all V_{BG} values. Given that no thermally-activated barrier exists at the metal/1T′ interface, this result indicates that the 2H/1T′ valence band energy barrier is smaller than the metal/2H energy barrier, in the case of Ti as the Schottky metal. The effective barrier heights at zero backgate voltage for several 2H-only or 2H/1T′ devices with different channel thicknesses have a high level of agreement (Figure B.10). The flat-band barrier height at the 2H/1T′ interface is estimated to be roughly 30 ± 10 meV as illustrated in Figure B.11. The metal/2H barrier is qualitatively consistent with the effective Schottky barrier heights extracted for metal contacts to exfoliated 2H-MoTe$_2$ [213-215], and the 2H/1T′ energy barrier is also consistent with

74

that observed for exfoliated $MoTe_2$ with process-induced 1T′ regions [174], and NaCl-phase-stabilized direct epitaxy [208].
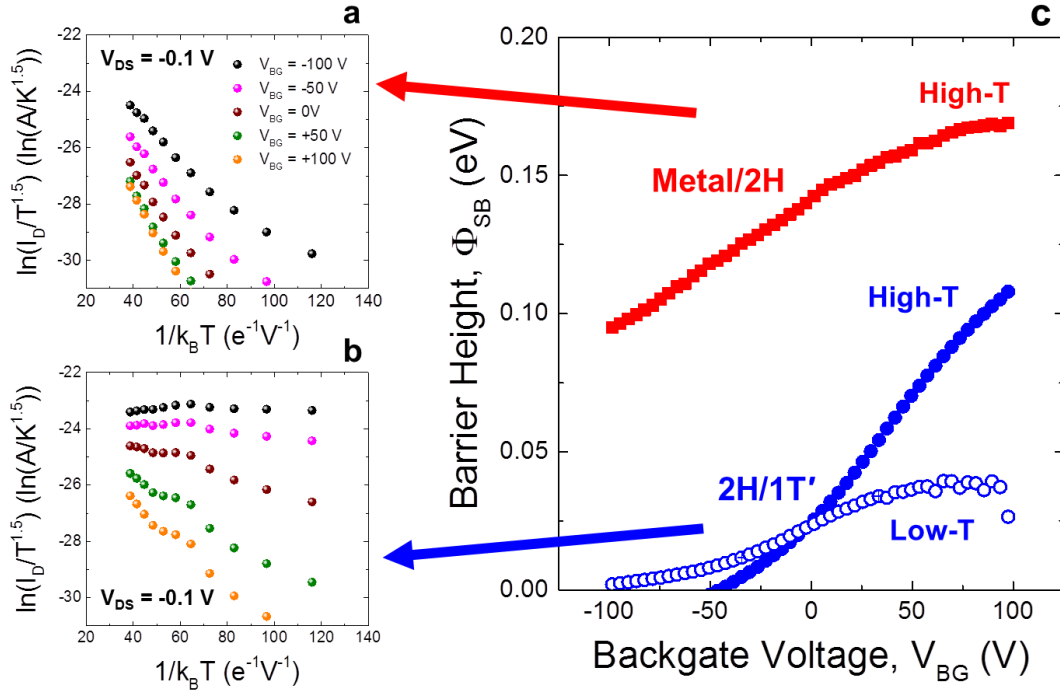
Figure 3.5: Backgate voltage-dependent Arrhenius plots and effective Schottky barrier heights. (a, b) Arrhenius plots for the (a) 2H-only device and (b) 2H/1T′ device at V_{DS} = −0.1 V for V_{BG} ranging from −100 to 100 V. (c) Effective Schottky barrier height of the 2H-only device in the high-temperature regime (red squares) and 2H/1T′ device in the high- (close blue circles) and low- (open blue circles) temperature regimes as a function of V_{BG}.

A second feature we observe is that the gate voltage dependence of the SBH (in the high-temperature regime) is much weaker for the 2H-only device compared to the 2H/1T′ device. We believe the relatively soft SBH dependence *vs*. gate voltage for the 2H-only device is due to a combination of two factors. The first is the presence of interface traps at the $MoTe_2/SiO_2$ boundary that results from the CVD growth procedure. Second, it is well-known that direct metal contacts to 2D semiconductors can have a

relatively long transfer length, where the majority of current is injected underneath the contacts, as opposed to at the contact edge [112, 178, 216, 217] (discussed in Chapter 1.4). In our devices, this is confirmed by our data in Figure 3.2b, which shows a transfer length of several microns. In this situation, the termination of the gate-voltage induced electric field on the metal contacts further reduces the efficiency of the gate modulation. It is the combination of these two effects that leads to very little barrier height modulation. Comparison of band diagrams at the metal/2H and 2H/1T′ interfaces under different backgate voltages illustrates the effect of the longer transfer length in the 2H-only device (Figure B.12), in agreement with previous reports [208]. It should be noted that, in the literature, the effective barrier height for metal contacts to exfoliated 2H-MoTe$_2$ has been found to have strong gate voltage dependence, with the barrier height increasing to 300 meV near the transistor off-state to near zero in the strong on-state region [214]. However, in those devices larger gate modulation is still possible, since it is expected that the interface state density is much smaller than in CVD-grown MoTe$_2$.

In contrast to the 2H-only case, we observed a much stronger modulation of the effective SBH for the 2H/1T′ device in the high-temperature regime. While we expect the interface state density to be similar for the two cases, the 2H/1T′ injector is a pure edge contact, and so the barrier height modulation is not affected by the metal contacts. Therefore, only the interface states associated with the 2H-MoTe$_2$ play a role in degrading the barrier height modulation.

Finally, we note that the SBH for the low-temperature regime of the 2H/1T′ device (also shown in Figure 3.5c) is relatively independent of gate voltage, particularly at positive gate voltages, when the device is nearer to the OFF-state. We believe that this

energy is related to interface traps at the $MoTe_2/SiO_2$ boundary and is not associated with a SBH. In the 2H/1T′ devices, the observation of this low-temperature activation energy regime is made possible by the low 2H/1T′ barrier, which allows sufficient current flow at low temperature. This regime is less easily observable in the 2H-only sample, since at low temperatures, the conductivity is near the noise floor of our measurements.

We also performed DFT of 1T′ and 2H-$MoTe_2$ band structures to estimate the expected band line ups. Details of the DFT calculations are provided in Appendix B.1. The DFT calculations confirm the metallic and semiconducting nature of the 1T′ and 2H phases, respectively (illustrated in Chapter 1.2), and show that the Fermi level at the 2H/1T′ boundary is within ~ 77 meV of the valence band edge (VBE). The calculated SBH is much lower than previous calculations for Ti contacts to 2H-$MoTe_2$ [108], which is qualitatively consistent with our observations in Figure 3.6c. However, we believe that the effect of interface state charging in our samples, as well as the use of a slightly thicker experimental sample than our calculations, makes a truly quantitative comparison with experiment difficult. Nevertheless, the qualitative agreement of our SBH with backgate voltage provides strong evidence as to the high-quality nature of the 2H/1T′ lateral interface in $MoTe_2$.

3.5 Summary

A comprehensive study on the electrical properties of *in-situ*-grown lateral 2H/1T′ $MoTe_2$ homojunction films synthesized by flux-controlled phase engineering has been conducted. $MoTe_2$ p-MOSFETs with metal contacts to 1T′ regions show significant improvement in device performance compared to the ones with metal/2H contacts

because of the reduced contact resistance (< 0.5 kΩ·µm) and the small barrier height (10's meV) for holes at the 2H/1T′ interface. Further reduction of interface traps should lead to improved device performance as well as improved understanding of the transport across the 2H/1T′ interface. While in this work, the technique of growing the 1T′ and 2H phases simultaneously is useful for evaluating the barrier heights and interface quality for homojunctions grown using the flux-controlled method, this technique can also be used to grow the two phases sequentially, which could be more practical for FET applications. In such a technique, the channel 2H phase MoTe$_2$ would be first grown over the entire substrate and patterned into individual channels, followed by the growth of the 1T′ phase around the channels, which could be further patterned and deposited with metal contacts. More on the study of the properties at the *sequentially*-grown 2H/1T′ MoTe$_2$ interface is discussed in Chapter 4. Finally, MoTe$_2$ with 2H/1T′ built-in homojunctions could also have significant benefits for realizing phase-change memory and logic devices, and recent work has shown that electrostatically induced phase change is possible through electrostatic gating.

CHAPTER 4　SEQUENTIAL SYNTHESIS OF LATERAL TMDC JUNCTIONS

The *in-situ*-grown 2H/1T′ MoTe$_2$ homojunctions synthesized by the flux-controlled phase engineering method have shown to form good 2D edge contacts for achieving low contact resistance. However, the *in-situ*-grown synthesis method is not practical for large-scale FET fabrications due to the lack of controllability in size and location of the round 2H-MoTe$_2$ domains. To overcome this issue, this method was previously studied to create patterned 2H/1T′ MoTe$_2$ homojunctions in a two-step lithographic sequence where the 1T′ phase is first synthesized and patterned, followed by the synthesis of 2H phase [37]. However, electrical characterization of the interface properties has not been performed. Furthermore, it would be useful to extend this two-step lithographic synthesis to create various TMDC junctions to fully utilize their diverse properties for novel applications, such as TMDC-based complementary MOSFETs. For example, complementary MOSFETs can be obtained by combining semiconducting TMDCs with metallic TMDCs that result in low contact resistance for either electrons or holes. There are several challenges that need to be addressed. (1) Can the first-grown material preserve its structure without phase transition or decomposition during the synthesis of the second material? (2) How do the interface properties of the *sequentially*-grown interfaces compare to those of the *in-situ*-grown interfaces? Can similar interface quality be achieved? (3) Does metallic materials exist that lead to low contact resistance for both electrons and holes for the same channel material? (4) Can we control the band alignment at the interface by *in situ* substitutional doping of the materials during growth?

This chapter describes this two-step lithographic synthesis approach for the

fabrication of various lateral TMDC junctions. Lateral 2H/1T′ MoTe$_2$ homojunctions and 2H-MoS$_2$/1T′-MoTe$_2$ heterojunctions are fabricated and characterized by Raman mapping, AFM, and transport measurements. TMDC syntheses were performed by Lun Jin. I performed the device fabrication, material and electrical characterizations.

This two-step lithographic synthesis approach can be further utilized in a scaled process for the fabrication of high-performance top-gated TMDC-based MOSFETs with self-aligned, phase-engineered contacts. One of the challenges of implementing this scaled process is the integration of ultra-thin high-κ dielectrics on TMDCs, due to the lack of surface dangling bonds (unsatisfied valences) which act as binding sites for precursor deposition. Preliminary study of the deposition of high-quality HfO$_2$ on MoTe$_2$ by ALD with a monolayer molecular crystal as a seeding layer is discussed.

4.1 *Sequentially*-Grown 2H/1T′ MoTe$_2$ homojunctions

4.1.1 Device Fabrication

Figure 4.1 illustrates the two-step lithographic synthesis approach for creating lateral 2H/1T′ MoTe$_2$ homojunctions based on the flux-controlled phase engineering method. Few-layer semiconducting 2H-MoTe$_2$ is first grown and patterned into rectangular device channels, followed by the growth of few-layer metallic 1T′-MoTe$_2$ as the contact material. The process started with the synthesis of 2H-MoTe$_2$ by tellurization of Mo nanoislands at high Te flux on a Si substrate with 100-nm-thick SiO$_2$ grown on top. Next, channel regions were created by mesa patterning using electron beam lithography (EBL) and etching in an Ar/CHF$_3$/CF$_4$ plasma. A conformal coating of Mo nanoislands was then deposited using electron beam evaporation (EBE) and lift off in acetone. The

deposited Mo nanoislands were then tullerized to 1T′-MoTe$_2$ at low Te flux. Regions composed of two back-to-back 2H/1T′ MoTe$_2$ homojunctions were patterned using EBL and then etched in a 30% H$_2$O$_2$:H$_2$O solution. Finally, Ti/Au metal contacts were deposited on the 1T′-MoTe$_2$ contact regions using EBE. The two-step lithographic approach is compatible with conventional CMOS fabrication process. Details of this two-step process are provided in Appendix C.5.
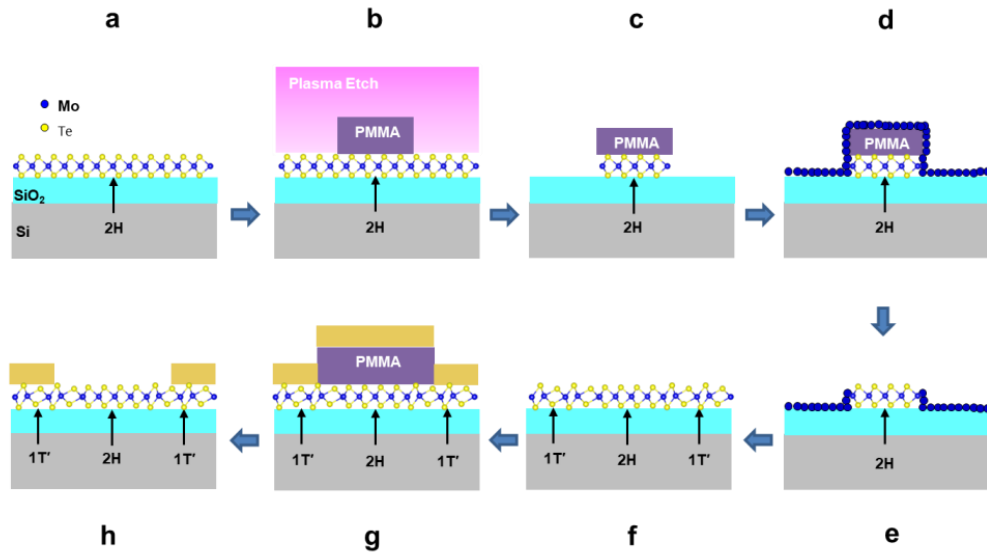
Figure 4.1: Fabrication of lateral 2H/1T′ MoTe$_2$ homojunction FETs using a two-step lithographic synthesis approach. (a) 2H-MoTe$_2$ synthesis. (b-c) Mesa patterning. (d-e) Mo conformal deposition and lift off. (f) 1T′-MoTe$_2$ synthesis. (g-h) Contact patterning and deposition.

The etching process used to pattern device channels caused undercutting of the 2H-MoTe$_2$ channels underneath the PMMA patterns (Figure 4.1c). Therefore, instead of planar deposition, conformal coating was used to ensure physical contacts between the deposited Mo nanoislands and the edges of the 2H-MoTe$_2$ channels. Previous experiments have shown that Mo nanoislands barely migrate during the synthesis of 1T′-MoTe$_2$, as depicted in the SEM images (Figure B.13). Therefore, it is important to make

sure the Mo nanoislands deposited for the synthesis of 1T′-MoTe$_2$ are in direct contact with the edges of the 2H-MoTe$_2$ channels; otherwise, 2H/1T′ homojunctions cannot be formed.

4.1.2   Material Characterizations

An optical image of *sequentially*-grown few-layer 2H/1T′ MoTe$_2$ homojunctions is shown in Figure 4.2a. The rectangular regions are patterned 2H-MoTe$_2$ channels, which are embedded in a 1T′-MoTe$_2$ matrix. Raman spectra (Figure 4.2b) indicate that the materials inside and outside the rectangles are composed of 2H and 1T′ MoTe$_2$, respectively. The phase-specific characteristic Raman peaks are A_{1g} 172 cm^{-1}, E^1_{2g} 232 cm^{-1}, B_{2g} 287 cm^{-1} for few-layer 2H-MoTe$_2$ and A_u 108 cm^{-1}, A_g 127 cm^{-1}, B_g 161 cm^{-1}, A_g 258 cm^{-1} for few-layer 1T′-MoTe$_2$. Raman intensity maps of 2H-MoTe$_2$ E^1_{2g} 232 cm^{-1} peak (Figure 4.2c) and 1T′-MoTe$_2$ B_g 161 cm^{-1} peak (Figure 4.2d) clearly show abrupt junctions between 2H- and 1T′- MoTe$_2$ regions. These results indicate that the phase of 2H-MoTe$_2$ (grown first) is conserved without phase change or decomposition during synthesis of 1T′-MoTe$_2$.

Figure 4.3a shows an optical image of an as-fabricated 2H/1T′ MoTe$_2$ homojunction FET with Ti/Au contacts. It is unclear if the topographic features on the 1T′-MoTe$_2$ surfaces shown in the AFM height image (Figure 4.3b) come from the synthesis and/or fabrication process, and further investigation is needed. The height line profile shows that there are sharp junctions between the 2H- and 1T′- MoTe$_2$ regions, though the 1T′-MoTe$_2$ region is ~18-nm thicker than the 2H-MoTe$_2$ region. This thickness difference (Figure 4.3c) might be due to the variations in the thickness of the

initial Mo nanoislands and the expansion coefficient of unit cell volume from Mo to

$MoTe_2$. Thicker Mo nanoislands were deposited intentionally for the synthesis of 1T′-

$MoTe_2$ to compensate for the recess in the SiO_2 etched during the mesa patterning. The

thickness measurements suggest that the thickness of Mo nanoislands for the synthesis of

1T′-$MoTe_2$ can be reduced. More sophisticated characterization is needed to better

understand the morphology and chemical bonding at the sequentially-grown interface.
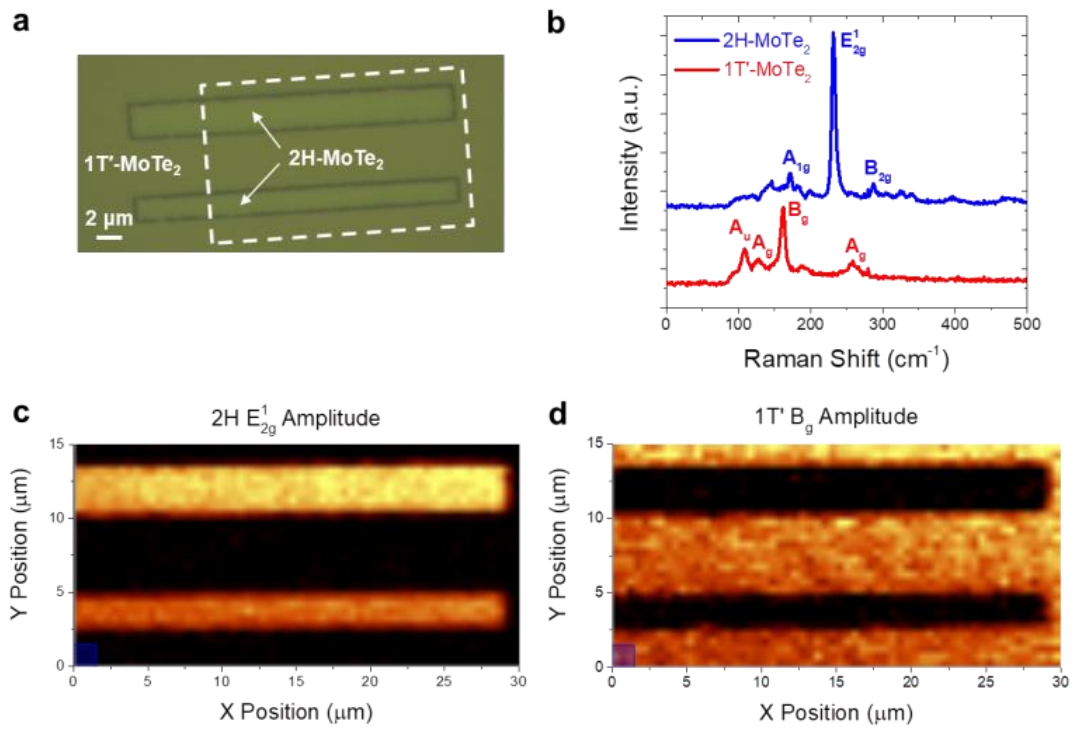
Figure 4.2: Raman mapping of *sequentially*-grown 2H/1T′ $MoTe_2$ homojunctions. (a) Optical image of *sequentially*-grown 2H/1T′ $MoTe_2$ homojunctions on a SiO_2/Si substrate. Two rectangular 2H regions are surrounded by 1T′ matrix. (b) Raman spectra taken from the 2H and 1T′ regions in (a) with an excitation laser with a wavelength of 633 nm and a power of 1 mW. The typical modes are: A_{1g} 172 cm^{-1}, E_{2g}^1 232 cm^{-1}, B_{2g} 287 cm^{-1} for 2H-$MoTe_2$ and A_u 108 cm^{-1}, A_g 127 cm^{-1}, B_g 161 cm^{-1}, A_g 258 cm^{-1} for 1T′-$MoTe_2$. (c)-(d) Raman intensity maps of the E_{2g}^1 mode of the 2H-$MoTe_2$ and the B_g mode of the 1T′-$MoTe_2$ taken from the white dashed rectangle in (a).
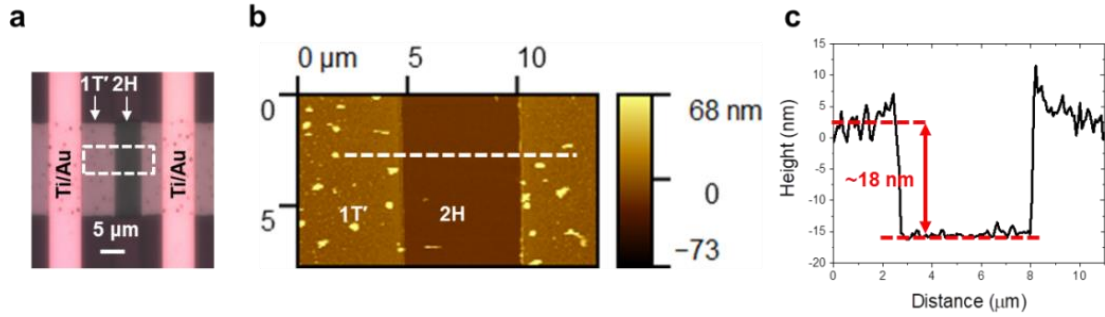
Figure 4.3: AFM of *sequentially*-grown 2H/1T′ MoTe$_2$ homojunctions. (a) Optical image of an as-fabricated 2H/1T′ MoTe$_2$ homojunction FET on a SiO$_2$/Si substrate. The scale bar is 5 um. (b) AFM height map of the region in the white dashed box in (a). (c) The height profile along the horizontal white line in (b) showing that the thickness difference between 2H- and 1T′- MoTe$_2$ is around 18 nm.

4.1.3 Transport Characterizations

Similar to the analysis of the *in-situ*-grown 2H/1T′ MoTe$_2$ homojunctions, three types of FETs were fabricated based on the *sequentially*-grown MoTe$_2$ homojunctions: (1) 1T′-only, (2) 2H-only, and (3) 2H/1T′ homojunction FETs. The room-temperature transfer characteristics of the *sequentially*-grown MoTe$_2$ devices are shown in Figure 4.4a. The 1T′-only devices exhibit a high drive current and no backgate voltage modulation confirming the metallic nature of 1T′-MoTe$_2$. The 2H/1T′ devices perform better than the 2H-only devices confirms a higher electrical conductivity at the sequentially 2H/1T′ interface compared to the metal/2H interface. These substrate-gated *sequentially*-grown MoTe$_2$ FETs show slightly better device characteristics than those of the *in-situ*-grown MoTe$_2$ FETs (Figure 4.4b). Similarly, the performance of the *sequentially*-grown homojunction FETs are also non-ideal as they are fabricated essentially based on the flux-controlled phase-engineering synthesis method, which led to a relatively large interface trap density (due to unreacted Mo and the formation of MoO$_3$ at the MoTe$_2$/SiO$_2$ interfaces).
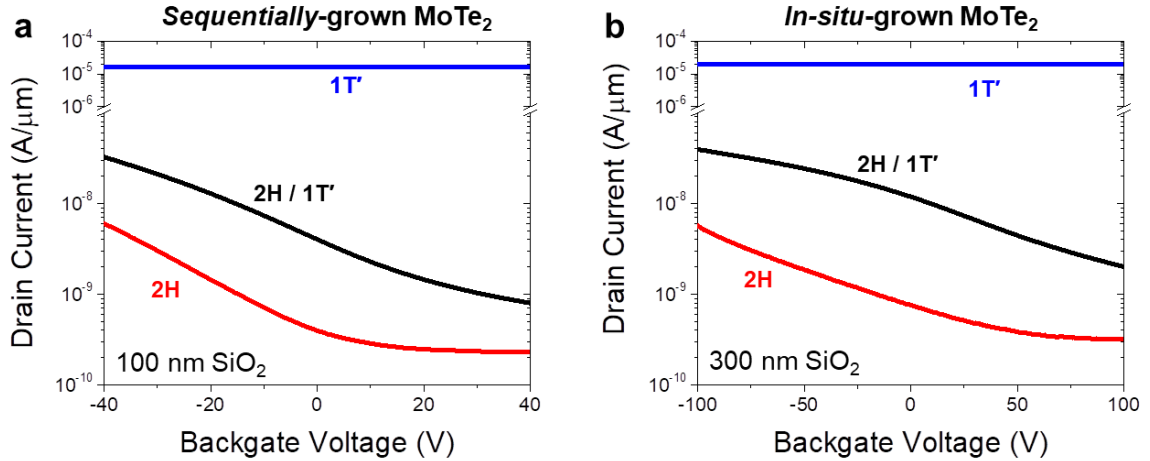
Figure 4.4: Room-temperature transfer characteristics of the 2H-only, 1T′-only and 2H/1T′ homojunction FETs fabricated on (a) *sequentially*-grown and (b) *in-situ*-grown MoTe$_2$ films. All the transfer characteristics were taken at V_{DS} = 0.1 V. For s*equentially*-grown FETs, both the 2H-only and 1T′-only devices have a channel length of 4 um and width of 10 μm. The 2H/1T′ device has a channel length of 4 μm, width of 10 μm, and contact spacing of 10 μm. For the *in-situ*-grown FETs, the 2H-only device has a channel length of 3 μm and width of 21 μm. The 1T′-only device has a channel length of 3 μm and width of 5 μm. The 2H/1T′ device has a channel length of 18 μm, width of 9 μm, and contact spacing of 23 μm.

Temperature-dependent transport characterizations were further performed to investigate the band alignments at the *sequentially*-grown metal (Ti)/2H-MoTe$_2$ and 2H/1T′ MoTe$_2$ interfaces. Figure 4.5 shows the temperature-dependent transport characteristics of a *sequentially*-grown 2H-only and 2H/1T′ homojunction MoTe$_2$ FET. The results show that the current of the 2H/1T′ homojunction device is in the mobility-limited regime whereas the current of the 2H-only device is limited by thermionic transport associated with the metal/2H-MoTe$_2$ interface, similar to the behaviors of the *in-situ*-grown MoTe$_2$ FETs (Figures 3.4c-f). Bias-dependent Schottky barriers at the *sequentially*-grown metal (Ti)/2H-MoTe$_2$ and 2H/1T′ MoTe$_2$ interfaces (Figure 4.6) extracted from the temperature-dependent transfer characteristics (Figures 4.5a-b) are also consistent with those of the *in-situ*-grown interfaces (Figure 3.6c). Temperature-

dependent experimental results confirm that the *sequentially*-grown MoTe$_2$ films and the

in-situ-grown MoTe$_2$ films have comparable electrical properties.
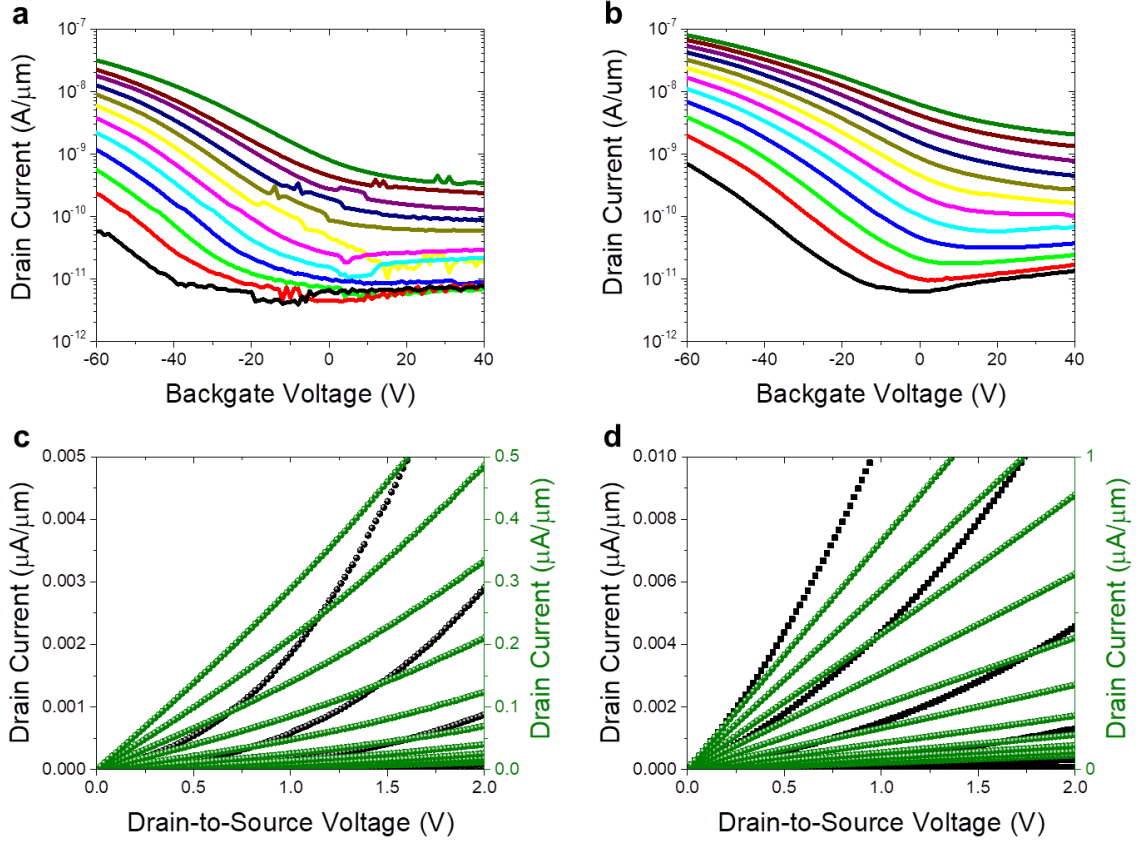
Figure 4.5: Temperature-dependent transport characteristics of the *sequentially*-grown 2H-only and 2H/1T′ homojunction MoTe$_2$ FETs. (a, b) Transfer characteristics (I_D vs V_{BG}) of (a) 2H-only device and (b) 2H/ 1T′ device at $V_{DS} = -0.1$ V for temperatures of 77 K (black curve) and from 100 K (red curve) to 300 K (olive curve), in steps of 20 K. (c, d) Output characteristics (I_D vs V_{DS}) of (c) 2H-only and (d) 2H/1T′ device for V_{BG} varying from −60 V (top curve) to +40 V (bottom curve) in steps of +10 V at T = 77K (black points) and T = 300 K (olive points). The 2H-only device has a channel length of 2 μm and width of 10 μm. The 2H/1T′ device has a channel length of 3 μm, width of 10 μm, and contact spacing of 8 μm.
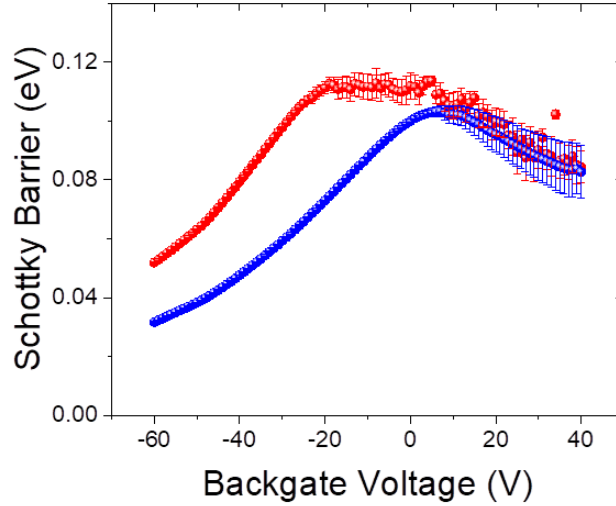
Figure 4.6: Effective Schottky barrier height of the *sequentially*-grown 2H-only device (closed red circles) and 2H/1T′ device (closed blue circles) in the high-temperature regime as a function of V_{BG}.

4.2 *Sequentially*-Grown 2H-MoS$_2$/1T′-MoTe$_2$ Heterojunction

4.2.1 Device Fabrication

The two-step lithographic synthesis approach in Figure 4.1 is slightly modified to fabricate lateral 2H-MoS$_2$/1T′-MoTe$_2$ heterojunctions. 2H-MoS$_2$ flakes were first synthesized by co-evaporation of MoO$_3$ and S using a CVD method (Appendix C.6). The synthesized MoS$_2$ flakes are randomly distributed triangular flakes with large side lengths up to ~80 μm; however, large-area continuous MoS$_2$ films are still preferred in the future. The rest of the process remains the same.

4.2.2 Material Characterizations

Figure 4.7a is an optical image of *sequentially*-grown lateral 2H-MoS$_2$/1T′-MoTe$_2$ heterojunctions on a 100 nm SiO$_2$/Si substrate. The patterned rectangular channel

regions are partially covered with 2H-MoS$_2$. Anywhere outside the rectangular regions is covered with 1T′-MoTe$_2$. The triangular footprint of the original 2H-MoS$_2$ is still visible due to the micro masking effect in plasma etch. Raman spectra taken from 2H-MoS$_2$ and 1T′-MoTe$_2$ regions (Figure 4.7b) show the typical Raman modes E_{2g}^1 381 cm^{-1}, A_{1g} 403 cm^{-1} for 2H-MoS$_2$ and A_u 108 cm^{-1}, A_g 127 cm^{-1}, B_g 161 cm^{-1}, A_g 258 cm^{-1} for 1T′-MoTe$_2$, respectively. Raman maps of 2H-MoS$_2$ E_{2g}^1 381 cm^{-1} peak (Figure 4.7c) and 1T′-MoTe$_2$ B_g 161 cm^{-1} peak (Figure 4.7d) clearly show abrupt junctions between 2H-MoS$_2$ and 1T′-MoTe$_2$ regions. No 2H-MoS$_2$ Raman signals were detected outside the patterned rectangular regions. The fact that the 2H-MoS$_2$ survived during the synthesis of 1T′-MoTe$_2$ suggests that this two-step lithographic synthesis approach has the potential to create various TMDC heterojunctions as long as the first grown TMDC can preserve its phase or crystal structure during the synthesis of the second TMDC. Again, the structural properties of the *sequentially*-grown interfaces need to be further characterized using more sophisticated techniques.

AFM analysis of the *sequentially*-grown 2H-MoS$_2$/1T′-MoTe$_2$ heterojunction is shown in Figure 4.8. The region that was studied is shown in Figure 4.8a. The AFM height map (Figure 4.8b) and the height line profile (Figure 4.8c) of the *sequentially*-grown 2H-MoS$_2$/1T′-MoTe$_2$ heterojunctions in Figure 4.8a again confirms the abrupt junctions between the 2H-MoS$_2$ and 1T′-MoTe$_2$ regions. The 1T′-MoTe$_2$ region above the surface of SiO$_2$ has similar thickness (~3.3 nm) to the 2H-MoS$_2$ region but shows a larger surface roughness.
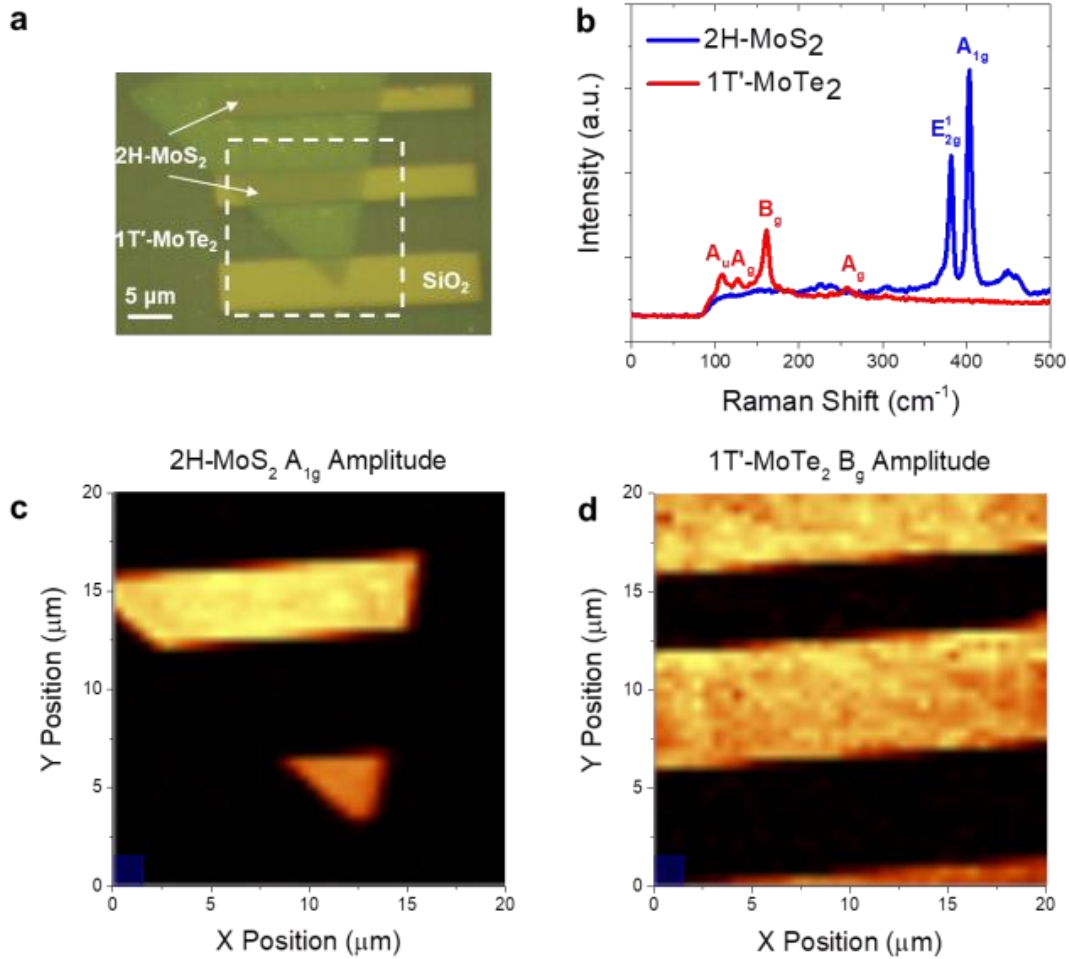
Figure 4.7: Raman mapping of lateral 2H-MoS$_2$/1T′-MoTe$_2$ heterojunctions. (a) Optical image of 2H-MoS$_2$/1T′-MoTe$_2$ heterojunctions on a 100 nm SiO$_2$/Si substrate. The rectangular regions are the patterned channel regions partially covered by 2H-MoS$_2$. Areas outside the patterned channel regions are 1T′-MoTe$_2$. The triangular outline of the original 2H-MoS$_2$ flake is visible due to the micro masking effect in plasma etch. (b) Raman spectra taken from the 2H-MoS$_2$ and 1T′-MoTe$_2$ regions in (a) with an excitation laser with a wavelength of 633 nm and a power of 1 mW. The typical modes are E_{2g}^1 381 cm^{-1}, A_{1g} 403 cm^{-1} for 2H-MoS$_2$ and A_u 108 cm^{-1}, A_g 127 cm^{-1}, B_g 161 cm^{-1}, A_g 258 cm^{-1} for 1T′-MoTe$_2$. (c)-(d) Raman intensity maps of the A_{1g} mode of the 2H-MoS$_2$ and the B_g mode of the 1T′-MoTe$_2$ of the region in the white dashed rectangle in (a).
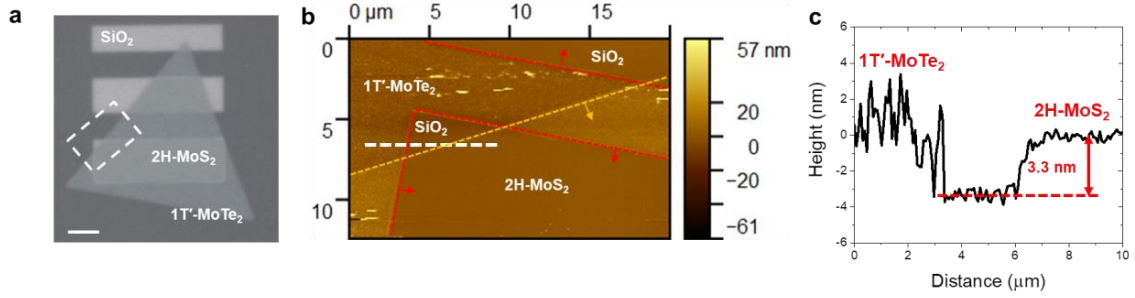
Figure 4.8: AFM of sequentially-grown 2H-MoS$_2$/1T′-MoTe$_2$ heterojunctions. (a) Optical image of 2H-MoS$_2$/1T′-MoTe$_2$ heterojunctions on a SiO$_2$/Si substrate. The rectangular regions are the patterned channel regions partially covered by 2H-MoS$_2$. Areas outside the pattern channel regions are 1T′-MoTe$_2$. The triangular footprint of the original 2H-MoS$_2$ flake is visible due to the micro masking effect in plasma etching. (b) AFM height map of the region in the white dashed box in (a). The red dashed lines are the outlines of the patterned channel regions. The orange dashed line is the outline of the original 2H-MoS$_2$ flake. (c) Height profile along the horizontal white line in (b) showing that both 2H-MoS$_2$ and 1T′-MoTe$_2$ (the part above the surface of SiO$_2$) are ~3.3 nm thick, but 1T′-MoTe$_2$ has a larger surface roughness.

4.2.3   Transport Characterizations

FETs based on *sequentially*-grown 2H-MoS$_2$/1T′-MoTe$_2$ heterojunctions were fabricated on a Si substrate with 100-nm-thick SiO$_2$ which acted as the gate dielectric. Ti/Au (10 nm / 80 nm) were deposited as the contact metals. Figure 4.9a shows the room-temperature transfer characteristics of a heterojunction FET with a channel length of 3 μm and width of 14 μm, and a contact spacing of 11 μm. The channel length is defined as the length of the region between two 1T′-MoTe$_2$ regions. The device is indicated by an arrow in the inset of Figure 4.9a, an optical image of a series of backgated heterojunction FETs. The device exhibits n-type behavior having a ~ 10^5 current I_{ON}/I_{OFF} ratio and a ~0.6 V/dec subthreshold slope. The OFF-state leakage current is extremely low, limited by the noise floor of the measurement setup. However, the ON-state drive current is also low, only in the nA/μm range.
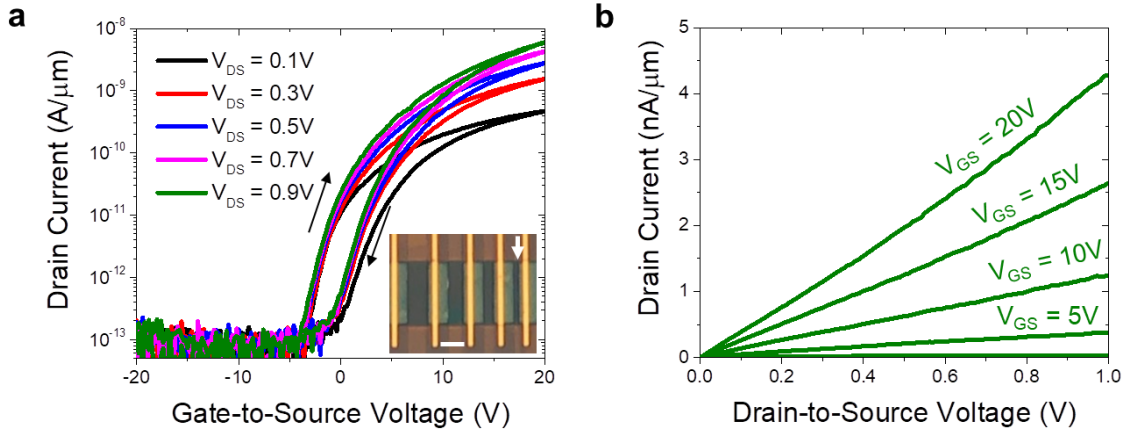
Figure 4.9: Room-temperature transport characteristic of the 2H-MoS$_2$/1T′-MoTe$_2$ heterojunction FETs fabricated using the two-step synthesis approach. (a) Transfer characteristics of a heterojunction FET with a channel length of 3 μm and width of 14 μm, and a contact spacing of 11 μm. The inset is an optical image of a series of backgated heterojunction FETs and the device under test is pointed to by the white arrow. Contact figures are slightly misaligned with the 1T′-MoTe$_2$ regions. The scale bar is 10 μm. (b) Output characteristics of the same device for V_{BG} ranging from -20 V to 20 V with a 5 V step.

In a control experiment, Ti/Au metal contacts were directly made to the 2H-MoS$_2$ flakes to create 2H-only MoS$_2$ n-MOSFETs. The measured room-temperature transport characteristics of a 2H-only MoS$_2$ FET with a channel length of 2 μm and width of 20 μm are shown in Figure 4.10. The device exhibits slightly higher drive current but worse subthreshold slope (~10 V/dec) and current I_{ON}/I_{OFF} ratio (~ 10^4) compared to the 2H-MoS$_2$/1T′-MoTe$_2$ heterojunction FET. Therefore, the intrinsic quality of the CVD-grown MoS$_2$ might be one cause for the low drive current. Other possible causes include the high contact resistance at the metal/1T′-MoTe$_2$ interfaces due to contaminations, as also seen from the unsaturated output characteristics in Figure 4.9b, and the large energy barrier at the 2H-MoS$_2$/1T′-MoTe$_2$ interfaces.
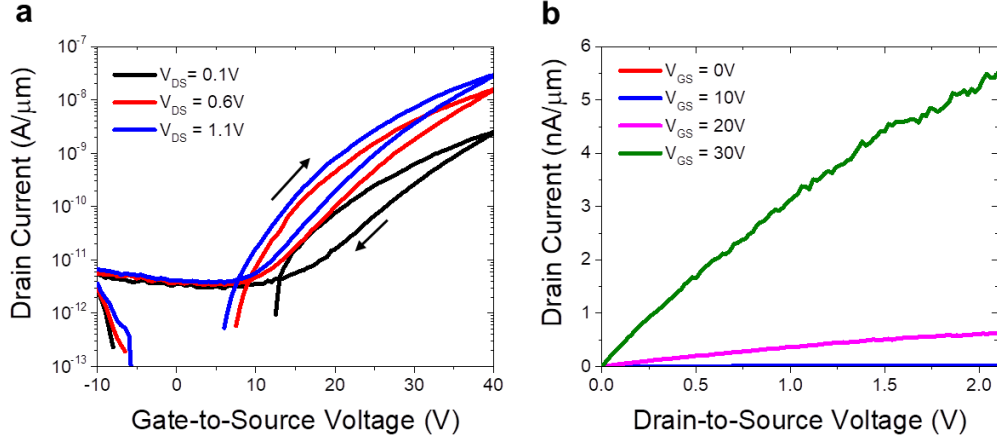
Figure 4.10: Room-temperature transport characteristic of the CVD 2H-MoS$_2$ device with substrate gate (100 nm SiO$_2$/Si). (a) Transfer characteristics of the device with a channel length of 2 μm and width of 20 μm at different V_{DS} values. (b) Output characteristics of the same device at different V_{BG} values.

Temperature-dependent transport characterizations were performed to extract the Schottky barrier at the *sequentially*-grown 2H-MoS$_2$/1T′-MoTe$_2$ interface. Figures 4.11a and 4.11b show the temperature-dependent transfer and output characteristics of a *sequentially*-grown 2H-MoS$_2$/1T′-MoTe$_2$ heterojunction n-MOSFET, respectively. The current I_{ON}/I_{OFF} ratio reduces and the nonlinearity of the output curves increases with decreasing temperature, suggesting that the current is limited by the thermionic transport associated with the 2H-MoS$_2$/1T′-MoTe$_2$ interface. The extracted Schottky barrier (Figure 4.11c) further confirms the large energy barrier at the interface. According to our Schottky barrier extraction for the 2H-MoTe$_2$/1T′-MoTe$_2$ interface, the Fermi level of 1T′-MoTe$_2$ is 10's meV above the valence band of 2H-MoTe$_2$. Therefore, if there are no interface states available, the Fermi level of 1T′-MoTe$_2$ should be aligned near the middle of the band gap of 2H-MoS$_2$ resulting in a large barrier for electron transport (Figure 4.11d). This energy barrier for electrons (holes) can be reduced by combining 2H-MoS$_2$ with other metallic TMDCs which have a Fermi level close to the conduction (valence)

bands of $2H\text{-}MoS_2$.
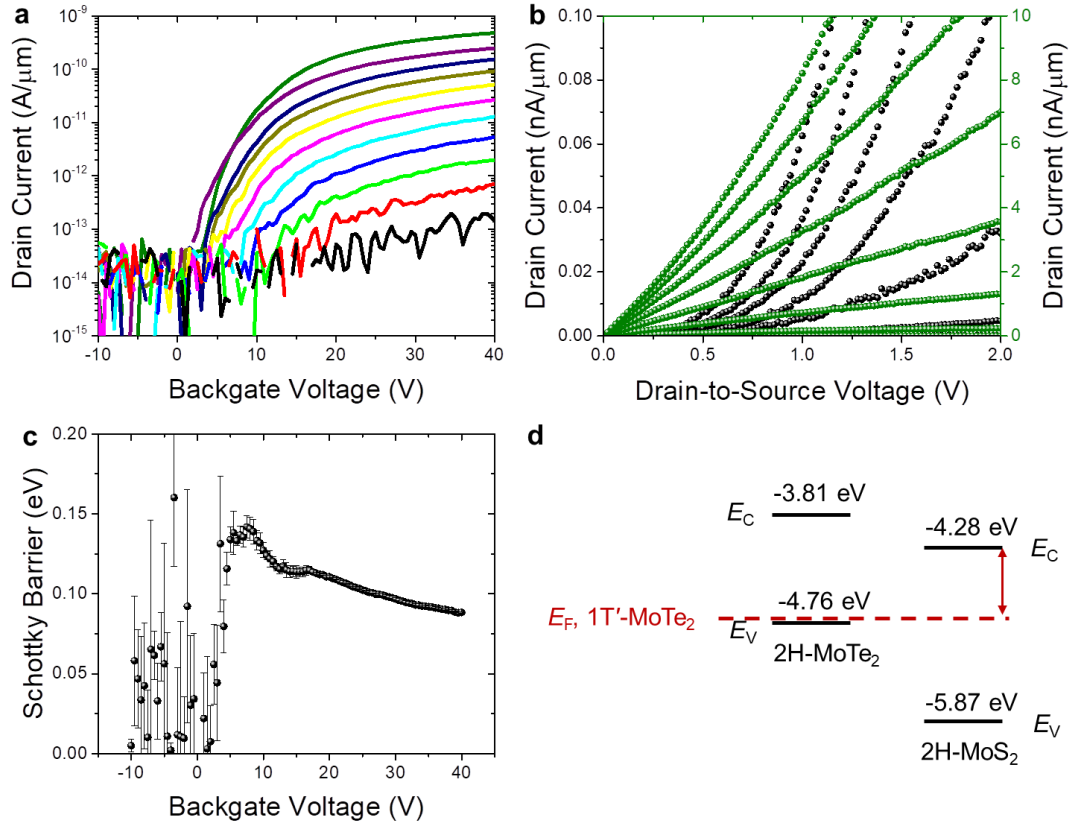
Figure 4.11: Temperature-dependent transport characteristics of a *sequentially*-grown $2H\text{-}MoS_2/1T'\text{-}MoTe_2$ heterojunction n-MOSFET. (a) Transfer characteristics (I_D vs V_{BG}) of the device at $V_{DS} = 0.1$ V for temperatures of 77 K (black curve) and from 100 K (red curve) to 300 K (olive curve), in steps of 20 K. (b) Output characteristics (I_D vs V_{DS}) of the device for V_{BG} varying from -10 V (bottom curve) to $+40$ V (top curve) in steps of $+10$ V at T = 77 K (black points) and T = 300 K (olive points). The device has a channel length of 2 μm, width of 14 μm, and contact spacing of 10 μm. (c) Effective Schottky barrier height of the device in the high-temperature regime as a function of V_{BG}. (d) Illustration of the band alignment for $2H\text{-}MoTe_2/1T'\text{-}MoTe_2$ and $2H\text{-}MoS_2/1T'\text{-}MoTe_2$ interfaces. The Fermi level of $1T'\text{-}MoTe_2$ is based on our experimental Schottky barrier extraction. The calculated band alignment for $2H\text{-}MoS_2$ and $2H\text{-}MoTe_2$ is adapted with permission from the reference [25]. The vacuum level is taken as zero reference.

4.3   Integration of Top Gate Dielectric

The ultimate goal is to utilize this two-step lithographic synthesis approach to develop a scaled process flow for fabricating top-gated TMDC-based MOSFETs with

self-aligned, phase-engineered contacts. Figure 4.12 illustrates this self-aligned process for the fabrication of 2H/1T′ MoTe$_2$ homojunction p-MOSFETs. Again, this process can be extended to create various TMDC heterojunctions for both n- and p-MOSFETs. Such a process could be compatible with standard self-aligned VLSI processing, thus allowing ultimate-scaled devices to be achieved.
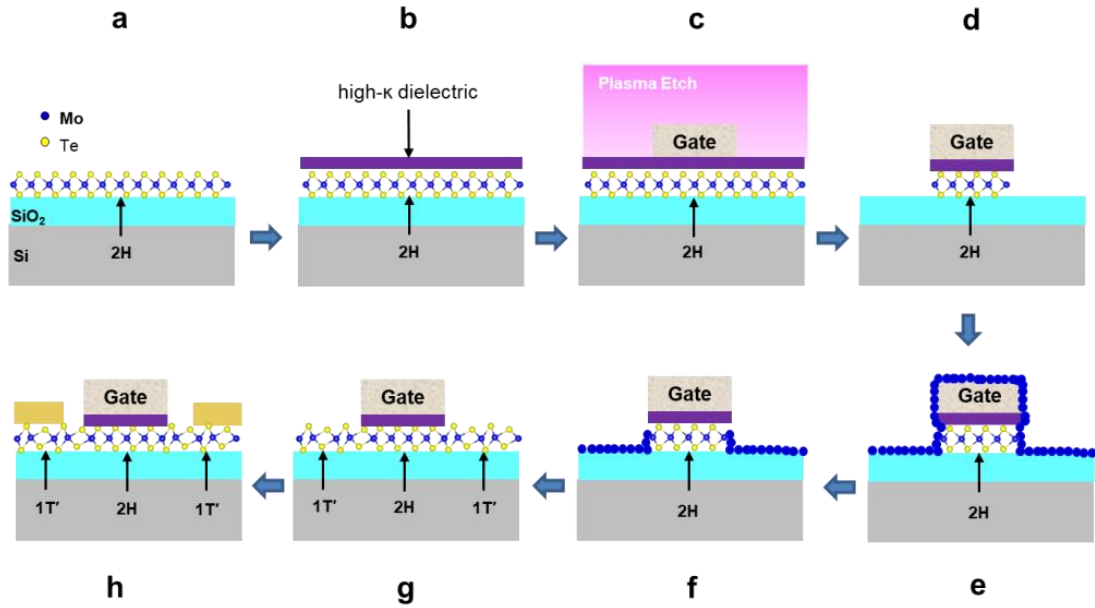
Figure 4.12: Fabrication of lateral 2H/1T′ MoTe$_2$ homojunction p-MOSFETs with self-aligned, phase-engineered contacts. (a) 2H phase MoTe$_2$ synthesis. (b) HfO$_2$ deposition. (c) Gate deposition and lift off. (d) Channel patterning. (e-f) Mo deposition and lift off. (g) 1T′ MoTe$_2$ synthesis. (h) Contact metal deposition and lift off.

This self-aligned fabrication process requires integration of ultra-thin and high-quality high-κ dielectrics on TMDCs. ALD is commonly adapted to deposit ultra-thin high-κ dielectrics owing to its capability in producing conformal and uniform thin films without damage. However, due to the lack of surface dangling bonds (binding sites for precursor deposition) on the basal plane of TMDCs, integration of thin high-κ dielectrics directly on TMDCs using ALD remains challenging. For example, sub-10 nm Al$_2$O$_3$

films directly deposited on MoS_2 using ALD forms island-like clusters with large pinholes (Figure 4.13) [218]. Over the past decade, many techniques have been developed to deposit high-quality high-κ dielectrics on 2D materials, including using interfacial layers, such as oxidized metal layers and hBN [219, 220], and using surface treatment, such as ozone, mild (O_2) plasma, or electron beam irradiation [221, 222, 223]. However, all those methods have their own drawbacks. They could either degrade the quality of 2D materials via surface oxidation or further increase the process complexity. The metal oxidation process suffers from the inherent roughness of evaporated metal films as well as damages by high-energy metal ions [219]. The 2D dielectric, hBN, exhibits high gate leakage currents due to its small band gap (~7 eV), low dielectric constant (5.06), and unfavorable band offsets to most 2D materials [220]. Ozone/O_2/plasma/electron irradiation treatments involve high-energy and reactive species that can introduce defects and interface states [221, 222, 223].
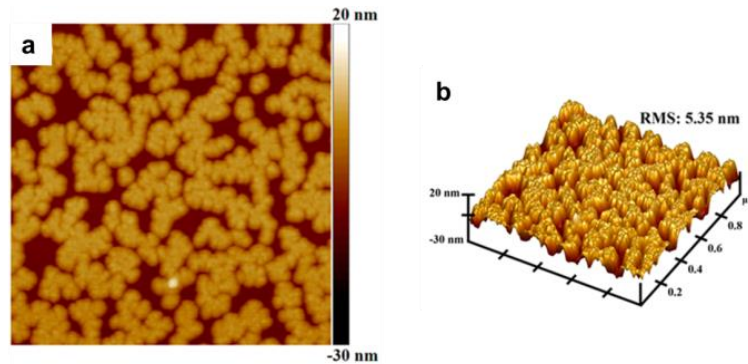
Figure 4.13: AFM images of sub-10 nm Al_2O_3 films deposited on MoS_2 flakes after 120 ALD cycles at 200 °C [218]. (a) Direct growth of the Al_2O_3 films on MoS_2 flakes. (b) The corresponding 3D images of (a). The scan size is 1 μm by 1 μm.

Recently, W. Li et al. reported the robust ALD of highly uniform high-κ dielectric with one-nanometer equivalent oxide thickness on 2D semiconductors by using monolayer (ML) 3,4,9,10-perylene-tetracarboxylic dianhydride (PTCDA) as a seeding

layer [224]. Figure 4.14a illustrates an HfO_2/ML PTCDA/2D material hybrid structure. PTCDA is layered material with ~0.3 nm interlayer distance corresponding to the π -π stack direction. When grown on 2D materials, it self-assembles into a herringbone lattice stabilized by hydrogen bonding [225]. ML PTCDA can be easily deposited on 2D materials using physical vapor deposition (PVD) [226]. The carbonyl functional groups in PTCDA molecules serve as closely distributed sites for ALD nucleation. Using ML PTCDA seeding layer, HfO_2 dielectrics with thickness down to 2 nm deposited on graphene, hBN, and MoS_2 are very smooth, as shown in the bright-field cross-section STEM images (Figure 4.14b). The n-type MoS_2 FET (p-type WSe_2 FET) with 3 nm HfO_2 gate dielectric (EOT = 1.3 nm) exhibit on/off ratio of 10^7 (10^6) and near-Boltzmann-limit SS of 60 (67) mV/dec. These results suggest that ML PTCDA is an excellent seeding layer for depositing ultra-thin high-quality gate dielectrics on 2D materials. This chapter demonstrates our preliminary results when adapting this technique to integrate thin HfO_2 on FETs based on our CVD-grown $MoTe_2$.
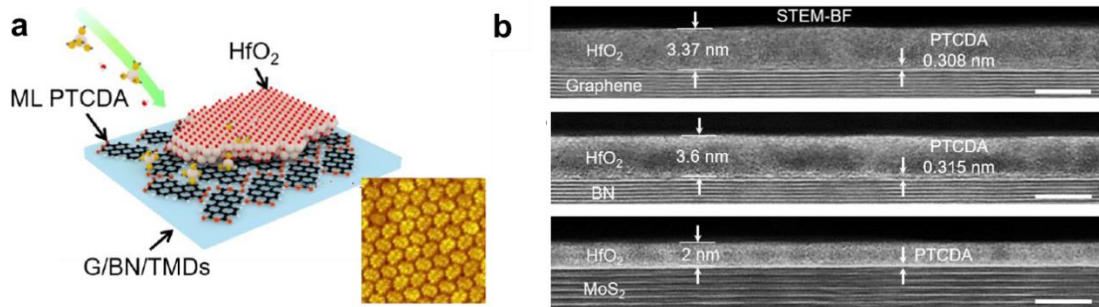
Figure 4.14: ALD of highly uniform high-κ dielectric with one-nanometer equivalent oxide thickness on 2D semiconductors by using ML PTCDA [224]. (a) Schematic illustration of the hybrid ML PTCDA/HfO_2 gate stack on 2D materials. Inset shows a 10 nm×10 nm high-resolution STM scan of ML PTCDA on graphene. (b) Cross-sectional STEM bright-field image of ML PTCDA/HfO_2 on graphene (top), MoS_2 (middle) and h-BN (bottom), respectively. The thickness of HfO_2 and PTCDA layer are marked, respectively. Scale bar are 5 nm.

4.3.1   Deposition of HfO$_2$ on 2H-MoTe$_2$

The top-gate fabrication started by first growing a few-layer 2H-MoTe$_2$ film on a SiO$_2$/Si substrate using the flux-controlled phase engineering method. To compare the deposition of PTCDA on SiO$_2$ and 2H-MoTe$_2$, the film was scratched by tweezers to expose SiO$_2$ in some regions. Next, ML PTCDA was deposited on the substrate using PVD. Details of the PVD method are provided in Appendix C.7. Figure 4.15a shows an optical image of a scratched region after ML PTCDA deposition. Raman spectra (Figure 4.15b) taken from a spot on the 2H-MoTe$_2$/ML PTCDA stack exhibit typical Raman peaks A_{1g} 172 cm^{-1}, E_{2g}^{1} 232 cm^{-1}, B_{2g} 287 cm^{-1} for few-layer 2H-MoTe$_2$ (indicated by red arrows) and Raman peaks A_g 1303 cm^{-1}, A_g 1383 cm^{-1}, A_g 1573 cm^{-1}, A_g 1590 cm^{-1} for ML PTCDA (indicated by blue arrows). Raman intensity maps of 2H-MoTe$_2$ E_{2g}^{1} 232 cm^{-1} peak (Figure 4.15c) and ML PTCDA A_g 1303 cm^{-1} peak (Figure 4.15d) show that ML PTCDA was deposited only on 2H-MoTe$_2$, not on SiO$_2$. It is because ML PTCDA was stabilized on the surface of 2H-MoTe$_2$ by hydrogen bonding and π-π interactions.

Next, ~6nm-thick HfO$_2$ was deposited at 150 °C by ALD using Tetrakis(dimethylamido) hafnium (TDMAH) and H$_2$O as precursors. Details of the HfO$_2$ deposition are provided in Appendix C.8. Figure 4.16 shows the AFM height maps for a 2H-MoTe$_2$ film, a 2H-MoTe$_2$/ML PTCDA stack after ML PTCDA deposition, and a 2H-MoTe$_2$/PTCDA/HfO$_2$ stack after HfO$_2$ deposition. After ML PTCDA deposition, the height was uniformly increased by ~0.3-0.4 nm, consistent with the height of ML PTCDA. The ML PTCDA film was highly crystalline and uniform with RMS similar to that of the 2H-MoTe$_2$ underneath. After HfO$_2$ deposition, no change in the height

indicates that uniform HfO_2 was deposited over the entire substrate. The deposited HfO_2 was pinhole-free with low RMS of ~0.4 nm.
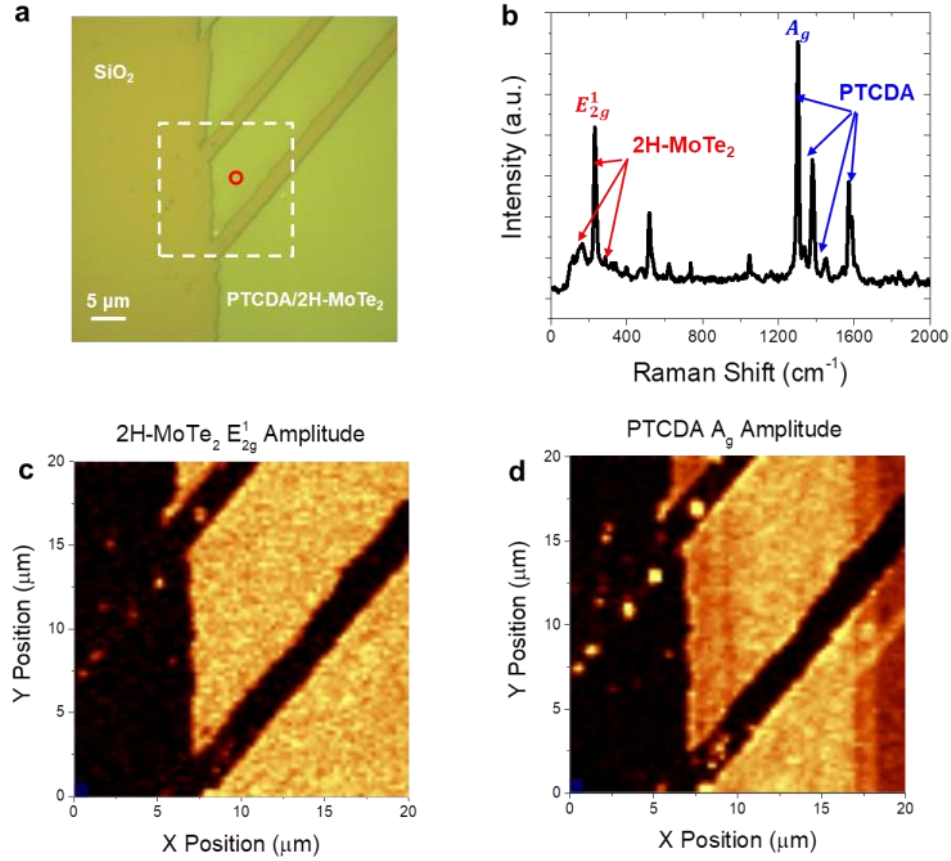
Figure 4.15: Raman mapping of 2H-MoTe$_2$/ML PTCDA stacks on a SiO$_2$/Si substrate. (a) Optical image of 2H-MoTe$_2$ flakes covered with ML PTCDA. (b) Raman spectra taken from the red spot in (a) with an excitation laser with a wavelength of 633 nm and a power of 1 mW. The typical modes are A_{1g} 172 cm^{-1}, E_{2g}^1 232 cm^{-1}, B_{2g} 287 cm^{-1} for few-layer 2H-MoTe$_2$ and A_g 1303 cm^{-1}, A_g 1383 cm^{-1}, A_g 1573 cm^{-1}, A_g 1590 cm^{-1} for ML PTCDA. (c)-(d) Raman intensity maps of the E_{2g}^1 232 cm^{-1} mode of 2H-MoTe$_2$ and the A_g 1303 cm^{-1} mode of PTCDA, respectively. PTCDA peak intensity was only detected on 2H-MoTe$_2$.
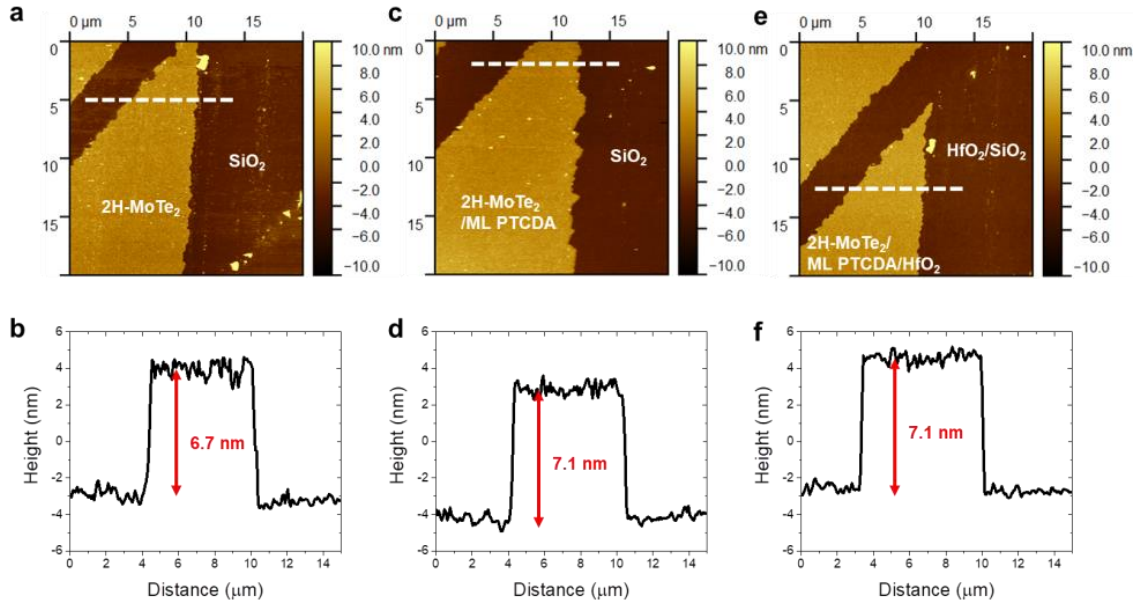
Figure 4.16: AFM height maps and profiles of a 2H-MoTe$_2$ flake on a SiO$_2$/Si substrate at different steps of HfO$_2$ integration. (a)-(b) a 2H-MoTe$_2$ film synthesized using the flux-controlled phase engineering method. The 2H-MoTe$_2$ flake has a thickness of ~6.7 nm and RMS of ~0.57 nm. The SiO$_2$ substrate has a RMS of ~0.22 nm. (c)-(d) The 2H-MoTe$_2$/ML PTCDA stack after monolayer (ML) PTCDA deposition. The 2H-MoTe$_2$/ML PTCDA stack has a thickness of ~7.1 nm and RMS of ~0.53 nm. It suggests that ML PTCDA (~0.3 nm) was deposited on 2H-MoTe$_2$. The RMS of SiO$_2$ is still ~0.22 nm. (e)-(f) The 2H-MoTe$_2$/ML PTCDA/HfO$_2$ stack after ~6 nm HfO$_2$ deposition using ALD. Since HfO$_2$ was deposited everywhere, the step height did not change. The 2H-MoTe$_2$/ML PTCDA/HfO$_2$ stack has RMS of ~0.4 nm and the HfO$_2$/SiO$_2$ stack has RMS of ~0.16 nm.

4.3.2 Dielectric Properties of HfO$_2$

To study the dielectric properties, 2H-MoTe$_2$ p-MOSFETs with ML PTCDA/6 nm HfO$_2$/10 nm Ni/100 nm Au as the top-gate stack were fabricated. 2H-MoTe$_2$ films were synthesized using the flux-controlled phase engineering method. The top-gated devices did not show improved transport characteristics (Figure 4.17) compared to the substrate-gated device, which might be attributed to the poor top interface quality due to surface roughness, contamination from the fabrication process, or oxidation of the topmost 2H-MoTe$_2$ layer. However, the gate leakage (red curve in Figure 4.17a) was less

than 10 pA/μm at top-gate voltages, $V_{TG} = \pm 3V$, close to the breakdown voltage for ~6 nm-thick HfO_2 (~0.6-0.9 V/nm breakdown field [227]), confirming the high quality of the HfO_2 film. Future work includes: (1) verifying the properties of the HfO_2 dielectrics using pristine TMDC materials, such as exfoliated layers, (2) studying the surface morphology of CVD-grown TMDCs using TEM/STEM, and (3) developing techniques to clean the surface of CVD-grown TMDCs before deposition of the PTCDA and HfO_2.
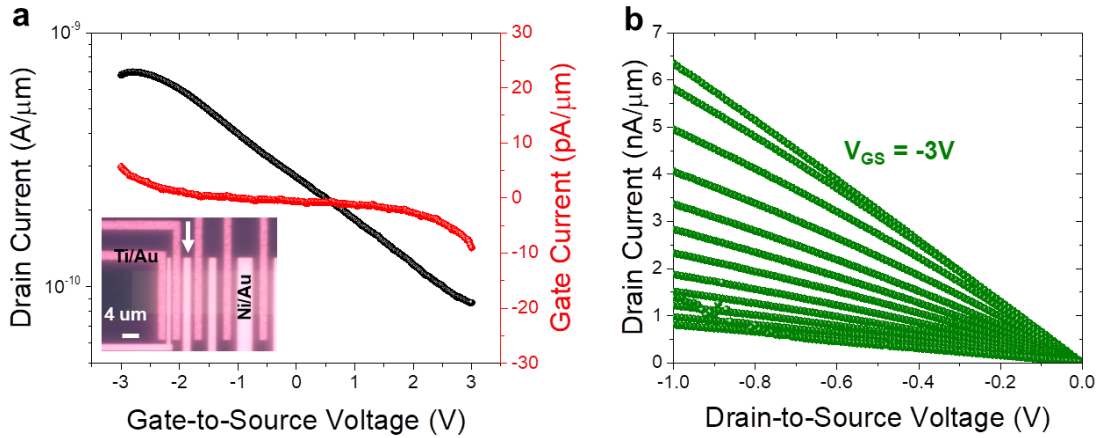
Figure 4.17: Room-temperature transport characteristic of the top-gated 2H-MoTe$_2$ p-MOSFETs. (a) Transfer characteristics of a device with a gate length of 2 μm, channel length of 4 μm and channel width of 22 μm at V_{DS} = -0.1 V. The device is pointed by the white arrow in the inset. The inset is an optical image of a series of 2H-MoTe$_2$ p-MOSFETs with ~6nm-thick HfO_2 dielectric and Ni/Au top gate on a SiO$_2$/Si substrate. The brighter wires are Ni/Au (10 nm/ 100 nm) top gates and the darker wires are Ti/Au (10 nm/ 80 nm) contacts. (b) Output characteristics of the same device for V_{BG} ranging from -3 V to 3 V with a 0.5 V step.

4.4 Summary

A two-step lithographic synthesis approach for fabricating lateral 2H/1T′ MoTe$_2$ homojunctions and 2H-MoS$_2$/1T′-MoTe$_2$ heterojunctions has been demonstrated. The *sequentially*-grown 2H/1T′ MoTe$_2$ homojunction FETs fabricated using this method show p-type behavior similar to that of the *in-situ*-grown MoTe$_2$ homojunction p-MOSFETs. The *sequentially*-grown 2H-MoS$_2$/1T′-MoTe$_2$ heterojunction FETs exhibit n-

type behavior with high current I_{ON}/I_{OFF} ratio, good subthreshold slope and low OFF-state current. However, the ON-state derive current is relatively low. The preliminary results verify that this two-step lithographic synthesis approach has potential to be utilized to create complementary TMDC-based MOSFETs. More structural and electrical characterizations are needed to better understand the properties of the *sequentially*-grown junctions.

The integration of thin high-quality dielectrics on 2H-MoTe$_2$ by ALD using a PTCDA seeding layer has also been investigated. This is one of the essential steps to utilize the two-step lithographic synthesis approach to enable a scaled process flow for the fabrication of high-performance top-gated MOSFETs with self-aligned, phase-engineered contacts. Although Raman and AFM results showed that the deposited HfO$_2$ has good uniformity, unfortunately, the HfO$_2$-gated 2H-MoTe$_2$ p-MOSFETs did not exhibit improved device characteristics compared to the substrate-gated ones, which might be due to the nonideality at the top interface. However, the HfO$_2$ did show low leakage current at high bias voltages indicating good dielectric properties of the HfO$_2$. More experiments are needed to verify the interface quality of the HfO$_2$ deposited on MoTe$_2$ using the ALD method.

CHAPTER 5   PHASE TRANSITION BY GATE-CONTROLLED LITHIUM INTERCALATION

Due to the large reduction in contact resistance, the resistance of the 2H/1T′ MoTe$_2$ homojunction FETs is dominated by the 2H channel properties. Dynamic and reversible control of the channel resistance via the semiconducting 2H to metallic 1T′ transition can make such a structure operate as a phase-change memory (PCM) device. As discussed in Chapter 1.5.1, tuning the phases in multilayer TMDCs requires a large charge doping level, which can be achieved by conventional high-κ dielectrics (such as HfO$_2$) but can be reached by electrostatic doping through ionic liquid gating [194] and chemical doping through lithium intercalation [95]. The ionic liquid gating is a reversible process but it has a small screening length (< 1 nm), meaning that it can only induce phase transition in monolayer TMDCs or the top-most layer of multilayer TMDCs. In contrast, the lithium intercalation can induce higher doping concentration and dope each individual layer in multilayer TMDCs, but it is an irreversible process.

In order to utilize our multilayer MoTe$_2$ homojunction FETs as PCM devices, a reversible gating mechanism that can induce phase transition in each individual layer is required. To realize it, a lithium-ion-based solid electrolyte (Li electrolyte) has been considered because it can electrochemically dope each individual layer through lithium intercalation controlled dynamically by gate voltage (an electrochemical doping mechanism). Generally, the Li electrolyte has several advantages over the liquid polymer electrolytes for studying the phase transition in multilayer TMDCs: (1) Owing to the smaller size of Li$^+$ ions (accumulated closer to the electrodes), it has large capacitance and breakdown voltage enabling high electrostatic doping concentration at low gate

voltages [228]. (2) At high gate voltages, Li^+ intercalation can be induced in-between layered TMDCs far beyond the electrostatic screening length (< 1 nm). Due to the large interlayer spacing of TMDCs, Li^+ ions can be driven in and out of layered TMDCs through a large gate electric field leading to high doping levels in each atomic layer. Y. Yu *et al.* has reported a phase transition in ~13 nm-thick TaS_2 by gate-controlled Li^+ intercalation using a Li electrolyte [229]. (3) Li electrolytes are nearly transparent, allowing simultaneous *in situ* optical and electrical characterizations. (4) The solid nature makes it compatible with conventional CMOS fabrication techniques. Conductive polymer materials can be integrated above the solid electrolyte as gate electrodes using standard photolithographic process.

Figure 5.1a shows a schematic illustration of a PCM device concept based on the monolayer 2H/1T′ $MoTe_2$ homojunction FETs with Li electrolyte gating (Li electrolyte FETs). The resistance state of the device switches from a high-resistance state to a low-resistance state when the channel material is switched from the 2H phase to 1T′ phase, and *vice versa*. The phase transition can be detected both optically and electrically. For optical detection, given that different structural phases exhibit distinct phonon vibration modes, Raman spectroscopy can be used to characterize the phase evolution of the channel when sweeping the gate voltage. For electrical detection, the change in the channel resistance can be read out from the device output characteristic, namely, the drain current vs. drain-to-source voltage (I_D-V_{DS}) curve (Figure 5.1b). The I_D-V_{DS} curve should display a dramatic change when the channel is switched.
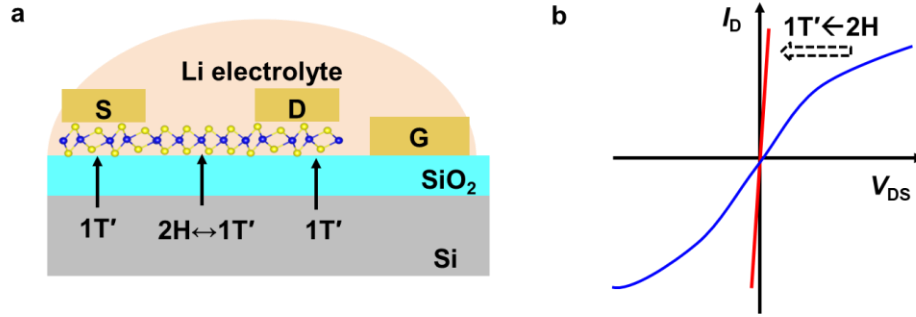
Figure 5.1: (a) Proposed phase-change memory device based on CVD 2H/1T′ MoTe$_2$ homojunction FETs with lithium-ion-based solid electrolyte in a side-gated configuration. It is worth noting that polymer gate electrodes can also be integrated on top of the electrolyte. (b) Expected behavior of the drain current vs. drain-to-source voltage (I_D-V_{DS}) curves resulting from the 2H to 1T′ phase transition.

One of the concerns for such a device is the slow movement of ions which may result in a hysteresis effect and limit the speed of the device. Inspiringly, the molecular dynamics simulations by K. Xu *et al.* (Figure 5.2) showed that the timescale for EDL formation to 10^{13} cm^{-2} can be reduced to nanoseconds in Li electrolyte at sufficiently high field strength (i.e., tens of mV/nm) [230]. Therefore, the Li electrolyte has the potential to be made high-speed if the polymer architecture, ion concentration, and additives in the electrolyte are carefully designed to reach high field strength.

In the following sections, the gate-controlled Li$^+$ intercalation induced phase transition in the CVD-grown 2H/1T′ MoTe$_2$ homojunction, exfoliated monolayer and few-layer MoTe$_2$, exfoliated few-layer MoS$_2$, and pre-lithiated few-layer MoS$_2$ flakes is explored. Devices fabricated on those materials are gated through a Li electrolyte and the phase of those materials is monitored by Raman spectroscopy. A reversible 2H/1T′ phase transition in pre-lithiated few-layer MoS$_2$ flake is observed, which has the potential to be utilized in our proposed PCM device concept.
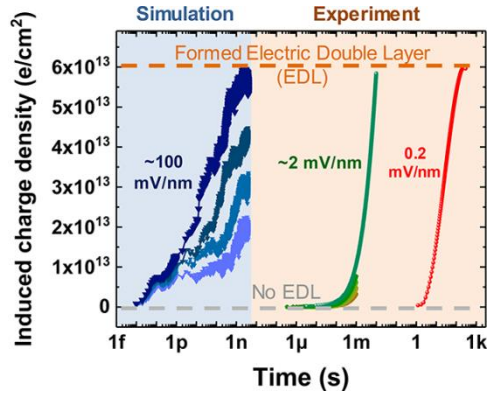
Figure 5.2: Charge density vs time during EDL formation from both simulation (left panel, light blue to dark blue indicate 50−100 mV/nm) and experiment (right panel, yellow to green indicate E_{pulse} from 0.3 to 2.3 mV/nm). The lower dashed line corresponds to no EDL formation, and the top dashed line corresponds to a formed EDL with a charge density of 6×10^{13} cm^{-2}. Reprinted with permission from [230]. Copyright (2018) American Chemical Society.

5.1 Experimental Details

5.1.1 Device Fabrication of Li Electrolyte FETs

Few-layer 2H/1T′ MoTe$_2$ homojunctions were synthesized on a 300 nm SiO$_2$/Si substrate using the *in situ* flux-controlled phase engineering method (described in Chapter 2), followed by lithographic patterning and etching to form 1T′/2H/1T′ channels. Next, the contact and the side-gate electrodes were patterned and deposited with 10 nm Ti/80 nm Au metals using electron beam lithography and deposition. Contact electrodes were deposited on the 1T′ regions and the gate electrode (side-gate) was deposited ~20-50 μm away from the channels, rather than above the channels. Details of the fabrication process are provided in Appendix C.4. A Li electrolyte was prepared by dissolving lithium perchlorate (LiClO$_4$) in polyethylene oxide (PEO) matrix (PEO:LiClO$_4$) with a weight ratio of 1:3.3. Specifically, 0.3 g LiClO$_4$ (Sigma Aldrich) and 1 g PEO powders (Mw = 100,000, Sigma Aldrich) were mixed with 15 ml anhydrous methanol (Alfa Aesar). The mixture was stirred overnight with the temperature kept at 50 °C. The liquid

PEO:LiClO$_4$ solution was drop-casted onto the substrate using a syringe and spread over the channels and electrodes. After application of the electrolyte, the substrate was annealed at 375 K under vacuum for 30 min to eliminate residual methanol and moisture. The substrate was kept under vacuum at all times during this process.

5.1.2　Raman and Electrical Characterization Setups

In order to apply a gate voltage while taking Raman spectra, the substrate was mounted on a customized holder which can connect the electrodes of the devices on the substrate to external power sources. The side-gate voltage, V_{SG}, was applied between the side-gate electrode and the source electrode of the Li electrolyte FETs using a Keithley 2450 source meter. A schematic of the Li electrolyte FETs with electrical connections is shown in Figure 5.3. Raman spectra were taken in air at various side-gate voltages with 532 nm laser excitation with a Witec confocal spectrometer using a 100× long working distance objective. Laser power was kept below 1 mW to eliminate the chance of inducing sample damages or the 1T′ phase by laser irradiation. To reduce the hysteresis resulting from the slow movement of molecules in the electrolyte, Raman spectra at each side-gate voltage were recorded 2 min after the voltage was set to a new value. For electrical measurement, the substrate was loaded in a vacuum probe station. The output characteristics (I_D-V_{DS}) were taken using a semiconductor analyzer (Keysight B1500A) under different V_{SG} values. It is worth noting that this electrical measurement can also be taken while taking Raman spectroscopy using the customized holder.
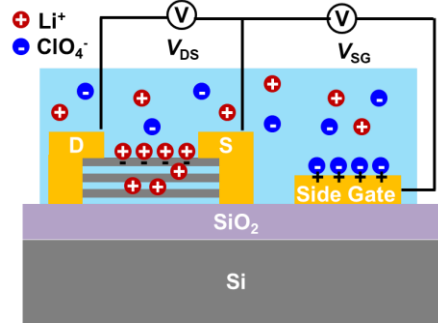
Figure 5.3: Side-view schematic of a TMDC-based Li electrolyte FET with connections for gated-Raman and electrical characterizations.

5.2 Li Electrolyte MoTe$_2$ and MoS$_2$ FETs

5.2.1 Li Electrolyte FETs Based on 2H/1T′ MoTe$_2$ homojunctions

Gated Raman experiments were first performed to verify if the phase transition in *in-situ*-grown few-layer 2H/1T′ MoTe$_2$ homojunctions can be induced by the PEO:LiClO$_4$ electrolyte gating. Figure 5.4a-b shows optical images of an MoTe$_2$ homojunction FET capped with PEO:LiClO$_4$ electrolyte before and after the gated Raman experiment. The side-gate voltage, V_{SG}, was applied between the side-gate electrode (not shown) and the contact electrode marked with GND. Figure 5.4c-d shows Raman spectra taken from the 2H-MoTe$_2$ channel when sweeping V_{SG} from 0 V to 5 V (positive sweep, Figure 5.4c) and then from -1 V to -5V (negative sweep, Figure 5.4d) with 0.5 V step. V_{SG} is kept within ± 5 V to avoid breakdown of the electrolyte as more than 1 µA leakage current is observed at V_{SG} = ± 5 V. When V_{SG} = 0 V, the characteristic phonon modes of the channel 2H-MoTe$_2$ are observed at A_{1g} 170 cm^{-1}, E_{2g}^1 234 cm^{-1}, and B_{2g} 289 cm^{-1}. The B_{2g} vibration mode is found to be absent in bulk and monolayer 2H-MoTe$_2$, but is allowed for few-layer MoTe$_2$ due to the breaking of translational symmetry [231]. All three peaks display a simultaneous intensity drop when V_{SG} is swept from 0 V

to 5V (Figure 5.4c), but phonon modes of few-layer 1T′-MoTe$_2$ (especially the B_g 166 cm^{-1} and A_g 258 cm^{-1} modes) are not observed. The reduction in peak intensity indicates degradation of the flake (confirmed by Figure 5.4b), which might be due to combined effects of laser heating and electrochemical reaction with Li$^+$ ions.
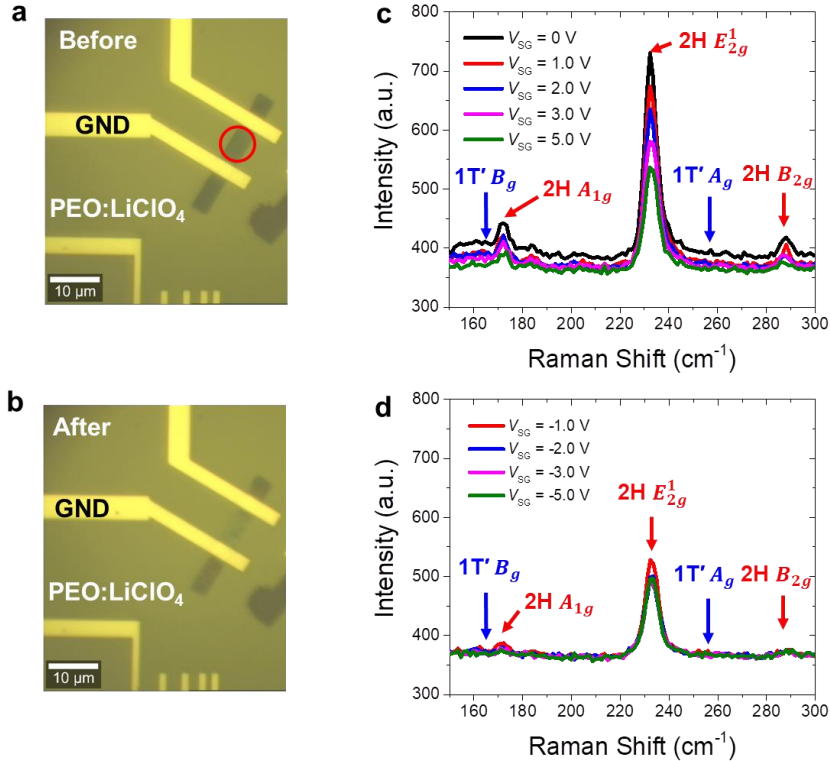
Figure 5.4: Gated-Raman characterization of few-layer (5-6 layers) 2H/1T′ MoTe$_2$ homojunction FET. (a-b) Optical image of the FET capped with PEO:LiClO$_4$ electrolyte (a) before and (b) after the gated Raman measurement. The side-gate electrode is not shown. (c-d) Raman spectra taken from the channel (within the red circle in (a)) when cycling the side-gate voltage, V_{SG}, (c) from 0 V to 5 V and (d) from -1 V to -5 V with step of 0.5 V. The typical Raman modes for 2H- and 1T′-MoTe$_2$ are indicated.

Figure 5.4d shows the evolution of Raman spectra when V_{SG} is swept negatively from -1 V to -5 V. Under negative V_{SG}, negative ClO$_4^-$ ions accumulate on the MoTe$_2$ surface inducing electrostatic charges in the MoTe$_2$, which is a nondestructive process. Therefore, no further degradation in peak intensity is observed under negative V_{SG}. Again,

no 1T′-MoTe$_2$ modes are observed. It is suspected that the carrier doping concentration induced by the PEO:LiClO$_4$ electrolyte gating is insufficient to trigger phase transition in few-layer MoTe$_2$ films.

5.2.2 Li Electrolyte FETs Based on Exfoliated MoTe$_2$

In order to verify if the PEO:LiClO$_4$ electrolyte has the capability to induce high enough carrier doping concentration, gated Raman experiments were performed on exfoliated monolayer (ML) 2H-MoTe$_2$ flakes. ML 2H-MoTe$_2$ flakes were exfoliated from bulk crystal using the mechanical exfoliation and then transferred onto a 300 nm SiO$_2$/Si substrate using the PDMS dry transfer method (described in Chapter 1.2). Li electrolyte FETs were fabricated on the ML 2H-MoTe$_2$ flakes following the fabrication process described in Chapter 5.1.1. An optical image of the fabricated device is shown in the inset of Figure 5.5a. Before carrying out the gated Raman experiment, the device characteristics of the Li electrolyte ML MoTe$_2$ FET were compared with substrate gating through the 300 nm SiO$_2$ substrate oxide and with side-gate gating through the PEO:LiClO$_4$ electrolyte (Figure 5.5a-b). The characterizations with substrate gating were taken before the application of the PEO:LiClO$_4$ electrolyte. With PEO:LiClO$_4$ gating, the ON-state drive current is increased by more than one order of magnitude and the subthreshold slope (SS) is reduced by more than 2 orders magnitude. A SS of ~ 100 mV/dec is achieved at $V_{DS} = 0.1$ V with the PEO:LiClO$_4$ gating, compared to > 15 V/dec with substrate gating. The results show that the PEO:LiClO$_4$ electrolyte provides a larger doping concentration than the 300 nm SiO$_2$ substrate, at even sub-1V. Larger doping levels are expected at even higher side-gate voltages, which might be sufficient for

inducing a phase transition in ML $MoTe_2$ flake. However, this phase transition cannot be detected electrically using this FET structure as it is based on an exfoliated $MoTe_2$ flake whose conductivity is limited by the contact resistance not by the channel resistance. Hence, the change of channel resistance will not be reflected significantly in the I_D-V_{DS} curves.
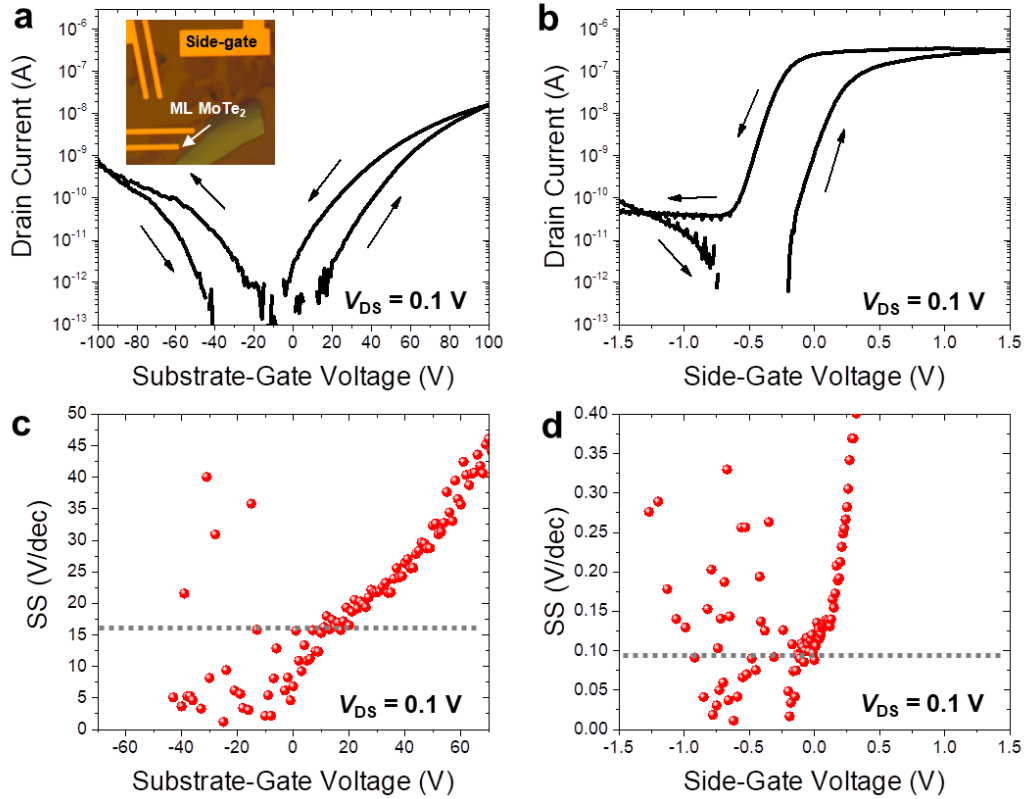
Figure 5.5: Transfer characteristics of a FET based on exfoliated monolayer (ML) $MoTe_2$ flake (a) with substrate gating and (b) with $PEO:LiClO_4$ electrolyte gating at $V_{DS} = 0.1$ V. Corresponding subthreshold slopes (SS) are shown in (c) and (d), respectively. The inset of (a) is an optical image of the device before the application of $PEO:LiClO_4$ electrolyte.

Alternatively, the phase transition was monitored at higher V_{SG} values using gated Raman spectroscopy. Due to the fact that ML $MoTe_2$ flakes degraded quickly before the V_{SG} reached a large value, multilayer $MoTe_2$ was used. This was particularly useful considering that few-layer $MoTe_2$ flakes are more stable and that Li^+ ions can intercalate

in-between layers inducing doping in each individual layer. Figures 5.6a-b show the evolution of the typical 2H modes, A_{1g}, E_{2g}^1, and B_{2g}, when sweeping V_{SG} from 0 V to 5 V (forward sweep) and then from 5 V back to 0 V (backward sweep). During the forward sweep (Figures 5.6a), all three peaks display a simultaneous intensity drop and shift to the left. A reversed trend is observed during the backward sweep (Figures 5.6b). However, the peak intensities are not fully recovered, reflecting a degradation of the flake. Especially, when V_{SG} is swept back to 0 V at the end of the backward sweep (black curve in Figure 5.6b), the peak intensities suddenly drop and the B_{2g} mode disappears, indicating a monolayer form. The degradation of the flake during the V_{SG} sweeps is shown in Figure B.14. The plot of the location of 2H A_{1g} peak vs. V_{SG} for both sweeps (Figure 5.4c) also shows reversible and hysteretic V_{SG} dependence. The location of the A_{1g} peak is at 166 cm^{-1} at high V_{SG} values, which coincides with the location of the 1T′ B_g peak. Since all 2H peaks are still present and no other 1T′ peaks appear, it is believed that this coincidence does not indicate a 2H/1T′ phase transition. Moreover, a slightly weaker response of the peak intensities and locations to V_{SG} is observed when V_{SG} is cycled negatively between 0 V and -4 V (Figure B.15). However, at negative V_{SG} there should not be any Li$^+$ intercalation in MoTe$_2$, so this gate voltage dependent behavior is likely due to electrostatic doping induced structural distortions. It is possible that Li$^+$ ions do not tend to intercalate into MoTe$_2$ even at high gate voltages, due to a low electron affinity of the MoTe$_2$. To further confirm this, layered MoTe$_2$ flakes were lithiated in organic lithium-containing solutions, such as n-butyl lithium (C$_4$H$_9$Li, n-BuLi), which has been successfully used to lithiate MoS$_2$ [95]. It is a chemical doping process wherein electrons are transferred from lithium carbon bond to the MoS$_2$: n-C$_4$H$_9$Li + MoS$_2$ →

LiMoS$_2$ + ½ n-C$_8$H$_{18}$ [232]. A few-layer MoTe$_2$ flake immersed in *n*-BuLi solution for up to 3 h did not show any sign of intercalation from the optical and Raman images (Figure B.17). It also has been reported that group VI TMDCs behave differently in lithium-containing solutions, either reacting with the entire reagent or being unreactive [232], which is still not well understood. The fact that MoTe$_2$ does not react with lithium may explain why phase transition was not observed in *in-situ*-grown few-layer MoTe$_2$ films under PEO:LiClO$_4$ electrolyte gating (Figure 5.4). In conclusion, under positive V_{SG} through the PEO:LiClO$_4$ electrolyte, Li$^+$ ions accumulate at the electrolyte-MoTe$_2$ interface creating an electric field and electrostatically inducing a large charge concentration on the top-most MoTe$_2$ layer; however, layers underneath cannot be doped since Li$^+$ ions do not intercalate layered MoTe$_2$; therefore phase transition cannot be induced.
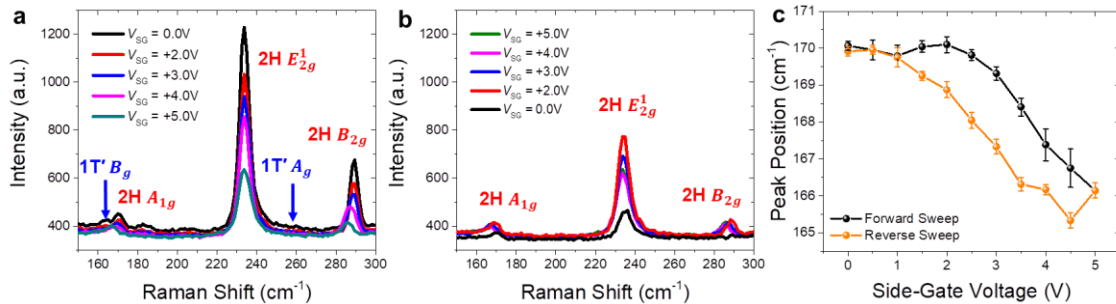
Figure 5.6: Gated-Raman characterization of an exfoliated few-layer MoTe$_2$ flake with PEO:LiClO$_4$ gating. (a-b) The evolution of Raman spectra when sweeping V_{SG} from (a) 0 V to 5 V (forward sweep) and (b) from 5 V to 0 V (backward sweep), with step of 0.5 V. (c) The evolution of the location of the 2H A_{1g} mode during both sweeps.

5.2.3   Li Electrolyte FETs Based on Pristine MoS$_2$

Since Li$^+$ intercalation can be induced in layered MoS$_2$ flakes by chemical doping via *n*-BuLi immersion, gated Raman experiments were performed to verify if Li$^+$

intercalation can also be induced by the PEO:LiClO$_4$ electrolyte and if the gate-controlled Li$^+$ intercalation has the capability to trigger the phase transition in MoS$_2$. The device fabrication starts with mechanical exfoliation and transfer of few-layer 2H-MoS$_2$ flakes on a 300 nm SiO$_2$/Si substrate. A ground (GND) electrode and side-gate electrode are patterned and deposited using standard electron beam lithographic process. The active regions are then covered with solid PEO:LiClO$_4$ electrolyte. Figure 5.7 is an optical image of the Li electrolyte MoS$_2$ device.
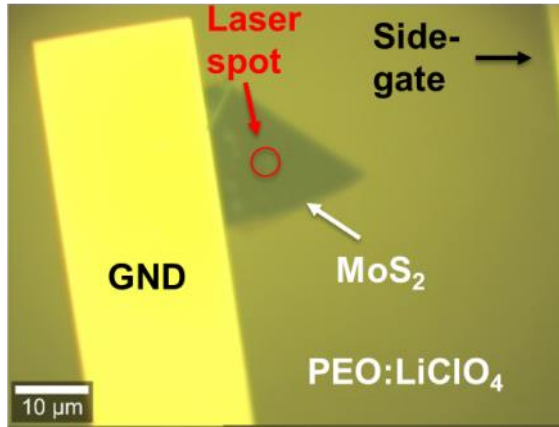
Figure 5.7: Optical image of an exfoliated few-layer MoS$_2$ flake contacted with a GND electrode and capped with PEO:LiClO$_4$ electrolyte.

Figures 5.8a-g show the evolution of zone-center phonon E^1_{2g} 383 cm^{-1} and A_{1g} 408 cm^{-1} modes of 2H-MoS$_2$ when sweeping V_{SG} from 0 V to 5 V. As depicted in the inset of Figure 5.8a, the A_{1g} phonon involves the sulfur atomic vibration in the opposite direction out of the basal plane, whereas the E^1_{2g} mode involves the displacement of Mo and sulfur atoms in the basal plane. The mode frequencies, ω, and the corresponding full width at half maximum (FWHM) were obtained by fitting a sum of two Lorentzians to the spectra.
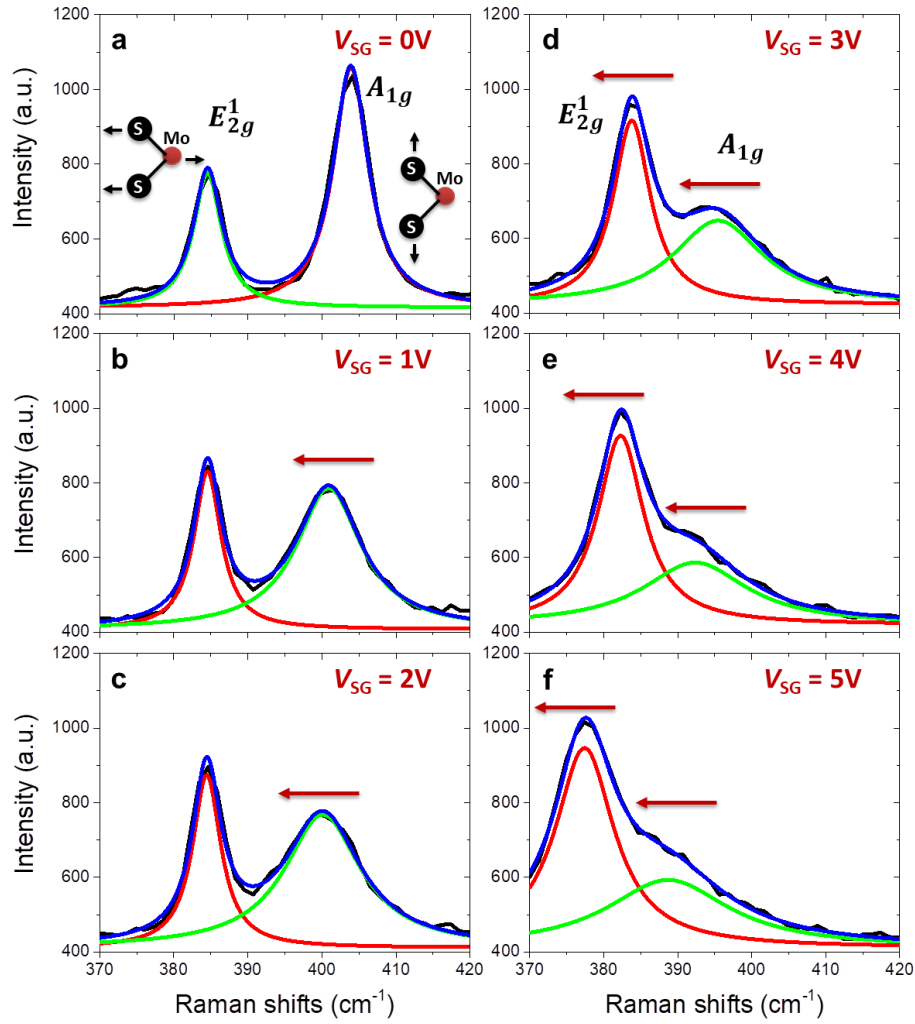
Figure 5.8: (a-f) Raman spectra of the PEO:LiClO$_4$ gated 2H-MoS$_2$ flake at different side-gate voltages V_{SG}. The black curves are the experimental Raman spectra, the blue curves are Lorentzian fits to the total spectrum, and the red and green curves are the Lorentzian fit to the E^1_{2g} (in-plane) and A_{1g} (out-of-plane) peaks, respectively.

Figures 5.9a and 5.9b show the shift of ω and corresponding FWHM, as a function of V_{SG}, respectively. At low V_{SG} values (within 3V), the linewidth of the A_{1g} mode increases significantly whereas the linewidth of the E^1_{2g} mode does not show any appreciable change. The observation is consistent with the DFT results by B. Chakraborty *et al.* which states that A_{1g} mode couples more strongly with electrons than the E^1_{2g} mode

as the structural distortions in the A_{1g} mode do not break the symmetry of MoS_2 leading to a large electron-phonon coupling (EPC) [228]. The reversible shifting of the A_{1g} mode of $2H$-$MoTe_2$ in Figure 5.6 may be explained by this electrostatic doping induced EPC effect.
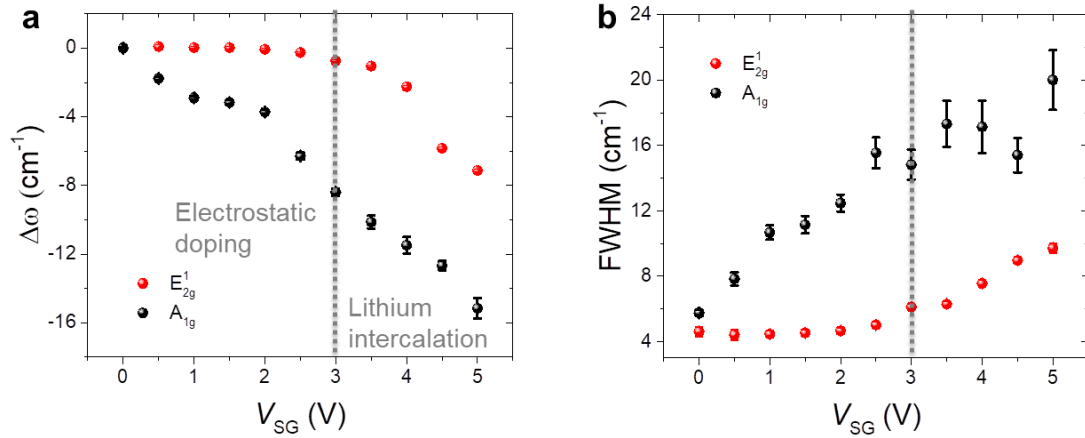
Figure 5.9: Change in the (a) phonon frequency $\Delta\omega$ and (b) FWHM of E_{2g}^1 and A_{1g} modes as a function of V_{SG}.

At high V_{SG} values (beyond 3V), both the 2H A_{1g} and E_{2g}^1 modes show significant softening and broadening, which might be attributed to the lattice expansion, distortion, and strain caused by the gate-controlled intercalation. Figure 5.10 shows Raman spectra of the PEO:LiClO$_4$ gated 2H-MoS$_2$ flake when cycling V_{SG} between 0 V and 5V in a wider wavelength range. The softening and broadening of the 2H A_{1g} and E_{2g}^1 modes are partially reversible, which might be attributed to degradation of the flake by Li$^+$ intercalation. However, no 1T'-MoS$_2$ phonon modes are observed even at high V_{SG} values, indicating that the intercalated Li$^+$ concentration by the electrolyte gate may be insufficient for triggering the phase transition in layered MoS$_2$. The chemical intercalation by organic n-BuLi solution may result in a higher intercalated Li$^+$

concentration than the gate-controlled electrochemical intercalation and therefore could induce the phase transition.
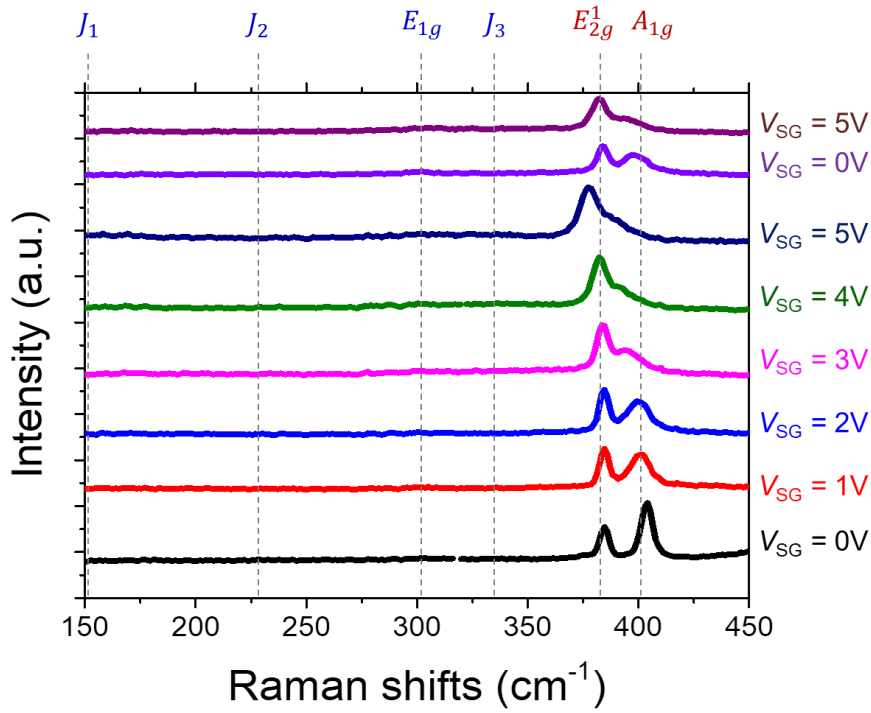
Figure 5.10: Raman spectra of the PEO:LiClO$_4$ gated 2H-MoS$_2$ flake when cycling V_{SG} between 0 V and 5V. The locations of E_{2g}^1 (383 cm^{-1}) and A_{1g} (408 cm^{-1}) peaks for 2H-MoS$_2$, and J_1 (156 cm^{-1}), J_2 (228 cm^{-1}), E_{1g} (305 cm^{-1}), and J_3 (330 cm^{-1}) peaks for 1T'-MoS$_2$ are indicated.

5.3 Phase Transition in Pre-lithiated MoS$_2$

Figure 5.11 shows the calculated energy barrier of the phase transition in monolayer MoS$_2$ from 2H to 1T by J. Xia *et al.* using the nudged elastic band (NEB) method [233]. With the aid of Li$^+$ intercalation (red curve), the energy barrier between 2H and 1T phase is lowered compared to the case without Li$^+$ (black curve), making the 2H/1T′ phase transition much easier to realize. Here, it is proposed to pre-lithiate the exfoliated pristine 2H-MoS$_2$ flakes by immersion in organic *n*-BuLi solution for an

appropriate amount of time to reduce the energy barrier and then induce the phase

transition through the gate-controlled Li^+ intercalation.
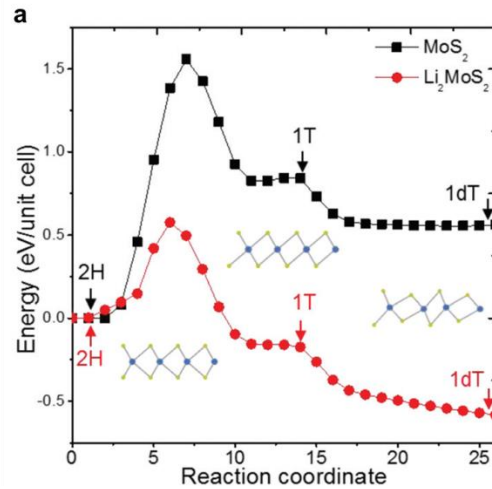
Figure 5.11: Transformation energy barrier of monolayer MoS_2 from the 2H to 1T′ to 1dT phase by calculation. Transformation energy barrier of monolayer MoS_2 from the 2H to 1T to 1dT phase by nudged elastic band (NEB) calculation. The black/red curve with discrete transient states depicts the energy change of the phase evolution from 2H to 1T to 1dT without/with Li+ participation. The reaction coordinates at 1, 13 and 26 represent 2H, 1T and 1dT phases and their atomic structures are inserted beside them. Reprinted with permission from reference [233].

5.3.1 Pre-lithiation Treatment

The pre-lithiation of few-layer $2H\text{-}MoS_2$ flakes transferred on a SiO_2/Si substrate

was performed by immersing the samples in n-BuLi solution for 3 h and rinsing with

hexane in a glove box. Figure 5.12a shows an optical image of a ~17 nm-thick MoS_2

flake after 3 h immersion in n-BuLi solution. Regions with different optical contrasts are

observed. The contrast change in the lithiated MoS_2 is due to an enhancement in optical

transmission that results from the doping provided by the Li intercalation. It is also

observed in Figure 5.12a that Li^+ ions enters the MoS_2 vdW gaps from the edges and

diffuses towards the center, as the edge areas show darker optical contrast than the center

regions.

To further investigate the structural properties of the lithiated regions with different optical contrast, we carried out Raman mapping measurements on the pre-lithiated MoS_2 flake. Raman spectrum (black curve, Figure 5.12b) taken from the brighter region (marked with 1) shows the two strong 2H-MoS_2 peaks, E_{2g}^1 (383 cm^{-1}) and A_{1g} (408 cm^{-1}), and one weak 1T'-MoS_2 peak, J_1 (156 cm^{-1}), while the Raman spectrum (red curve, Figure 5.12b) taken from the darker region (marked with 2) shows two weak 2H-MoS_2 E_{2g}^1 and A_{1g} peaks and four strong 1T'-MoS_2 peaks, J_1, J_2 (228 cm^{-1}), E_{1g} (305 cm^{-1}), J_3 330 cm^{-1}. The results show that both regions are 'mix-phased' but the structure of the brighter region is closer to 2H phase (2H-dominated region) whereas the structure of the darker region is closer to 1T' phase (1T'-dominated region). Raman intensity maps (Figure 5.12c) of the 2H E_{2g}^1 peak and the 1T' J_1 peak show that the darker contrast reflects a higher Li$^+$ concentration. Since the Raman spectra of the pre-lithiated MoS_2 show both 2H and 1T' phonon modes, one would expect that that the phase transition will require much less additional charge transfer than pristine MoS_2.
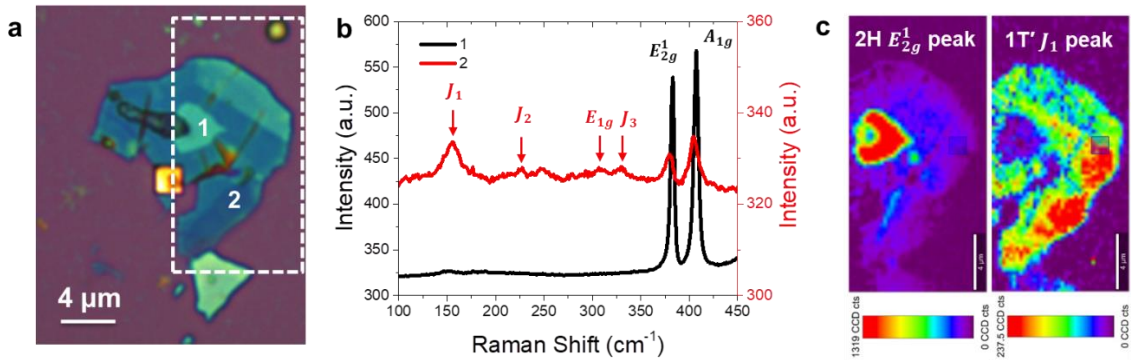
Figure 5.12: (a) Optical image of a ~17 nm-thick MoS_2 flake after 3 h immersion in *n*-BuLi. (b) Raman spectra taken from the points marked by 1 and 2 in (a). (c) Raman intensity maps of 2H E_{2g}^1 383 cm^{-1} peak (left) and 1T' J_1 156 cm^{-1} peak (right) of the region in the white dashed box in (a).

5.3.2 Reversible Phase Transition in Pre-lithiated MoS$_2$ Flake

To verify if the phase of the pre-lithiated MoS$_2$ can be modulated by the gate-controlled Li$^+$ intercalation, gated Ramen experiments were performed on the pre-lithiated MoS$_2$ flake shown in Figure 5.12a. Figure 5.13a shows an optical image of the flake with the ground contact. The flake is capped with PEO:LiClO$_4$ electrolyte before carrying out the Raman experiments. Raman maps of 2H A_{1g} peak and 1T$'$ J_1 peak at zero side gate voltage ($V_{SG} = 0$ V) (Figure 5.13b) reveals that the edge regions, which were 1T$'$-dominated after immersion in n-BuLi, became 2H-dominated after the device fabrication, indicating a de-lithiation process may have occurred during the liftoff of the electrode metals in acetone.

Figures 5.13b-e show the evolution of the 2H A_{1g} and 1T$'$ J_1 peak intensities when cycling V_{SG} between 0 V and 3V. Reversible change in 2H A_{1g} peak intensity was observed due to the softening and broadening of the peak caused by electrostatic doping, similar to the observation in the exfoliated MoS$_2$ flake (Figure 5.8-5.9). No noticeable change in 1T$'$ J_1 peak intensity suggests that phase transition cannot be induced below $V_{SG} = 3$ V. When V_{SG} is swept to 4 V, the intensity of the 2H A_{1g} peak of the edge (2H-dominated) regions almost disappears, while the intensity of the 1T$'$ J_1 peak is increased dramatically (Figure 5.13f). The edge regions convert to the 1T$'$ phase and the phase transition happens at V_{SG} between 3 V and 4 V. A gradual increase (decrease) of the 2H A_{1g} (1T$'$ J_1) peak intensity was observed as V_{SG} is swept back to 0 V (Figure 5.13f-j). The observed phase transition in pre-lithiated 2H-dominated MoS$_2$ is reversible with a small hysteresis due to the slow movement of the ions in the electrolyte.
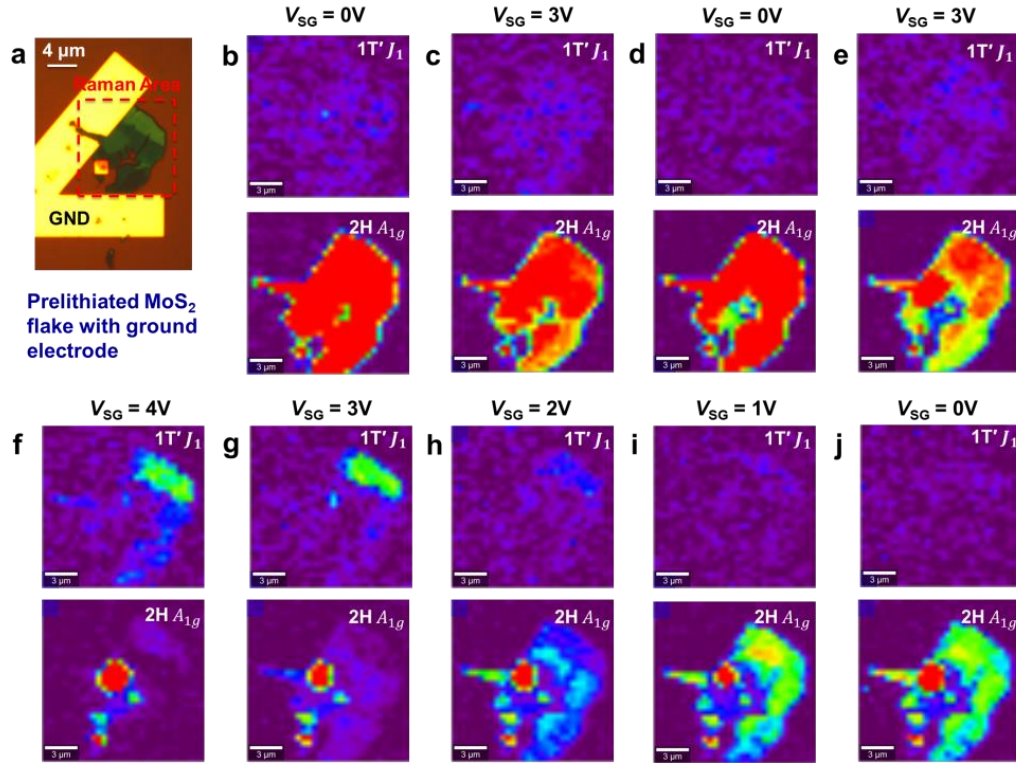
Figure 5.13: (a) Optical image of a pre-lithiated MoS_2 flake with the ground contact. (b-e) The evolution of the 2H-MoS_2 A_{1g} and 1T′-MoS_2 J_1 peak intensities when cycling the side-gate voltage, V_{SG}, between 0 V and 3V. (f-j) The evolution of the 2H A_{1g} and 1T′ J_1 peak intensities (on the same scale) when sweeping V_{SG} from 4 V to 0 V.

This hysteresis can also be interpreted through the Raman intensity of the 1T′ J_1 peak to the intensity over both 1T′ J_1 and 2H A_{1g} peaks: F = 1T′ (J_1) / [1T′ (J_1) + 2H (A_{1g})]. The V_{SG} dependence of F for the forward and reverse sweeps is plotted in Figure 5.14. Below 3 V in the forward sweep, F remains around zero, meaning that the 2H phase is still dominant and the fraction of 1T′ is negligible. When V_{SG} is increased to 4 V, F sharply rises to ~1 suggesting a nearly complete transition to the 1T′ phase. When V_{SG} is swept backwards, the flake remains in the 1T′ phase until the bias is reduced to 3V. The 2H phase begins to recur as V_{SG} is continuously lowered, but is not fully recovered at 0 V, which is attributed to the remaining Li^+ ions intercalated in-between the MoS_2 layers. A

negative bias might be needed to fully restore the 2H phase. Again, degradation of the flake occurs under large side-gate V_{SG}, due to Li^+ intercalation and/or other electrochemical reactions between MoS_2 and Li^+ ions which is accelerated by the adsorbed H_2O molecules from the atmosphere. To sum up, the fast response below $V_{SG} = 3V$ is an electrostatic doping process, while the hysteretic response above $V_{SG} = 3V$ is due to lithiation / de-lithiation.
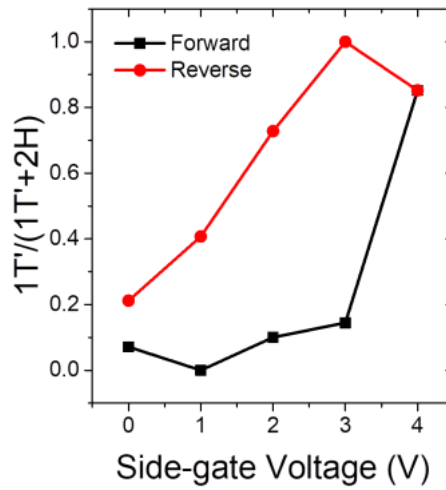
Figure 5.14: Gate-dependent Raman intensity ratios. The y-axis is the Raman intensity of the 1T′ J_1 peak to the intensity over both 1T′ J_1 and 2H A_{1g} peaks: F = 1T′ (J_1) / [1T′ (J_1) + 2H (A_{1g})]. The black and red curves are for the forward and reverse V_{SG} sweeps, respectively. The ratio shows hysteresis under the side-gate voltage scan. The transformation of phonon modes and the corresponding hysteresis loop indicate a phase transition between 2H and 1T′ phases under side-gate voltage through the PEO:LiClO$_4$ electrolyte.

5.3.3 Transport characteristics of pre-lithiated 2H- and 1T′-dominanted MoS_2

Having observed reversible phase transition in a 2H-dominated MoS_2 flake by gate-controlled Li^+ intercalation, a fabrication process to utilize this structure in a proposed PCM device concept has been developed. The process starts with patterning contact regions to the flakes using electron beam lithography. With the PMMA patterns

for contacts, the 2H-MoS$_2$ in the contact regions is converted to metallic (1T′ or 1T′-dominated) phase by immersing the substrate in n-BuLi solutions for > 4 h. After the deposition and liftoff of contact metal, the 2H-MoS$_2$ in the channel region is also treated with the n-BuLi solutions for < 2 h so that it turns to a semiconducting 2H-dominated phase. The immersion time depends on the concentration of the n-BuLi solutions and the thickness of the MoS$_2$ flakes, which needs to be further calibrated.

To validate this idea, transport characteristic measurements were carried out to verify if the pre-lithiated 2H-dominated (1T′-dominated) MoS$_2$ is semiconducting (metallic). Figure 5.15a shows an optical image of a few-layer MoS$_2$ flake after 3h treatment in n-BuLi solution. Raman spectra (Figure 5.15b) taken from the regions marked by 1, 2 and 3 in Figure 5.14a show that the outer darker regions (marked by 3) are 1T′-dominated whereas the center regions (marked by 1 and 2) are 2H-dominated.

Next, FETs were fabricated on the 2H-dominated, 1T′-dominated, and 2H-dominated/1T′-dominated heterojunction regions (5.15c). Room-temperature transfer characteristics of these devices as well as a pristine MoS$_2$ FET are shown in Figure 5.15d. The n-type doping effect from lithiation is confirmed by a left shift of the threshold voltage of the FET based on the 2H-dominated MoS$_2$ (red curve), compared to the pristine MoS$_2$ FET (magenta curve). The FET based on the 2H-dominated MoS$_2$ shows a current on-off ratio of 10^7 and a steep subthreshold slope, implying that the pre-lithiated 2H-dominated MoS$_2$ is still semiconducting and can be used as channel material. Unexpectedly, the FET based on 1T′-dominated MoS$_2$ (black curve) did not exhibit high ON-state drive current. This result is believed to be due to large resistance of the metal contacts to the 1T′-dominated region, which is likely due to the contamination (LiOH,

Li$_2$CO$_3$) from the reaction of *n*-BuLi with H$_2$O and CO$_2$. The following is one potential

reaction sequence: C$_4$H$_9$Li + H$_2$O → C$_4$H$_{10}$ + LiOH and 2 LiOH + CO$_2$ → Li$_2$CO$_3$ + H$_2$O

or C$_4$H$_9$Li + CO$_2$ → C$_4$H$_9$CO$_2$Li. The contaminants are indicated with white arrows in the

optical image (Figure 5.14a). The existence of Co_3^{2-} on the surface of the flakes after the

n-BuLi treatment is confirmed by XPS (Figure B.17). The performance of the 2H-

dominated/1T′-dominated heterojunction FETs (blue curve) was also limited by the large

contact resistance at the metal/1T′ interface. However, conductance modulation was

observed, suggesting that this approach is promising if the surface contamination issues

can be addressed.
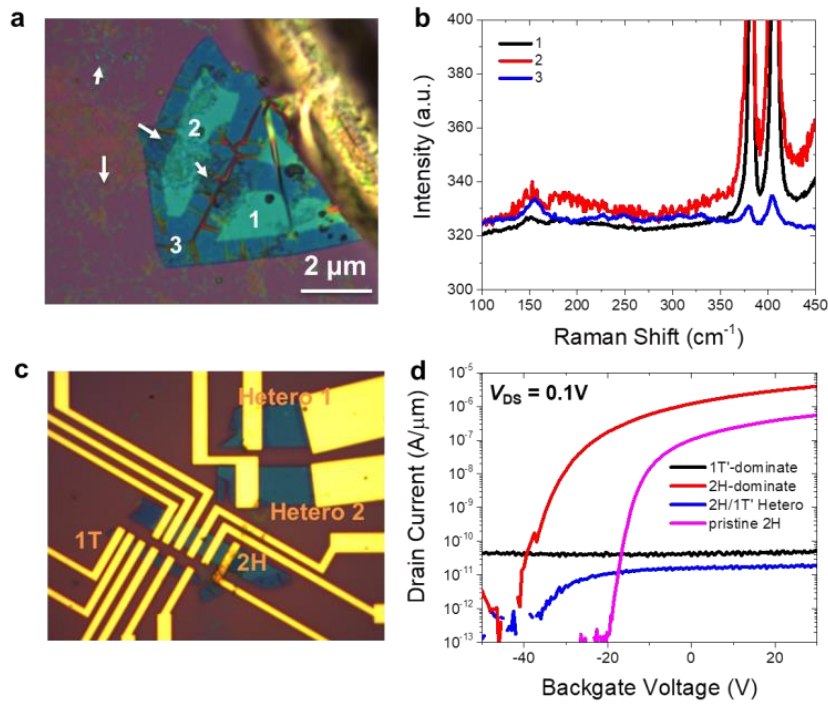
Figure 5.15: Transport characteristics of pre-lithiated 2H- and 1T′-dominanted MoS$_2$. (a) Optical image of a few-layer MoS$_2$ flake on SiO$_2$/Si substrate after immersion in *n*-BuLi for 3 h. (b) Raman spectra taken from the points marked by 1-3 in (a). The inner brighter regions are 2H-dominated while the outer darker regions are 1T′-dominated. (c) An optical images of the FETs made on the flake including 2H-dominated-only, 1T′-dominated-only and 2H-dominated/1T′-dominated heterojunction devices. (d) Transfer characteristics of the three types of devices with back substrate gating at V_{DS} = 0.1 V.

5.4 Summary

In summary, a reversible phase transition in few-layer pre-lithiated 2H-MoS$_2$ flakes by gate-controlled Li$^+$ intercalation through a solid PEO:LiClO$_4$ electrolyte has been demonstrated. The pre-lithiated 2H-MoS$_2$ possess excellent semiconducting properties and requires less additional doping to transform into the metallic 1T′ phase. The gate-controllable phase transition in the pre-lithiated 2H-MoS$_2$ can be implemented in phase-change memory applications. Future work includes understanding and eliminating the degradation of the flakes and evaluating the electrical behavior of the Li$^+$-intercalation-induced phase change.

CHAPTER 6   CONCLUSION AND OUTLOOK

In this dissertation I have presented my experimental work on phase-engineered field-effect transistors (FETs) based on two-dimensional (2D) transition metal dichalcogenides (TMDCs). The contact resistance at the source/drain metal/TMDC interface in TMDC-based FETs is far above the projected allowable values for future high-performance applications, mainly due to the strong Fermi level pinning at the interface. This dissertation aimed to find a solution to the large contact resistance and further implement the TMDC-based FETs with lowered contact resistance in novel applications.

First, in chapter 2, I presented an *in situ* flux-controlled phase-engineering method for the synthesis of lateral metal-semiconductor (2H/1T′) MoTe$_2$ homojunctions. Detailed material characterizations of the i*n-situ*-grown homojunctions reveal that nearly-single-crystalline 2H domains stitch to polycrystalline 1T′ domains with an abrupt interface. This lateral 2H/1T′ MoTe$_2$ homojunction itself is a 2D edge contact, which may result in ultra-low contact resistance if the interface has a small Schottky barrier height (SBH).

Next, in chapter 3, I presented the study on the electrical properties of the i*n-situ*-grown homojunctions by performing temperature-dependent transport characterizations on MoTe$_2$ homojunction FETs of which the channel regions are 2H phase the contact regions are 1T′ phase. With the phase-engineered 1T′ contacts, the device showed improved p-type behavior with a low contact resistance less than 0.5 kΩ·µm, compared to the MoTe$_2$ FETs with 2H contacts. The SBH for hole injections at the 2H/1T′ MoTe$_2$ interface was found far below the value at the metal (Ti)/2H interface at any gat bias

conditions. The extracted flat-band SBH is only 10's meV. The results showed that the lateral 2H/1T′ MoTe$_2$ homojunction is an ideal contact for p-MOSFETs.

Due to lack of controllability in the size and location of the homojunctions, the *in situ* flux-controlled synthesis method is impractical for large-scale production. In chapter 4, I presented a two-step lithographic synthesis approach for creating large-scale various lateral TMDC junctions in sequence. Using this two-step approach, *sequentially*-grown lateral MoTe$_2$ homojunction p-MOSFETs were fabricated, which showed similar behavior to *in-situ*-grown MoTe$_2$ homojunction p-MOSFETs. This two-step approach was further utilized to fabricate lateral 2H-MoS$_2$/1T′-MoTe$_2$ heterojunction n-MOSFETs with high current on/off ratio and low OFF-state leakage current. The results imply the potential of utilizing this two-step method to fabricate complementary TMDC-based MOSFETs.

Due to the large reduction in contact resistance, dynamical and reversible control of the channel resistance via the semiconducting 2H to metallic 1T′ transition can make phase-engineered TMDC FETs operate as phase-change memory (PCM) devices. Finally, in chapter 5, I presented a reversible phase transition in few-layer pre-lithiated semiconducting 2H-MoS$_2$ flakes by gate-controlled Li$^+$ intercalation through a solid PEO:LiClO$_4$ electrolyte. This gate-controlled Li$^+$ intercalation induced phase transition enable the use of lateral junctions between pre-lithiated semiconducting and metallic TMDCs for PCM application.

Additional challenges for TMDC FETs with phase-engineered contacts includes: (1) improving the interface between the substrate oxide and TMDC to reduce interface traps, which should lead to improved device performance; (2) investigating the band

alignments of various TMDC metallic-semiconducting junctions to ensure that complementary contacts can be achieved; (3) developing techniques to incorporate doping at the contacts to further lower the contact resistance and the effective SBH; (4) optimizing the device geometry of phase-engineered TMDC FETs to achieve higher performance, such as scaled top-gated MOSFETs with self-aligned, phase-engineered contacts, as illustrated in Figure 4.9. This process requires the integration of ultra-thin high-quality high-κ dielectric on TMDCs.

Additional challenges for implementing TMDC phase-change memories includes: (1) fabricating lateral junctions between pre-lithiated semiconducting TMDC (such as MoS_2) and other metallic TMDCs with low injection barriers. Such a structure can electrically read out the change of channel resistance under gate-controlled phase transition through a Li electrolyte, thus operating as a PCM device; (2) finding solutions to eliminating degradation of the flakes to improve the reproducibility, such as exploring other nondestructive phase change mechanisms, and solutions to mitigate the hysteresis effect due to the slow movement of ions; (3) developing synthesis approaches to synthesize monolayer TMDCs or their alloys to reduce the transition gate voltage. Monolayer TMDCs requires less carrier doping concentration (gate voltages) to undergo a structural phase transition. Theoretical computations showed that the free energy difference between the 2H and 1T′ phases can be made arbitrarily small by varying the fraction of W (1-x) in $Mo_xW_{1-x}Te_2$ alloy [192, 234]; (4) optimizing the geometry of solid electrolyte gated devices to improve the speed, such as integration of top-gate electrodes.

REFERENCES

[1] K. S. Novoselov, A. K. Geim, S. V. Morozov, D. Jiang, Y. Zhang, S. V. Dubonos, I. V. Grigorieva, and A. A. Firsov, "Electric Field Effect in Atomically Thin Carbon Films," *Science*, vol. 306, no. 5696, pp. 666–669, 2004.

[2] G. E. Moore, "Cramming more components onto integrated circuits," *Electronics*, vol. 38, no. 8, pp. 114–117, 1965.

[3] K. Mistry, *10 nm Technology Leadership*. https://newsroom.intel.com/newsroom/wp-content/uploads/sites/11/2017/03/Kaizad-Mistry-2017-Manufacturing.pdf.

[4] J. Lu, "Elastic properties of carbon nanotubes and nanoropes," *Phys. Rev. Lett.*, vol. 79, no. 7, pp. 1297–1300, 1997.

[5] M. Y. Han, B. Özyilmaz, Y. Zhang, and P. Kim, "Energy Band-Gap Engineering of Graphene Nanoribbons," *Phys. Rev. Lett.*, vol. 98, no. 20, pp. 206805, 2007.

[6] G. Giovannetti, P. A. Khomyakov, G. Brocks, P. J. Kelly, and J. van den Brink, "Substrate-induced band gap in graphene on hexagonal boron nitride: *Ab initio* density functional calculations," *Phys. Rev. B*, vol. 76, no. 6, pp. 073103, 2007.

[7] F. Xia, D. B. Farmer, Y.-M. Lin, and P. Avouris, "Graphene Field-Effect Transistors With High on/off Current Ratio and Large Transport Band Gap at Room Temperature," *Nano Lett.*, vol. 10, no. 2, pp. 715–718, 2010.

[8] S. Y. Zhou, G.-H. Gweon, A. V. Fedorov, P. N. First, W. A. de Heer, D.-H. Lee, F. Guinea, A. H. Castro Neto, and A. Lanzara, "Substrate-Induced Bandgap Opening in Epitaxial Graphene," *Nature Mater.*, vol. 6, pp. 770–775, 2007.

[9] S. Xiao, J.-H. Chen, S. Adam, E. D. Williams, and M. S. Fuhrer, "Charged impurity scattering in bilayer graphene," *Phys. Rev. B*, vol. 82, pp. 041406(R), 2010.

[10] S. Y. Lee, D. L. Duong, Q. A. Vu, Y. Jin, P. Kim, and Y. H. Lee, "Chemically Modulated Band Gap in Bilayer Graphene Memory Transistors with High On/Off Ratio," *ACS Nano*, vol. 9, no. 9, pp. 9034–9042, 2015.

[11] E. J. Olson, R. Ma, T. Sun, M. A. Ebrish, N. Haratipour, K. Min, N. R. Aluru, and S.

J. Koester, "Capacitive Sensing of Intercalated H_2O Molecules Using Graphene," *ACS Appl. Mater. Interfaces*, vol. 7, no. 46, pp. 25804–25812, 2015.

[12] Y. Zhang, R. Ma, Y. C. Kudva, P. Bühlmann, and S. J. Koester, "Glucose Sensing with Graphene Varactors," *IEEE Sensors*, 2016.

[13] R. Ma, Q. Su, J. Li, and S. J. Koester, "Acetone Sensing Using Graphene Quantum Capacitance Varactors," *IEEE Sensors*, 2016.

[14] Y. Zhang, R. Ma, X. V. Zhen, Y. C. Kudva, P. Bühlmann, and S. J. Koester, "Capacitive Sensing of Glucose in Electrolytes Using Graphene Quantum Capacitance Varactors," *ACS Appl. Mater. Interfaces*, vol. 9, no. 44, pp. 38863–38869, 2017.

[15] C. D. Liang, R. Ma, Y. Su, A. O'Hara, E. X. Zhang, M. L. Alles, P. Wang, S. E. Zhao, S. T. Pantelides, Steven J Koester, R. D. Schrimpf, and D. M. Fleetwood, "Defects and Low-Frequency Noise in Irradiated Black Phosphorus MOSFETs with HfO_2 Gate Dielectrics," *IEEE Trans. Nucl. Sci.*, vol. 65, no. 6, pp. 1227–1238, 2018.

[16] C. D. Liang, R. Ma, K. Li, Y. Su, H. Gong, K. L. Ryder, P. Wang, A. L. Sternberg, E. X. Zhang, M. L. Alles, R. A. Reed, S. J. Koester, D. M. Fleetwood, and R. D. Schrimpf, "Laser-Induced Single-Event Transients in Black Phosphorus MOSFETs," *IEEE Trans. Nucl. Sci.*, vol. 66, no. 1, pp. 384–388, 2019.

[17] R. Ma, H. Zhang, Y. Yoo, Z. P. Degregorio, L. Jin, P. Golani, J. G. Azadani, T. Low, J. E. Johns, L. A. Bendersky, A. V. Davydov, and S. J. Koester, "$MoTe_2$ Lateral Homojunction Field-Effect Transistors Fabricated using Flux-Controlled Phase Engineering," *ACS Nano*, vol. 13, no. 7, pp. 8035–8046, 2019.

[18] M. Chhowalla, H. S. Shin, G. Eda, L.-J. Li, K. P. Loh, and H. Zhang, "The chemistry of two-dimensional layered transition metal dichalcogenide nanosheets," *Nat. Chem.*, vol. 5, pp. 263–275, 2013.

[19] B. Radisavljevic, A. Radenovic, J. Brivio, V. Giacometti, and A. Kis, "Single-layer MoS_2 transistors," *Nat. Nanotechnol.*, vol. 6, pp. 147–150, 2011.

[20] K. K. Kam, and B. A. Parkinson, "Detailed photocurrent spectroscopy of the semiconducting group-VIB transition metal dichalcogenides," *J. Phys. Chem.*, vol. 86, no. 4, pp. 463–467, 1982.

[21] R. G. Dickinson, and L. Pauling, "The crystal structure of molybdenite," *J. Am.*

Chem. Soc., vol. 45, no. 6, pp. 1466–1471, 1923.

[22] R. F. Frindt, and A. D. Yoffe, "Physical properties of layer structures: optical properties and photoconductivity of thin crystals of molybdenum disulphide," *Proc. R. Soc. A*, vol. 273, no. 1352, pp. 69–83, 1963.

[23] X. Wang and F. Xia, "Van der Waals heterostructures: Stacked 2D materials shed light," *Nat. Mater.*, vol. 14, pp. 264–265, 2015.

[24] C. Gong, H. Zhang, W. Wang, L. Colombo, R. M. Wallace, and K. Cho, "Band alignment of two-dimensional transition metal dichalcogenides: Application in tunnel field effect transistors," *Appl. Phys. Lett.*, vol. 103, no. 5, pp. 053513, 2013.

[25] A. Splendiani, L. Sun, Y. Zhang, T. Li, J. Kim, C.-Y. Chim, G. Galli, and F. Wang, "Emerging Photoluminescence in Monolayer MoS_2," *Nano Lett.*, vol. 10, no. 4, pp. 1271–1275, 2010.

[26] K. Dileep, R. Sahu, S, Sarkar, S. C. Peter, and R. Datta, "Layer specific optical band gap measurement at nanoscale in MoS_2 and ReS_2 van der Waals compounds by high resolution electron energy loss spectroscopy," *J. Appl. Phys.*, vol. 119, no. 11, 114309, 2016.

[27] T. Mueller, F. Xia, and P. Avouris, "Graphene photodetectors for high-speed optical communications," *Nat. Photonics*, vol. 4, pp. 297–301, 2010.

[28] C. D. English, G. Shine, V. E. Dorgan, K. C. Saraswat, and E. Pop, "Improved Contacts to MoS_2 Transistors by Ultra-High Vacuum Metal Deposition," *Nano Lett.*, vol. 16, no. 6, pp. 3824–3830, 2016.

[29] Y. Liu, X. Duan, Y. Huang, and X. Duan, "Two-dimensional transistors beyond graphene and TMDCs," *Chem. Soc. Rev.*, vol. 47, no. 16, pp. 6388–6409, 2018.

[30] S. Manzeli, D. Ovchinnikov, D. Pasquier, O. V. Yazyev, and A. Kis, "2D transition metal dichalcogenides," *Nat. Rev. Mater.*, vol. 2, pp. 17033, 2017.

[31] X. Qian, J. Liu, L. Fu, and J. Li, "Quantum spin Hall effect in two-dimensional transition metal dichalcogenides," *Science,* vol. 346, no. 6215, pp. 1344–1347, 2014.

[32] K.-A. N. Duerloo, Y. Li, and E. J. Reed, "Structural phase transitions in two-

dimensional Mo- and W-dichalcogenide monolayers," *Nat. Commun.*, vol. 5, no. 4214, 2014.

[33] D. H. Keum, S. Cho, J. H. Kim, D.-H. Choe, H.-J. Sung, M. Kan, H. Kang, J.-Y. Hwang, S. W. Kim, H. Yang, K. J. Chang, and Y. H. Lee, "Bandgap opening in few-layered monoclinic MoTe$_2$," *Nat. Phys.*, vol. 11, pp. 482–486, 2015.

[34] W. Choi, N. Choudhary, G. H. Han, J. Park, D. Akinwande, and Y. H. Lee, "Recent development of two-dimensional transition metal dichalcogenides and their applications," *Material Today*, vol. 20, no. 3, pp. 116–130, 2017.

[35] R. Beams, L. G. Cançado, S. Krylyuk, I. Kalish, B. Kalanyan, A. K. Singh, K. Choudhary, A. Bruma, P. M. Vora, F. Tavazza, A. V. Davydov, and S. J. Stranick, "Characterization of Few-Layer 1T' MoTe$_2$ by Polarization-Resolved Second Harmonic Generation and Raman Scattering," *ACS Nano*, vol. 10, no. 10, pp. 9626–9636, 2016.

[36] J. A. Wilson and A. D. Yoffe, "The transition metal dichalcogenides discussion and interpretation of the observed optical, electrical and structural properties," *Adv. Phys.*, vol. 18, no. 73, pp. 193–335, 1969.

[37] Y. Yoo, Z. P. DeGregorio, Y. Su, S. J. Koester, and J. E. Johns, "In-Plane 2H-1T' MoTe$_2$ Homojunctions Synthesized by Flux-Controlled Phase Engineering," *Adv. Mater.*, vol. 29, no. 16, pp. 1605461, 2017.

[38] H. M. Hill, A. F. Rigosi, K. T. Rim, G. W. Flynn, and T. F. Heinz, "Band alignment in MoS$_2$/WS$_2$ transition metal dichalcogenide heterostructures probed by scanning tunneling microscopy and spectroscopy," *Nano Lett.*, vol. 16, no. 8, pp. 4837–4837, 2016.

[39] P. Rivera, H. Yu, K. L. Seyler, N. P. Wilson, W. Yao, and X. Xu, "Interlayer valley excitons in heterobilayers of transition metal dichalcogenides," *Nat. Nanotechnol.*, vol. 13, pp. 1004–1015, 2018.

[40] K. L. Seyler, D. Zhong, B. Huang, X. Linpeng, N. P. Wilson, T. Taniguchi, K. Watanabe, W. Yao, D. Xiao, M. A. McGuire, K.-M. C. Fu, and X. Xu, "Valley manipulation by optically tuning the magnetic proximity effect in WSe$_2$/CrI$_3$ heterostructures," *Nano Lett.*, vol. 18, no. 6, pp. 3823–3828, 2018.

[41] K. F. Mak, K. He, J. Shan, and T. F. Heinz, "Control of valley polarization in monolayer MoS2 by optical helicity," *Nat. Nanotechnol.*, vol. 7, pp. 494–498, 2012.

[42] S. Tang, C. Zhang, C. Jia, H. Ryu, C. Hwang, M. Hashimoto, D. Lu, Z. Liu, T. P. Devereaux, Z.-X. Shen, and S.-K. Mo, "Electronic structure of monolayer 1T' -MoTe$_2$ grown by molecular beam epitaxy," *APL Mater.*, vol. 6, no. 2, pp. 026601, 2018.

[43] R. F. Frindt, "Single Crystals of MoS$_2$ Several Molecular Layers Thick," *J. Appl. Phys*, vol. 37, no. 4, 1966.

[44] K. S. Novoselov, D. Jiang, F. Schedin, T. J. Booth, V. V. Khotkevich, S. V. Morozov, and A. K. Geim, "Two-dimensional atomic crystals," *Proc. Natl Acad. Sci.*, vol. 102, 10451–10453, 2005.

[45] M. M. Benameur, B. Radisavljevic, J. S. Héron, S. Sahoo, H. Berger, and A. Kis, "Visibility of dichalcogenide nanolayers," *Nanotechnol.*, vol. 22, no. 12, 2011.

[46] M. Yi and Z. Shen, "A review on mechanical exfoliation for the scalable production of graphene," *J. Mater. Chem. A*, vol. 3, no. 22, pp. 11700–11715, 2015.

[47] E. Varrla, C. Backes, K. R. Paton, A. Harvey, Z. Gholamvand, J. McCauley, and J. N. Coleman, "Large-Scale Production of Size-Controlled MoS$_2$ Nanosheets by Shear Exfoliation," *Chem. Mater.*, vol. 27, no. 3, pp. 1129–1139, 2015.

[48] G. Eda, H. Yamaguchi, D. Voiry, T. Fujita, M. Chen, and M. Chhowalla, "Photoluminescence from chemically exfoliated MoS$_2$," *Nano Lett.*, vol. 11, no. 12, pp. 5111–5116, 2011.

[49] Z. Zeng, Z. Yin, X. Huang, H. Li, Q. He, G. Lu, F. Boey, and H. Zhang, "Single-layer semiconducting nanosheets: high-yield preparation and device fabrication," *Angew. Chem. Int. Ed.*, vol. 50, no. 47, pp. 11093–11097, 2011.

[50] J. Wu, H. Li, Z. Yin, H. Li, J. Liu, X. Cao, Q. Zhang, and H. Zhang, "Layer Thinning and Etching of Mechanically Exfoliated MoS$_2$ Nanosheets by Thermal Annealing in Air," *Small*, vol. 9, no. 19, pp. 3314–3319, 2013.

[51] M. Yamamoto, T. L. Einstein, M. S. Fuhrer, and W. G. Cullen, "Anisotropic Etching of Atomically Thin MoS$_2$," *J. Phys. Chem. C*, vol. 117, no. 48, pp. 25643–25649, 2013.

[52] X. Lu, M. I. B. Utama, J. Zhang, Y. Zhao, and Q. Xiong, "Layer-by-layer thinning of MoS_2 by thermal annealing," *Nanoscale*, vol. 5, no. 19, pp. 8904–8908, 2013.

[53] D. Dumcenco, D. Ovchinnikov, K. Marinov, P. Lazić, M. Gibertini, N. Marzari, O. L. Sanchez, Y.-C. Kung, D. Krasnozhon, M.-W. Chen, S. Bertolazzi, P. Gillet, A. F. i Morral, A. Radenovic, and A. Kis, "Large-area epitaxial monolayer MoS_2," *ACS Nano*, vol. 9, no. 4, pp. 4611–4620, 2015.

[54] O. Lehtinen, H.-P. Komsa, A. Pulkin, M. B. Whitwick, M.-W. Chen, T. Lehnert, M. J. Mohn, O. V. Yazyev, A. Kis, U. Kaiser, and A. V. Krasheninnikov, "Atomic scale microstructure and properties of Se-deficient two-dimensional $MoSe_2$," *ACS Nano*, vol. 9, no. 3, pp. 3274–3283, 2015.

[55] X. Wang, Y. Gong, G. Shi, W. L. Chow, K. Keyshar, G. Ye, R. Vajtai, J. Lou, Z. Liu, E. Ringe, B. K. Tay, and P. M. Ajayan, "Chemical Vapor Deposition Growth of Crystalline Monolayer $MoSe_2$," *ACS Nano*, vol. 8, no. 5, pp. 5125–5131, 2014.

[56] Y.-H. Lee, X.-Q. Zhang, W. Zhang, M.-T. Chang, C.-T. Lin, K. D. Chang, Y.-C. Yu, J. T.-W. Wang, C.-S. Chang, L.-J. Li, and T.-W. Lin, "Synthesis of Large-Area MoS_2 Atomic Layers with Chemical Vapor Deposition," *Adv. Mater.*, vol. 24, pp. 2320–2325, 2012.

[57] S. Najmaei, Z. Liu, W. Zhou, X. Zou, G. Shi, S. Lei, B. I. Yakobson, J.-C. Idrobo, P. M. Ajayan, and J. Lou, "Vapour phase growth and grain boundary structure of molybdenum disulphide atomic layers," *Nat. Mater.*, vol. 12, pp. 754–759, 2013.

[58] Y. Yu, C. Li, Y. Liu, L. Su, Y. Zhang, and L. Cao, "Controlled Scalable Synthesis of Uniform, High-Quality Monolayer and Few-layer MoS_2 Films," *Sci. Rep.*, vol. 3, 2013.

[59] S. Wang, Y. Rong, Y. Fan, M. Pacios, H. Bhaskaran, K. He, and J. H. Warner, "Shape Evolution of Monolayer MoS_2 Crystals Grown by Chemical Vapor Deposition," *Chem. Mater.*, vol. 26, no. 22, pp. 6371–6379, 2014.

[60] Y. Zhan, Z. Liu, S. Najmaei, P. M. Ajayan, and J. Lou, "Large-Area Vapor-Phase Growth and Characterization of MoS_2 Atomic Layers on a SiO_2 Substrate," *Small*, vol. 8, no. 7, pp. 966–971, 2012.

[61] J. Park, N. Choudhary, J. Smith, G. Lee, M. Kim, and W. Choi, "Thickness

modulated MoS$_2$ grown by chemical vapor deposition for transparent and flexible electronic devices," *Appl. Phys. Lett.*, vol. 106, 2015.

[62] G. H. Han, N. J. Kybert, C. H. Naylor, B. S. Lee, J. Ping, J. H. Park, J. Kang, S. Y. Lee, Y. H. Lee, R. Agarwal, and A. T. C. Johnson, "Seeded growth of highly crystalline molybdenum disulphide monolayers at controlled locations," *Nat. Commun.*, vol. 6, 2015.

[63] K. Kang, S. Xie, L. Huang, Y. Han, P. Y. Huang, K. F. Mak, C.-J. Kim, D. Muller, and J. Park, "High-mobility three-atom-thick semiconducting films with wafer-scale homogeneity," *Nature*, vol. 520, pp. 656–660, 2015.

[64] S. M. Eichfeld, L. Hossain, Y.-C. Lin, A. F. Piasecki, B. Kupp, A. G. Birdwell, R. A. Burke, N. Lu, X. Peng, J. Li, A. Azcatl, S. McDonnell, R. M. Wallace, M. J. Kim, T. S. Mayer, J. M. Redwing, and J. A. Robinson, "Highly Scalable, Atomically Thin WSe$_2$ Grown via Metal–Organic Chemical Vapor Deposition," *ACS Nano*, vol. 9, no. 2, pp. 2080–2087, 2015.

[65] L. K. Tan, B. Liu, J. H. Teng, S. Guo, H. Y. Lowd, and K. P. Loh, "Atomic layer deposition of a MoS$_2$ film," *Nanoscale*, vol. 6, no. 18, pp. 10584–10588, 2014.

[66] G. Ham, S. Shin, J. Park, H. Choi, J. Kim, Y.-A. Lee, H. Seo, and H. Jeon, "Tuning the Electronic Structure of Tin Sulfides Grown by Atomic Layer Deposition," *ACS Appl. Mater. Interfaces*, vol. 5, no. 18, pp. 8889−8896, 2013.

[67] Z. Jin, S. Shin, D. H. Kwon, S.-J. Hana, and Y.-S. Min, "Novel chemical route for atomic layer deposition of MoS$_2$ thin film on SiO$_2$/Si substrate," *Nanoscale*, vol. 6, no. 23, pp. 14453–14458, 2014.

[68] J.-G. Song, J. Park, W. Lee, T. Choi, H. Jung, C. W. Lee, S.-H. Hwang, J. M. Myoung, J.-H. Jung, S.-H. Kim, C. Lansalot-Matras, and H. Kim, "Layer-Controlled, Wafer-Scale, and Conformal Synthesis of Tungsten Disulfide Nanosheets Using Atomic Layer Deposition," *ACS Nano*, vol. 7, no. 12, pp. 11333–11340, 2013.

[69] R. Frisenda, E. Navarro-Moratalla, P. Gant, D. P. D. Lara, P. Jarillo-Herrero, R. V. Gorbachev, and A. Castellanos-Gomez, "Recent progress in the assembly of nanodevices and van der Waals heterostructures by deterministic placement of 2D materials," *Chem.*

Soc. Rev., vol. 47, no. 1, pp. 53–68, 2018.

[70] R. Dong and I. Kuljanishvili, "Review Article: Progress in fabrication of transition metal dichalcogenides heterostructure systems," *J. Vac. Sci. Technol. B*, vol. 35, no. 3, pp. 030803, 2017.

[71] P. Rivera, J. R. Schaibley, A. M. Jones, J. S. Ross, S. Wu, G. Aivazian, P. Klement, K. Seyler, G. Clark, N. J. Ghimire, J. Yan, D. G. Mandrus, W. Yao, and X. Xu, "Observation of long-lived interlayer excitons in monolayer $MoSe_2$–WSe_2 heterostructures," *Nat. Commun.*, vol. 6, 2015.

[72] K. Liu, Q. Yan, M. Chen, W. Fan, Y. Sun, J. Suh, D. Fu, S. Lee, J. Zhou, S. Tongay, J. Ji, J. B. Neaton, and J. Wu, "Elastic properties of chemical-vapor-deposited monolayer MoS_2, WS_2, and their bilayer heterostructures," *Nano Lett.*, vol. 14, no. 9, pp. 5097–103, 2014.

[73] A. Jain, P. Bharadwaj, S. Heeg, M. Parzefall, T. Taniguchi, K. Watanabe, and L. Novotny, "Minimizing residues and strain in 2D materials transferred from PDMS," *Nanotechnol.*, vol. 29, pp. 265203, 2018.

[74] M. A. Ibrahem, T.-W. Lan, J. K. Huang, Y.-Y. Chen, K.-H. Wei, L.-J. Li, and C. W. Chu, "High quantity and quality few-layers transition metal disulfide nanosheets from wet-milling exfoliation," *RSC Adv.*, vol. 3, pp. 13193–13202, 2013.

[75] M. Velický, G. E. Donnelly, W. R. Hendren, S. McFarland, D. Scullion, W. J. I. DeBenedetti, G. C. Correa, Y. Han, A. J. Wain, M. A. Hines, D. A. Muller, K. S. Novoselov, H. D. Abruña, R. M. Bowman, E. J. G. Santos, and F. Huang, "Mechanism of Gold-Assisted Exfoliation of Centimeter-Sized Transition-Metal Dichalcogenide Monolayers," *ACS Nano*, vol. 12, no. 10, 10463–10472, 2018.

[76] F. Liu, W. Wu, Y. Bai, S. H. Chae, Q. Li, J. Wang, J. Hone, and X.-Y. Zhu, "Disassembling 2D van der Waals crystals into macroscopic monolayers and reassembling into artificial lattices," *Science*, vol. 367, no. 6480, pp. 903–906, 2020.

[77] X.-Q. Zhang, C.-H. Lin, Y.-W. Tseng, K.-H. Huang, and Y.-H. Lee, "Synthesis of Lateral Heterostructures of Semiconducting Atomic Layers," *Nano Lett.*, vol. 15, no. 1, pp. 410–415, 2015.

[78] M. I. Serna, S. H. Yoo, S. Moreno, Y. Xi, J. P. Oviedo, H. Choi, H. N. Alshareef, M. J. Kim, M. Minary-Jolandan, and M. A. Quevedo-Lopez, "Large-Area Deposition of MoS$_2$ by Pulsed Laser Deposition with In Situ Thickness Control," *ACS Nano*, vol. 10, no. 6, pp. 6054–6061, 2016.

[79] K. M. McCreary, A. T. Hanbicki, S. Singh, R. K. Kawakami, G. G. Jernigan, M. Ishigami, A. Ng, T. H. Brintlinger, R. M. Stroud, and B. T. Jonker, "The Effect of Preparation Conditions on Raman and Photoluminescence of Monolayer WS$_2$," *Sci. Rep.*, vol. 6, 2016.

[80] K.-K. Liu, W. Zhang, Y.-H. Lee, Y.-C. Lin, M.-T. Chang, C.-Y. Su, C.-S. Chang, H. Li, Y. Shi, H. Zhang, C.-S. Lai, and L.-J. Li, "Growth of Large-Area and Highly Crystalline MoS$_2$ Thin Layers on Insulating Substrates," *Nano Lett.*, vol. 12, no. 3, pp. 1538–1544, 2012.

[81] Y.-C. Lin, W. Zhang, J.-K. Huang, K.-K. Liu, Y.-H. Lee, C.-T. Liang, C.-W. Chu, and L.-J. Li, "Wafer-scale MoS$_2$ thin layers prepared by MoO$_3$ sulfurization," *Nanoscale*, vol. 4, no. 20, pp. 6637–6641, 2012.

[82] A. Gurarslan, Y. Yu, L. Su, Y. Yu, F. Suarez, S. Yao, Y. Zhu, M. Ozturk, Y. Zhang, and L. Cao, "Surface-Energy-Assisted Perfect Transfer of Centimeter-Scale Monolayer and Few-Layer MoS$_2$ Films onto Arbitrary Substrates," *ACS Nano*, vol. 8, no. 11, 11522–11528, 2014.

[83] K. Kaasbjerg, K. S. Thygesen, and K. W. Jacobsen, "Phonon-limited mobility in n-type single-layer MoS$_2$ from first principles," *Phys. Rev. B*, vol. 85, no. 11, 2012.

[84] X. Li, J. T. Mullen, Z. Jin, K. M. Borysenko, M. B. Nardelli, and K. W. Kim, "Intrinsic electrical transport properties of monolayer silicene and MoS$_2$ from first principles," *Phys. Rev. B*, vol. 87, no. 11, 2013.

[85] N. Ma and D. Jena, "Charge Scattering and Mobility in Atomically Thin Semiconductors," *Phys. Rev. X*, vol. 4, 2014.

[86] S. Das, H.-Y. Chen, A. V. Penumatcha, and J. Appenzeller, "High Performance Multilayer MoS$_2$ Transistors with Scandium Contacts," *Nano Lett.*, vol. 13, no. 1, pp. 100–105, 2013.

[87] H. Peelaers and C. G. Van de Walle, "Effects of strain on band structure and effective masses in MoS_2," *Phys. Rev. B*, vol. 86, no. 24, 2012.

[88] P. M. Solomon, S.E. Laux, L. Shi, J. Cai, and W. Haensch, "Experimental and theoretical explanation for the orientation dependence gate-induced drain leakage in scaled MOSFETs," In *Device Research Conference (DRC), 2009 IEEE International*. IEEE, 2009.

[89] B. Keeth and R. J. Baker. *DRAM Circuit Design: Fundamental and High-Speed Topics*. Wiley-Interscience, 2008. Online ISBN: 9780470184752.

[90] Y. Zhu, L. Peng, Z. Fang, C. Yan, X. Zhang, and G. Yu, "Structural Engineering of 2D Nanomaterials for Energy Storage and Catalysis," *Adv. Mater.*, vol. 30, no. 15, 2018.

[91] M. Acerce, D. Voiry, and M. Chhowalla, "Metallic 1T Phase MoS_2 Nanosheets as Supercapacitor Electrode Materials," *Nat. Nanotechnol.*, vol. 10, no. 4, 2015.

[92] K. Chang and W. Chen, "*In situ* synthesis of MoS_2/graphenenanosheet composites with extraordinarily high electrochemical performance for lithium ion batteries," *Chem. Commun.*, vol. 47, pp. 4252–4254, 2011.

[93] A. Castellanos-Gomez, M. Poot, G. A. Steele, H. S. J. van der Zant, N. Agrait, G. Rubio-Bollinger, "Elastic Properties of Freely Suspended MoS_2 Nanosheets," *Adv. Mater.*, vol. 24, no. 6, pp. 772–775, 2012.

[94] H.-Y. Chang, M. Nagavalli, Y. Rudresh, G. Amritesh, R. A. Sanne, S. Yang, N. Lu, S. K. Banerjee, and D. Akinwande, "Large-Area Monolayer MoS_2 for Flexible Low-Power RF Nanoelectronics in the GHz Regime," *Adv. Mater.*, vol. 28, no. 9, pp. 1818–1823, 2016.

[95] R. Kappera, D. Voiry, S. E. Yalcin, B. Branch, G. Gupta, A. D. Mohite, and M. Chhowalla, "Phase-engineered low-resistance contacts for ultrathin MoS_2 transistors," *Nat. Mater.*, vol. 13, pp. 1128–1134, 2014.

[96] R. Landauer, "Spatial Variation of Currents and Fields Due to Localized Scatterers in Metallic Conduction", *IBM J. Res. Dev.*, vol. 1, no. 3, pp. 223–231, 1957.

[97] Y. V. Sharvin, "A Possible Method for Studying Fermi Surfaces," *Sov. Phys. JETP*,

vol. 21, no. 3, pp. 655–656, 1965.

[98] D. Jena, K. Banerjee, and G. H. Xing, "Intimate contacts," *Nat. Mater.*, vol. 13, pp. 1076–1078, 2014.

[99] ITRS 2.0 Home Page. http://www.itrs2.net/.

[100] L. Wang, I. Meric1, P. Y. Huang, Q. Gao, Y. Gao, H. Tran, T. Taniguchi, K. Watanabe, L. M. Campos, D. A. Muller, J. Guo, P. Kim, J. Hone, K. L. Shepard, and C. R. Dean, "One-dimensional electrical contact to a two-dimensional material," *Science*, vol. 342, no. 6158, pp. 614–617, 2013.

[101] J. Kang, W. Liu, D. Sarkar, D. Jena, and K. Banerjee, "Computational study of metal contacts to monolayer transition-metal dichalcogenide semiconductors," *Phys. Rev. X*, vol. 4, no. 3, pp. 031005, 2014.

[102] Y. Matsuda, W.-Q. Deng, and W. A. Goddard, "Contact resistance for 'endcontacted' metal−graphene and metal−nanotube interfaces from quantum mechanics," *J. Phys. Chem. C*, vol. 114, no. 41, pp. 17845–17850, 2010.

[103] J. Kang, D. Sarkar, W. Liu, D. Jena, and K. Banerjee, "A computational study of metal-contacts to beyond-graphene 2D semiconductor materials," *IEEE Int. Electron Dev. Meet.*, pp. 407–410, 2012.

[104] W. Liu, J. Kang, W. Cao, D. Sarkar, Y. Khatami, D. Jena, and K. Banerjee, "High-performance few-layer-MoS$_2$ field-effect-transistor with record low contact-resistance," *IEEE Int. Electron Dev. Meet.*, pp. 19.4.1–19.4.4, 2013.

[105] F. Giannazzo, G. Fisichella, A. Piazza, S. Di Franco, G. Greco, S. Agnello, and F. Roccaforte, "Impact of contact resistance on the electrical properties of MoS$_2$ transistors at practical operating temperatures," *Beilstein J. Nanotechnol.*, vol. 8, pp. 254–263, 2017.

[106] W. Liu, D. Sarkar, J. Kang, W. Cao, and K. Banerjee, "Impact of Contact on the Operation and Performance of Back-Gated Monolayer MoS$_2$ Field-Effect-Transistors," *ACS Nano*, vol. 9, no. 8, pp. 7904–7912, 2015.

[107] C. Gong, L. Colombo, R. M. Wallace, and K. Cho, "The unusual mechanism of partial Fermi level pinning at metal–MoS$_2$ interfaces," *Nano Lett.*, vol. 14, no. 4, pp.

1714–1720, 2014.

[108] C. Kim, I. Moon, D. Lee, M. S. Choi, F. Ahmed, S. Nam, Y. Cho, H.-J. Shin, S. Park, and W. J. Yoo, "Fermi Level Pinning at Electrical Metal Contacts of Monolayer Molybdenum Dichalcogenides," *ACS Nano*, vol. 11, no. 2, pp. 1588–1596, 2017.

[109] A. Allain, J. Kang, K. Banerjee, and A. Kis, "Electrical contacts to two-dimensional semiconductors," *Nat. Mater.*, vol. 14, pp. 1195–1205, 2015.

[110] Y. Taur and T. H. Ning. *Fundamentals of Modern VLSI Devices*. Cambridge University Press: Cambridge, UK, 2013. Online ISBN: 9781107635715.

[111] H. Yuan, G. Cheng, S. Yu, A. R. H. Walker, C. A. Richter, M. Pan, and Q. Li, "Field effects of current crowding in metal-MoS_2 contacts," *Appl. Phys. Lett.*, vol. 108, no. 10, 2016.

[112] Y. Guo, Y. Han, J. Li, A. Xiang, X. Wei, S. Gao, and Q. Chen, "Study on the Resistance Distribution at the Contact between Molybdenum Disulfide and Metals," *ACS Nano*, vol. 8, no. 8, pp. 7771–7779, 2014.

[113] Y. Xu, C. Cheng, S. Du, J. Yang, B. Yu, J. Luo, W. Yin, E. Li, S. Dong, P. Ye, and X. Duan, "Contacts between Two- and Three-Dimensional Materials: Ohmic, Schottky, and p–n Heterojunctions," *ACS Nano*, vol. 10, no. 5, pp. 4895–4919, 2016.

[114] J.-R. Chen, P. M. Odenthal, A. G. Swartz, G. C. Floyd, H. Wen, K. Y. Luo, and R. K. Kawakami, "Control of Schottky Barriers in Single Layer MoS_2 Transistors with Ferromagnetic Contacts," *Nano Lett.*, vol. 13, no. 7, pp. 3106–3110, 2013.

[115] H. Qiu, L. Pan, Z. Yao, J. Li, Y. Shi, and X. Wang, "Electrical characterization of back-gated bi-layer MoS_2 field-effect transistors and the effect of ambient on their performances," *Appl. Phys. Lett.*, vol. 100, no. 12, 2012.

[116] A. Dankert, L. Langouche, M. V. Kamalakar, and S. P. Dash, "High-Performance Molybdenum Disulfide Field-Effect Transistors with Spin Tunnel Contacts," *ACS Nano*, vol. 8, no. 1, pp. 476–482, 2014.

[117] W. Wang, Y. Liu, L. Tang, Y. Jin, T. Zhao, and F. Xiu, "Controllable Schottky Barriers between MoS_2 and Permalloy," *Sci. Rep.*, vol. 4, 2014.

[118] S. M. Sze and K. K. Ng. *Physics of Semiconductor Devices*. John Wiley & Sons, 2006. Online ISBN: 9780470068328.

[119] A. Anwar, B. Nabet, J. Culp, and F. Castro, "Effects of electron confinement on thermionic emission current in a modulation doped heterostructure," *J. Appl. Phys.*, vol. 85, no. 5, 1999.

[120] H.-J. Chuang, X. Tan, N. J. Ghimire, M. M. Perera, B. Chamlagain, M. M.-C. Cheng, J. Yan, D. Mandrus, D. Tománek, and Z. Zhou, "High Mobility WSe_2 p- and n-Type Field-Effect Transistors Contacted by Highly Doped Graphene for Low-Resistance Contacts," *Nano Lett.*, vol. 14, no. 6, pp. 3594–3601, 2014.

[121] H. Liu, A. T. Neal, Z. Zhu, Z. Luo, X. Xu, D. Tománek, and P. D. Ye, "Phosphorene: An unexplored 2D semiconductor with a high hole mobility," *ACS Nano*, vol. 8, no. 4, pp. 4033–4041, 2014.

[122] J. R. Lince, D. J. Carré, and P. D. Fleischauer, "Schottky-barrier Formation on a Covalent Semiconductor Without Fermi-level Pinning: The metal-MoS_2(0001) Interface," *Phys. Rev. B*, vol. 36, no. 3, pp. 1647–1656, 1987.

[123] W. Jaegermann, C. Pettenkofer, and B. A. Parkinson, "Cu and Ag deposition on layered p-type WSe_2: Approaching the Schottky limit," *Phys. Rev. B*, vol. 42, no. 12, pp. 7487–7496, 1990.

[124] R. Schlaf, A. Klein, C. Pettenkofer, and W. Jaegermann, "W. Laterally inhomogeneous surface-potential distribution and photovoltage at clustered In/WSe_2(0001) interfaces," *Phys. Rev. B*, vol. 48, no. 19, pp. 14242–14252, 1993.

[125] A. Kleina, C. Pettenkofera, W. Jaegermanna, M. Lux-Steinerb, and E. Bucher, "A photoemission study of barrier and transport properties of the interfaces of Au and Cu with WSe_2(0001) surfaces," *Surf. Sci.*, vol. 321, no. 1–2, pp. 19–31, 1994.

[126] R. T. Tung, "The physics and chemistry of the Schottky barrier height," *Appl. Phys. Rev.*, vol. 1, no. 1, 2014.

[127] L. Porte, C. H. de Villeneuve, and M. Phaner, "Scanning tunneling microscopy observation of local damages induced on graphite surface by ion implantation," *J. Vac. Sci. Technol. B Microelectron. Nanometer Struct. Process. Meas. Phenom.*, vol. 9, pp.

1064–1067, 1991.

[128] O. W. Holland, B. R. Appleton, and J. Narayan, "Ion implantation damage and annealing in germanium," *J. Appl. Phys.*, vol. 54, no. 5, pp. 2295–2301, 1983.

[129] S. J. Pearton, A. R. Von Neida, J. M. Brown, K. T. Short, L. J. Oster, and U. K. Chakrabarti, "Ion implantation damage and annealing in InAs, GaSb, and GaP," *J. Appl. Phys.*, vol. 64, no. 2, pp. 629–636, 1988.

[130] J. Narayan and O. W. Holland, "Characteristics of Ion-Implantation Damage and Annealing Phenomena in Semiconductors," *J. Electrochem. Soc.*, vol. 131, pp. 2651–2662, 1984.

[131] R. E. Hummel, Wei Xi, P. H. Holloway, and K. A. Jones, "Optical investigations of ion implant damage in silicon," *J. Appl. Phys.*, vol. 63, no. 8, pp. 2591–2594, 1988.

[132] M. R. Laskar, D. N. Nath, L. Ma, E. W. Lee II, C. H. Lee, T. Kent, Z. Yang, R. Mishra, M. A. Roldan, J.-C. Idrobo, S. T. Pantelides, S. J. Pennycook, R. C. Myers, Y. Wu, and S. Rajan, "p-type doping of MoS$_2$ thin films using Nb," *Appl. Phys. Lett.*, vol. 104, no. 9, 2014.

[133] J. Suh, T.-E. Park, D.-Y. Lin, D. Fu, J. Park, H. J. Jung, Y. Chen, C. Ko, C. Jang, Y. Sun, R. Sinclair, J. Chang, S. Tongay, and J. Wu, "Doping Against the Native Propensity of MoS$_2$: Degenerate Hole Doping by Cation Substitution," *Nano Lett.*, vol. 14, no. 12, pp. 6976–6982, 2014.

[134] S. Das, M. Demarteau, and A. Roelofs, "Nb-doped single crystalline MoS$_2$ field effect transistor," *Appl. Phys. Lett.*, vol. 106, no. 17, 2015.

[135] G. Mirabelli, M. Schmidt, B. Sheehan, K. Cherkaoui, S. Monaghan, I. Povey, M. McCarthy, A. P. Bell, R. Nagle, F. Crupi, P. K. Hurley, and R. Duffy, "Back-gated Nb-doped MoS$_2$ junctionless field-effect-transistors," *AIP Adv.*, vol. 6, no. 2, 2016.

[136] H.-J. Chuang, B. Chamlagain, M. Koehler, M. M. Perera, J. Yan, D. Mandrus, D. Tománek, and Z. Zhou, "Low-Resistance 2D/2D Ohmic Contacts: A Universal Approach to High-Performance WSe$_2$, MoS$_2$, and MoSe$_2$ Transistors," *Nano Lett.*, vol. 16, no. 3, pp. 1896–1902, 2016.

[137] T. Hallam, S. Monaghan, F. Gity, L. Ansari, M. Schmidt, C. Downing, C. P. Cullen, V. Nicolosi, P. K. Hurley, and G. S. Duesberg, "Rhenium-doped MoS$_2$ films," *Appl. Phys. Lett.*, vol. 111, no. 20, 2017.

[138] L. Yang, K. Majumdar, H. Liu, Y. Du, H. Wu, M. Hatzistergos, P. Y. Hung, R. Tieckelmann, W. Tsai, C. Hobbs, and P. D. Ye, "Chloride Molecular Doping Technique on 2D Materials: WS$_2$ and MoS$_2$," *Nano Lett.*, vol. 14, no. 11, pp. 6275–6280, 2014.

[139] S. Qin, W. Lei, D. Liu, and Y. Chen, "In-situ and tunable nitrogen-doping of MoS$_2$ nanosheets," *Sci. Rep.*, vol. 4, 2014.

[140] A. Azcatl, X. Qin, A. Prakash, C. Zhang, L. Cheng, Q. Wang, N. Lu, M. J. Kim, J. Kim, K. Cho, R. Addou, C. L. Hinkle, J. Appenzeller, and R. M. Wallace, "Covalent Nitrogen Doping and Compressive Strain in MoS$_2$ by Remote N$_2$ Plasma Exposure," *Nano Lett.*, vol. 16, no. 9, pp. 5437–5443, 2016.

[141] D. Kiriya, M. Tosun, P. Zhao, J. S. Kang, and A. Javey, "Air-Stable Surface Charge Transfer Doping of MoS$_2$ by Benzyl Viologen," *J. Am. Chem. Soc.*, vol. 136, no. 22, pp. 7853–7856, 2014.

[142] A. Rai, A. Valsaraj, H. C.P. Movva, A. Roy, R. Ghosh, S. Sonde, S. Kang, J. Chang, T. Trivedi, R. Dey, S. Guchhait, S. Larentis, L. F. Register, E. Tutuc, and S. K. Banerjee, "Air stable doping and intrinsic mobility enhancement in monolayer molybdenum disulfide by amorphous titanium suboxide encapsulation," *Nano Lett.*, vol. 15, no. 7, pp. 4329–4336, 2015.

[143] S. Chuang, C. Battaglia, A. Azcatl, S. McDonnell, J. S. Kang, X. Yin, M. Tosun, R. Kapadia, H. Fang, R. M. Wallace, and A. Javey, "MoS$_2$ P-type Transistors and Diodes Enabled by High Work Function MoO$_x$ Contacts," *Nano Lett.*, vol. 14, no. 3, pp. 1337–1342, 2014.

[144] A. Alharbi and D. Shahrjerdi, "Contact engineering of monolayer CVD MoS$_2$ transistors," In *Device Research Conference (DRC), 2017 IEEE International*. IEEE, 2017.

[145] C. J. McClellan, E. Yalon; K. K. H. Smithe, S. V. Suryavanshi, E. Pop, "Effective n-type doping of monolayer MoS$_2$ by AlO$_x$," In *Device Research Conference (DRC),*

2017 IEEE International. IEEE, 2017.

[146] C. J. L. de la Rosa, A. Nourbakhsh, M. Heyne, I. Asselberghs, C. Huyghebaert, I. Radu, M. Heynsa, and S. De Gendtac , "Highly efficient and stable MoS$_2$ FETs with reversible n-doping using a dehydrated poly(vinyl-alcohol) coating," *Nanoscale*, vol. 9, no. 1, pp. 258–265, 2017.

[147] X. Liu, D. Qu, J. Ryu, F. Ahmed, Z. Yang, D. Lee, and W. J. Yoo, "P-Type Polar Transition of Chemically Doped Multilayer MoS$_2$ Transistor," *Adv. Mater.*, vol. 28, no. 12, 2345–2351, 2016.

[148] S.-W. Min, M. Yoon, S. J. Yang, K. R. Ko, and S. Im, "Charge-Transfer-Induced p-Type Channel in MoS$_2$ Flake Field Effect Transistors," *ACS Appl. Mater. Interfaces*, vol. 10, no. 4, pp. 4206–4212, 2018.

[149] Y. Zhang, J. Ye, Y. Matsuhashi, and Y. Iwasa, "Ambipolar MoS$_2$ Thin Flake Transistors," *Nano Lett.*, vol. 12, no. 3, pp. 1136–1140, 2012.

[150] M.-W. Lin, L. Liu, Q. Lan, X. Tan, K. S. Dhindsa, P. Zeng, V. M. Naik, M. M.-C. Cheng, and Z. Zhou, "Mobility enhancement and highly efficient gating of monolayer MoS$_2$ transistors with polymer electrolyte," *J. Phys. Appl. Phys.*, vol. 45, 2012.

[151] M. M. Perera, M.-W. Lin, H.-J. Chuang, B. P. Chamlagain, C. Wang, X. Tan, M. M.-C. Cheng, D. Tománek, and Z. Zhou, "Improved Carrier Mobility in Few-Layer MoS$_2$ Field-Effect Transistors with Ionic-Liquid Gating," *ACS Nano*, vol. 7, no. 5, pp. 4449–4458, 2013.

[152] J. Jiang, M. A. Kuroda, A. C. Ahyi, T. Isaacs-Smith, V. Mirkhani, M. Park, and S. Dhar, "Chitosan solid electrolyte as electric double layer in multilayer MoS$_2$ transistor for low-voltage operation," *Phys. Status Solidi A*, vol. 212, pp. 2219–2225, 2015.

[153] S. KC, R. C Longo, R. Addou, R. M Wallace, and K. Cho, "Impact of intrinsic atomic defects on the electronic structure of MoS$_2$ monolayers," *Nanotechnology*, vol. 25, 2014.

[154] Y. Han, Z. Wu, S. Xu, X. Chen, L. Wang, Y. Wang, W. Xiong, T. Han, W. Ye, J. Lin, Y. Cai, K. M. Ho, Y. He, D. Su, and N. Wang, "Probing Defect-Induced Midgap States in MoS$_2$ Through Graphene–MoS$_2$ Heterostructures," *Adv. Mater. Interfaces*, vol.

2, no. 8, 2015.

[155] C.-P. Lu, G. Li, J. Mao, L.-M. Wang, and E. Y. Andrei, "Bandgap, Mid-Gap States, and Gating Effects in MoS_2," *Nano Lett.*, vol. 14, no. 8, pp. 4628–4633, 2014

[156] Y. Guo, D. Liu, and J. Robertson, "3D Behavior of Schottky Barriers of 2D Transition-Metal Dichalcogenides," *ACS Appl. Mater. Interfaces*, vol. 7, no. 46, pp. 25709–25715, 2015.

[157] R. J. Wu, S. Udyavara, R. Ma, Y. Wang, M. Chhowalla, T. Birol, S. J. Koester, M. Neurock, and K. A. Mkhoyan, "Visualizing the metal-MoS_2 contacts in two-dimensional field-effect transistors with atomic resolution," *Phys. Rev. Mater.*, vol. 3, no. 11, pp. 111001, 2019.

[158] M. Farmanbar and G. Brocks, "First-principles study of van der Waals interactions and lattice mismatch at MoS_2/metal interfaces," *Phys. Rev. B*, vol. 93, 2016.

[159] Y. Du, L. Yang, J. Zhang, H. Liu, K. Majumdar, P. D. Kirsch, and P. D. Ye, "MoS_2 Field-Effect Transistors With Graphene/Metal Heterocontacts," *IEEE Elect. Dev. Lett.*, vol. 35, no. 5, pp. 599−601, 2014.

[160] W. S. Leong, X. Luo, Y. Li, K. H. Khoo, S. Y. Quek, and J. T. L. Thong, "Low Resistance Metal Contacts to MoS_2 Devices with Nickel-Etched-Graphene Electrodes," *ACS Nano*, vol. 9, no. 1, pp. 869–877, 2014.

[161] J. Wang, Q. Yao, C.-W. Huang, X. Zou, L. Liao, S. Chen, Z. Fan, K. Zhang, W. Wu, X, Xiao, C. Jiang, and W.-W. Wu, "High Mobility MoS_2 Transistor with Low Schottky Barrier Contact by Using Atomic Thick h-BN as a Tunneling Layer," *Adv. Mater.*, vol. 28, no. 37, pp. 8302–8308, 2016.

[162] W. Park, Y. Kim, S. K. Lee, U. Jung, J. H. Yang, C. Cho, Y. J. Kim, S. K. Lim, I. S. Hwang, H.-B.-R. Lee, and B. H. Lee, "Contact resistance reduction using Fermi level de-pinning layer for MoS_2 FETs," In *Electron Devices Meeting (IEDM), 2014 IEEE International*. IEEE, 2014.

[163] N. Kaushik, A. Nipane, S. Karande, and S. Lodha, "Contact resistance reduction in MoS_2 FETs using ultra-thin TiO_2 interfacial layers" In *Device Research Conference (DRC), 2015 IEEE International*. IEEE, 2015.

[164] N. Kaushik, D. Karmakar, A. Nipane, S. Karande, and S. Lodha, "Interfacial n-Doping Using an Ultrathin TiO_2 Layer for Contact Resistance Reduction in MoS_2," *ACS Appl. Mater. Interfaces*, vol. 8, no. 1, pp. 256–263, 2016.

[165] S. Lee, A. Tang, S. Aloni, and H.-S. P. Wong, "Statistical Study on the Schottky Barrier Reduction of Tunneling Contacts to CVD Synthesized MoS_2," *Nano Lett.*, vol. 16, no. 1, pp. 276–281, 2016.

[166] D. Connelly, C. Faulkner, P. A. Clifton, and D. E. Grupp, "Fermi-level depinning for low-barrier Schottky source/drain transistors," *Appl. Phys. Lett.*, vol. 88, no. 1, 2006.

[167] A. M. Roy, J. Y. J. Lin, and K. C. Saraswat, "Specific Contact Resistivity of Tunnel Barrier Contacts Used for Fermi Level Depinning," *IEEE Electron Device Lett.*, vol. 31, no. 10, pp. 1077–1079, 2010.

[168] Y. Wang, J. C. Kim, R. J. Wu, J. Martinez, X. Song, J. Yang, F. Zhao, A. Mkhoyan, H. Y. Jeong, and M. Chhowalla, "Van der Waals contacts between three-dimensional metals and two-dimensional semiconductors," *Nature*, vol. 568, 2019.

[169] C. Kim, K. Y. Lee, I. Moon, S. Issarapanacheewin, and W. J. Yoo, "Metallic contact induced van der Waals gap in a MoS_2 FET," *Nanoscale*, vol. 11, pp. 18246–18254, 2019.

[170] J. Kang, W. Liu, and K. Banerjee, "High-performance MoS_2 transistors with low-resistance molybdenum contacts," *Appl. Phys. Lett.*, vol. 104, no. 9, 2014.

[171] I. Popov, G. Seifert, and D. Tománek, "Designing electrical contacts to MoS_2 monolayers: a computational study," *Phys. Rev. Lett.*, vol. 108, no. 15, 2012

[172] Y. Khatami, H. Li, C. Xu, and K. Banerjee, "Metal-to-Multilayer-Graphene Contact—Part I: Contact Resistance Modeling," *IEEE Trans. Electron Devices*, vol. 59, no. 9, pp. 2444–2452, 2012.

[173] Y. Khatami, H. Li, C. Xu, and K. Banerjee, "Metal-to-Multilayer-Graphene Contact—Part II: Analysis of Contact Resistance," *IEEE Trans. Electron Devices*, vol. 59, no. 9, pp. 2453–2460, 2012.

[174] S. Cho, S. Kim, J. H. Kim, J. Zhao, J. Seok, D. H. Keum, J. Baik, D.-H. Choe, K. J.

Chang, K. Suenaga, S. W. Kim, Y. H. Lee, and H. Yang, "Phase patterning for ohmic homojunction contact in MoTe$_2$," *Science*, vol. 349, no. 6248, pp. 625–628, 2015.

[175] D. K. Schroder. *Semiconductor Material and Device Characterization*. John Wiley & Sons, 2006. Online ISBN: 9780471749097.

[176] Y. S. Chieh, A. K. Perera, and J. P. Krusius, "Series resistance of silicided ohmic contacts for nanoelectronics," *IEEE Trans. Electron. Dev.*, vol. 39, no. 8, pp. 1882–1888, 1992.

[177] H. Liu, M. Si, Y. Deng, A. T. Neal, Y. Du, S. Najmaei, P. M. Ajayan, J. Lou, and P. D. Ye, "Switching mechanism in single-layer molybdenum disulfide transistors: An insight into current flow across Schottky barriers," *ACS Nano*, vol. 8, no. 1, pp. 1031–1038, 2014.

[178] K. L. Grosse, M.-H. Bae, F. Lian, E. Pop, and W. P. King, "Nanoscale Joule heating, Peltier cooling and current crowding at graphene–metal contacts," *Nat. Nanotechnol.*, vol. 6, pp. 287–290, 2011.

[179] D. B. Scott, W. R. Hunter, and H. Shichijo, "A Transmission Line Model for Silicided Diffusions: Impact on the Performance of VLSI Circuits," *IEEE J. Solid-State Circuits*, vol. 17, no. 2, pp. 281–291, 1982.

[180] H. H. Berger, "Models for contacts to planar devices," *Solid State Electron.*, vol. 15, no. 2, pp. 145–158, 1972.

[181] F. Xia, V. Perebeinos, Y.-M. Lin, Y. Wu, and P. Avouris, "The origins and limits of metal–graphene junction resistance," *Nat. Nanotechnol.*, vol. 6, no.3, pp. 179–184, 2011.

[182] K. Nagashio, T. Nishimura, K. Kita and A. Toriumi, "Metal/graphene contact as a performance killer of ultra-high mobility graphene analysis of intrinsic mobility and contact resistance," In *Electron Devices Meeting (IEDM), 2009 IEEE International*. IEEE, 2009.

[183] S. Russoab, M. F. Craciuna, M. Yamamotoa, A. F. Morpurgoc, and S. Tarucha, "Contact resistance in graphene-based devices," *Physica E*, vol. 42, no. 4, pp. 677–679, 2010.

[184] X.-L. Fan, Y. Yang, P. Xiao and W.-M. Lau, "Site-specific catalytic activity in exfoliated MoS_2 single-layer polytypes for hydrogen evolution: basal plane and edges," *J. Mater. Chem. A*, vol. 2, pp. 20545–20551, 2014.

[185] D. Voiry, H. Yamaguchi, J. Li, R. Silva, D. C. Alves, T. Fujita, M. Chen, T. Asefa, V. B. Shenoy and G. Eda, "Enhanced Catalytic Activity in Strained Chemically Exfoliated WS_2 Nanosheets for Hydrogen Evolution," *Nat. Mater.*, vol. 12, pp. 850–855, 2013.

[186] H. Wang, Z. Lu, S. Xu, D. Kong, J. J. Cha, G. Zheng, P.-C. Hsu, K. Yan, D. Bradshaw, F. B. Prinz, and Y. Cui, "Electrochemical tuning of vertically aligned MoS_2 nanofilms and its application in improving hydrogen evolution reaction," *PNAS*, vol. 110, no. 49, pp. 19701–19706, 2013.

[187] Y. Zhou, Y. Liu, W. Zhao, R. Xu, D. Wang, B. Li, X. Zhou and H. Shen, "Rational design and synthesis of 3D MoS_2 hierarchitecture with tunable nanosheets and 2H/1T phase within graphene for superior lithium storage," *Electrochim. Acta*, vol. 211, pp. 1048–1055, 2016.

[188] Y. Xia, B. Wang, X. Zhao, G. Wang and H. Wang, "Core-shell composite of hierarchical MoS_2 nanosheets supported on graphitized hollow carbon microspheres for high performance lithium-ion batteries" *Electrochim. Acta*, vol. 187, pp. 55–64, 2016.

[189] W. Tang, Z. Chen, B. Tian, H.-W. Lee, X. Zhao, X. Fan, Y. Fan, K. Leng, C. Peng and M.-H. Kim, "*In Situ* Observation and Electrochemical Study of Encapsulated Sulfur Nanoparticles by MoS_2 Flakes," *J. Am. Chem. Soc.*, vol. 139, no. 29, pp. 10133–10141, 2017.

[190] H. Yamaguchi, J.-C. Blancon , R. Kappera , S. Lei , S. Najmaei , B. D. Mangum , G. Gupta , P. M. Ajayan , J. Lou and M. Chhowalla, "Spatially Resolved Photoexcited Charge-Carrier Dynamics in Phase-Engineered Monolayer MoS_2," *ACS Nano*, vol. 9, no. 1, pp. 840–849, 2015.

[191] H. L. Zhuang, M. D. Johannes, A. K. Singh, and R. G. Hennig, "Doping-controlled phase transitions in single-layer MoS_2," *Phys. Rev. B*, vol. 96, no. 16, 2017.

[192] Y. Li, K.-A. N. Duerloo, K. Wauson, and E. J. Reed, "Structural semiconductor-to-

semimetal phase transition in two-dimensional materials induced by electrostatic gating," *Nat. Commun.*, vol. 7, 2016.

[193] H. Yang, S. W. Kim, M. Chhowalla, and Y. H. Lee, "Structural and quantum-state phase transitions in van der Waals layered materials," *Nat. Phys.*, vol. 13, pp. 931–937, 2017.

[194] Y. Wang, J. Xiao, H. Zhu, Y. Li, Y. Alsaid, K. Y. Fong, Y. Zhou, S. Wang, W. Shi, Y. Wang, A. Zettl, E. J. Reed, and X. Zhang, "Structural phase transition in monolayer $MoTe_2$ driven by electrostatic doping," *Nature*, vol. 550, pp. 487–491, 2017.

[195] H. T. Yuan, M. Toh, K. Morimoto, W. Tan, F. Wei, H. Shimotani, Ch. Kloc, and Y. Iwasa, "Liquid-gated electric-double-layer transistor on layered metal dichalcogenide, SnS_2," *Appl. Phys. Lett.*, vol. 98, no. 1, 2011.

[196] J. T. Ye, Y. J. Zhang, R. Akashi, M. S. Bahramy, R. Arita, Y. Iwasa, "Superconducting Dome in a Gate-Tuned Band Insulator," *Science*, vol. 338, no. 6111, pp. 1193–1196, 2012.

[197] T. Fujimotoa, and K. Awaga, "Electric-double-layer field-effect transistors with ionic liquids," *Phys. Chem. Chem. Phys.*, vol. 15, pp. 8983–9006, 2013.

[198] S. Fan, X. Zou, H. Du, L. Gan, C. Xu, W. Lv, Y. He, Q. Yang, F. Kang, and J. Li, "Theoretical Investigation of the Intercalation Chemistry of Lithium/Sodium Ions in Transition Metal Dichalcogenides," *J. Phys. Chem. C*, vol. 121, pp. 13599−13605, 2017.

[199] L. Zhou, K. Xu, A. Zubair, A. D. Liao, W. Fang, F. Ouyang, Y. H. Lee, K. Ueno, R. Saito, T. Palacios, J. Kong, M. S. Dresselhaus, "Large-Area Synthesis of High-Quality Uniform Few-Layer $MoTe_2$," *J. Am. Chem. Soc.*, vol. 137, no. 37, 2015.

[200] S. Kim, J. H. Kim, D. Kim, G. Hwang, J. Baik, H. Yang, and S. Cho, "Post-patterning of an electronic homojunction in atomically thin monoclinic $MoTe_2$," *2D Mater.*, vol. 4, no. 2, 2017.

[201] S. Song, D. H. Keum, S. Cho, D. Perello, Y. Kim, and Y. H. Lee, "Room temperature semiconductor–metal transition of $MoTe_2$ thin films engineered by strain," *Nano Lett.*, vol. 16, no. 1, pp. 188–193, 2016.

[202] S. W. Wang, H. Medina, K. B. Hong, C. C. Wu, Y. Qu, A. Manikandan, T. Y. Su, P. T. Lee, Z. Q. Huang, Z. Wang, F. C. Chuang, H. C. Kuo, and Y. L. Chueh, "Thermally Strained Band Gap Engineering of Transition-Metal Dichalcogenide Bilayers with Enhanced Light–Matter Interaction toward Excellent Photodetectors," *ACS Nano*, vol. 11, no. 9, pp. 8768–8776, 2017.

[203] A. P. Nayak, T. Pandey, D. Voiry, J. Liu, S. T. Moran, A. Sharma, C. Tan, C.-H. Chen, L.-J. Li, M. Chhowalla, J.-F. Lin, A. K. Singh, and D. Akinwande, "Pressure-Dependent Optical and Vibrational Properties of Monolayer Molybdenum Disulfide," *Nano Lett.*, vol. 15, no. 1, pp. 346–353, 2015.

[204] T. A. Empante, Y. Zhou, V. Klee, A. E. Nguyen, I.-H. Lu, M. D. Valentin, S. A. Naghibi Alvillar, E. Preciado, A. J. Berges, C. S. Merida, M. Gomez, S. Bobek, M. Isarraraz, E. J. Reed, and L. Bartels, "Chemical Vapor Deposition Growth of Few-Layer MoTe$_2$ in the 2H, 1T', and 1T Phases: Tunable Properties of MoTe$_2$ Films," *ACS Nano*, vol. 11, no. 1, pp. 900−905, 2017.

[205] L. Yang, W. Zhang, J. Li, S. Cheng, Z. Xie, and H. Chang, "Tellurization Velocity-Dependent Metallic–Semiconducting–Metallic Phase Evolution in Chemical Vapor Deposition Growth of Large-Area, Few-Layer MoTe$_2$," *ACS Nano*, vol. 11, no. 2, pp. 1964–1972, 2017.

[206] S. Cheng, L. Yang, J. Li, Z. Liu, W. Zhang and H. Chang, "Large area, phase-controlled growth of few-layer, two-dimensional MoTe$_2$ and lateral 1T'-2H heterostructures by chemical vapor deposition," *CrystEngComm*, vol. 19, pp. 1045-1051, 2017.

[207] J. C. Park, S. J. Yun, H. Kim, J.-H. Park, S. H. Chae, S.-J. An, J.-G. Kim, S. M. Kim, K. K. Kim, and Y. H. Lee, "Phase-Engineered Synthesis of Centimeter-Scale 1T' and 2H-Molybdenum Ditelluride Thin Films," *ACS Nano*, vol. 9, no. 6, pp. 6548–6554, 2015.

[208] J. H. Sung, H. Heo, S. Si, Y. H. Kim, H. R. Noh, K. Song, J. Kim, C.-S. Lee, S.-Y. Seo, D.-H. Kim, H. K. Kim, H. W. Yeom, T.-H. Kim, S.-Y. Choi, J. S. Kim, and M.-H. Jo, "Coplanar semiconductor–metal circuitry defined on few-layer MoTe$_2$ via

polymorphic heteroepitaxy," *Nat. Nanotechnol.*, vol. 12, pp. 1064–1070, 2017.

[209] X. Xu, S. Chen, S. Liu, X. Cheng, W. Xu, P. Li, Y. Wan, S. Yang, W. Gong, K. Yuan, P. Gao, Y. Ye, and L. Dai, "Millimeter-Scale Single-Crystalline Semiconducting MoTe$_2$ via Solid-to-Solid Phase Transformation," *J. Am. Chem. Soc.*, vol. 141, no. 5, pp. 2128–2134, 2019.

[210] L. Zhou, A. Zubair, Z. Wang, X. Zhang, F. Ouyang, K. Xu, W. Fang, K. Ueno, J. Li, T. Palacios, J. Kong, and M. S. Dresselhaus, "Synthesis of High-Quality Large-Area Homogenous 1T' MoTe$_2$ from Chemical Vapor Deposition," *Adv. Mater.*, vol. 28, no. 43, pp. 9526–9531, 2016.

[211] D. Yang, X. Hu, M. Zhuang, Y. Ding, S. Zhou, A. Li, Y. Yu, H. Li, Z. Luo, L. Gan, and T. Zhai, "Inversion Symmetry Broken 2D 3R-MoTe$_2$," *Adv. Funct. Mater.*, vol. 28, no. 26, 2018.

[212] X. Zhang, Z. Jin, L. Wang, J. A. Hachtel, E. Villarreal, Z. Wang, T. Ha, Y. Nakanishi, C. S. Tiwary, J. Lai, L. Dong, J. Yang, R. Vajtai, E. Ringe, J. C. Idrobo, B. I. Yakobson, J. Lou, V. Gambin, R. Koltun, and P. M. Ajayan, "Low Contact Barrier in 2H/1T' MoTe$_2$ In-Plane Heterostructure Synthesized by Chemical Vapor Deposition," *ACS Appl. Mater. Interfaces*, vol. 11, no. 13, pp. 12777–12785, 2019.

[213] N. Harati Pour, Y. Anugrah, S. Wu, X. Xu, and S. J. Koester, "Chemical Doping for Threshold Control and Contact Resistance Reduction in Graphene and MoS$_2$ Field Effect Transistors," In *Device Research Conference (DRC), 2013 IEEE International*. IEEE, 2013.

[214] S. Fathipour, N. Ma, W. S. Hwang, V. Protasenko, S. Vishwanath, H. G. Xing, H. Xu, D. Jena, J. Appenzeller, and A. Seabaugh, "Exfoliated multilayer MoTe$_2$ field-effect transistors," *Appl. Phys. Lett.*, vol. 105, 2014.

[215] N. Harati Pour and S. J. Koester, "Multi-Layer MoTe$_2$ p-Channel MOSFETs with High Drive Current," In *Device Research Conference (DRC), 2014 IEEE International*. IEEE, 2014.

[216] A. Prakash, H. Ilatikhameneh, P. Wu, and J. Appenzeller, "Understanding contact gating in Schottky barrier transistors from 2D channels," *Sci. Rep.*, vol. 7, 2017.

[217] K. Nagashioa, T. Nishimura, K. Kita, and A. Toriumi, "Contact resistivity and current flow path at metal/graphene contact," *Appl. Phys. Lett.*, vol. 97, 2010.

[218] W. Yang, Q.-Q. Sun, Y. Geng, L. Chen, P. Zhou, S.-J. Ding, and D. W. Zhang, "The Integration of Sub-10 Nm Gate Oxide on MoS_2 with Ultra Low Leakage and Enhanced Mobility," *Sci. Rep.*, vol. 5, 2015.

[219] Y. Liu, J. Guo, E. Zhu, L. Liao, S.-J. Lee, M. Ding, I. Shakir, V. Gambin, Y. Huang, and X. Duan, "Approaching the Schottky–Mott limit in van der Waals metal–semiconductor junctions," *Nature*, vol. 557, pp. 696–700, 2018.

[220] H. Park, G. H. Shin, K. J. Lee, and S.-Y. Choi, "Atomic-scale etching of hexagonal boron nitride for device integration based on two-dimensional materials," *Nanoscale*, vol. 10, pp. 15205–15212, 2018.

[221] J. Wang, S. Li, X. Zou, J. Ho, L. Liao, X. Xiao, C. Jiang, W. Hu, J. Wang, and J. Li, "Integration of High-*k* Oxide on MoS_2 by Using Ozone Pretreatment for High-Performance MoS_2 Top-Gated Transistor with Thickness-Dependent Carrier Scattering Investigation," *Small*, vol. 11, no. 44, pp. 5932–5938, 2015.

[222] K. M. Price, K. E. Schauble, F. A. McGuire, D. B. Farmer, and A. D. Franklin, "Uniform Growth of Sub-5-Nanometer High-κ Dielectrics on MoS_2 Using Plasma-Enhanced Atomic Layer Deposition," *ACS Appl. Mater. Interfaces*, vol. 9, no. 27, pp. 23072–23080, 2017.

[223] J. Yang, S. Kim, W. Choi, S. H. Park, Y. Jung, M.-H. Cho, and H. Kim, "Improved Growth Behavior of Atomic-Layer-Deposited High-κ Dielectrics on Multilayer MoS_2 by Oxygen Plasma Pretreatment," *ACS Appl. Mater. Interfaces*, vol. 5, no. 11, pp. 4739–4744, 2013.

[224] W. Li, J. Zhou, S. Cai, Z. Yu, J. Zhang, N. Fang, T. Li, Y. Wu, T. Chen, X. Xie, H. Ma, K. Yan, N. Dai, X. Wu, H. Zhao, Z. Wang, D. He, L. Pan, Y. Shi, P. Wang, W. Chen, K. Nagashio, X. Duan, and X. Wang, "Integrating high-quality dielectrics with one-nanometer equivalent oxide thickness on two-dimensional electronic devices," arXiv:1909.09753, 2019.

[225] Q. H. Wang and M. C. Hersam, "Room-temperature molecular-resolution

characterization of self-assembled organic monolayers on epitaxial graphene," *Nat. Chem.*, vol. 1, pp. 206–211, 2009.

[226] B. Wu, Y. Zhao, H. Nan, Z. Yang, Y. Zhang, H. Zhao, D. He, Z. Jiang, X. Liu, Y. Li, Y. Shi, Z. Ni, J. Wang, J.-B. Xu, and X. Wang, "Precise, Self-Limited Epitaxy of Ultrathin Organic Semiconductors and Heterojunctions Tailored by van der Waals Interactions," *Nano Lett.*, vol. 16, no. 6, pp. 3754–3759, 2016.

[227] J. F. Conley, Y. Ono, R. Solanki, G. Stecker, and W. Zhuang, "Electrical properties of HfO_2 deposited via atomic layer deposition using $Hf(NO_3)_4$ and H_2O," *Appl. Phys. Lett.*, vol. 82, no. 20, 2003.

[228] B. Chakraborty, A. Das, and A. K. Sood, "The formation of a p–n junction in a polymer electrolyte top-gated bilayer graphene transistor," *Nanotechnol.*, vol. 20, 2009.

[229] Y. Yu, F. Yang, X. F. Lu, Y. J. Yan, Y.-H. Cho, L. Ma, X. Niu, S. Kim, Y.-W. Son, D. Feng, S. Li, S,-W. Cheong, X. H. Chen, and Y. Zhang, "Gate-tunable phase transitions in thin flakes of 1T-TaS_2," *Nat. Nanotechnol.*, vol. 10, pp. 270–276, 2015.

[230] K. Xu, M. M. Islam, D. Guzman, A. C. Seabaugh, A. Strachan, and S. K. Fullerton-Shirey, "Pulse Dynamics of Electric Double Layer Formation on All-Solid-State Graphene Field-Effect Transistors," *ACS Appl. Mater. Interfaces*, vol. 10, no. 49, pp. 43166–43176, 2018.

[231] X. Luo, Y. Zhao, J. Zhang, M. Toh, C. Kloc, Q. Xiong, and S. Y. Quek, "Effects of lower symmetry and dimensionality on Raman spectra in two-dimensional WSe_2," *Phys. Rev. B*, vol. 88, no. 19, 2013.

[232] M. B. Dines, "Lithium intercalation via n-Butyllithium of the layered transition metal dichalcogenides," *Mat. Res. Bull.*, vol. 10, pp. 287-292, 1975.

[233] J. Xia, J. Wang, D. Chao, Z. Chen, Z. Liu, J.-L. Kuo, J. Yan, and Z. X. Shen, "Phase evolution of lithium intercalation dynamics in 2H-MoS_2", *Nanoscale*, vol. **9**, no. 22, pp. 7533–7540, 2017.

[234] K.-A. N. Duerloo and E. J. Reed, "Structural Phase Transitions by Design in Monolayer Alloys," *ACS Nano*, vol. 10, no. 1, pp. 289–297, 2016.

[235] P. E. Blöchl, "Projector Augmented-Wave Method," *Phys. Rev. B: Condens. Matter Mater. Phys.*, vol. 50, pp. 17953−17979, 1994.

[236] G. Kresse and J. Furthmüller, "Efficient Iterative Schemes for Ab Initio Total Energy Calculations Using a Plane-Wave Basis Set," *Phys. Rev. B: Condens. Matter Mater. Phys.*, vol. 54, pp. 11169−11186, 1996.

[237] J. P. Perdew, K. Burke, and M. Ernzerhof, "Generalized Gradient Approximation Made Simple," *Phys. Rev. Lett.*, vol. 77, pp. 3865−3868, 1996.

[238] G. Makov and M. C. Payne, "Periodic Boundary Conditions in Ab Initio Calculations," *Phys. Rev. B: Condens. Matter Mater. Phys.*, vol. 51, pp. 4014−402, 1995.

APPENDIX A

TERMINOLOGY

Table A. 1. Terminology

Symbol/Acronym	Quantity	Unit (SI)
GR	Graphene	N/A
2D	Two-dimensional	N/A
FET	Field-effect transistor	N/A
SCE	Short-channel effects	N/A
BP	Black phosphorus	N/A
TMDC	Transition metal dichalcogenide	N/A
hBN	Hexagonal boron nitride	N/A
MoS_2	Molybdenum disulfide	N/A
$MoTe_2$	Molybdenum ditelluride	N/A
DRAM	Dynamic random access memory	N/A
3D	Three-dimensional	N/A
SC	Semiconducting	N/A
λ	Transistor natural scaling length	nm
DIBL	Drain induced barrier lowering	unitless
$\varepsilon_{channel}$	Channel permittivity	F/m or $A^2 \cdot s^4 \cdot kg^{-1} \cdot m^{-3}$
ε_{oxide}	Dielectric permittivity	F/m or $A^2 \cdot s^4 \cdot kg^{-1} \cdot m^{-3}$
$t_{channel}$	Channel thickness	nm
t_{oxide}	Dielectric thickness	nm
μ	Field-effect mobility	cm^2/v·s
H	Hexagonal phase	N/A
T	Tetragonal phase	N/A
T'	Distorted octahedral or monoclinic phase	N/A
SHG or Φ_{SB}	Second harmonic generation	N/A
DFT	Density functional theory	N/A
PAW	Projected-augmented wave	N/A
VASP	Vienna ab initio simulation package	N/A
PBE	Perdew−Burke−Ernzerhof	N/A
GGA	Generalized gradient approximation	N/A
BZ	Brillouin zone	N/A
SOC	Spin-orbit coupling	N/A
CBM	Conduction band minimum	N/A
VBM	Valence band maximum	N/A
MBE	Molecular beam epitaxy	N/A
CVD	Chemical vapor deposition	N/A
MOCVD	Metal-organic CVD	N/A

ALD	Atomic layer deposition	N/A
PVD	Physical vapor deposition	N/A
PDMS	Polydimethylsiloxane	N/A
PMMA	Poly(methyl methacrylate)	N/A
PS	Polystyrene	N/A
I_{ON}	ON-state current	A
I_{OFF}	OFF-state current	A
I_{ON}/I_{OFF}	Transistor on-to-off current ratio	unitless
BTBT	Band-to-band tunneling	N/A
GIDL	Gate-induced drain leakage	A
I_{sub}	Subthreshold leakage	A
I_{gate}	Gate leakage	A
k_B	Boltzmann constant	eV/K or m^2 kg s^{-2} K^{-1}
E_g	Band gap	eV
2T	Two-transistor	N/A
TFT	Thin film transistor	N/A
R_c	Contact resistance	Ω
W	Channel width	μm
L	Channel length	μm
h	Planck's constant	J·s
e or q	Electron charge	C
k_F	Fermi wavevector	m^{-1}
n_{2D}	2D charge carrier density	10^{13} m^{-2}
SBH	Schottky barrier height	eV
SBW	Schottky barrier width	nm
FLP	Fermi-level pinning	N/A
vdW	van der Waals	N/A
I_D	Drain current	A
V_{DS}	Drain-to-source voltage	V
V_{GS}	Gate-to-source voltage	V
V_{BG}	Backgate voltage	V
E_A	Activation energy	eV
V_{FB}	Flat-band voltage	V
T	Temperature	K
CMOS	Complementary metal–oxide–semiconductor	N/A
MOSFET	Metal–oxide–semiconductor FET	N/A
EBE	Electron beam evaporation	N/A
EBL	Electron beam lithography	N/A
ADF	Annular dark-field	N/A
TEM	Transmission electron microscopy	N/A
STEM	Scanning transmission electron microscopy	N/A
L_T	Transfer length	nm
L_C	Contact length	nm

ρ_C	Specific contact resistivity	$\Omega \cdot cm^2$
ρ_S	Sheet resistivity	$\Omega \cdot cm^2$
R_S	Sheet resistance of channel semiconductor	$\Omega/\square$
R_T	Total resistance	Ω
R_{CH}	Resistance of the device channel	Ω
HER	Hydrogen evolution reaction	N/A
AFM	Atomic force microscopy	N/A
MS	Metallic-semiconducting	N/A
XPS	X-ray photoelectron spectroscopy	N/A
XRD	X-ray powder diffraction	N/A
RMS	Root-mean-square	N/A
BF	Bright-field	N/A
SAEDP	Selected area electron diffraction pattern	N/A
DF	Dark-field	N/A
HRTEM	High-resolution TEM	N/A
LAADF	Low-magnification low-angle annular dark-field	N/A
HRSTEM	High-resolution STEM	N/A
FFT	Fourier transform	N/A
TLM	Transfer length method	N/A
SS	Subthreshold swing	mV/dec
VLSI	Very Large Scale Integration	N/A
ML	Monolayer	N/A
PTCDA	3,4,9,10-perylene-tetracarboxylic dianhydride	N/A
TDMAH	Tetrakis(dimethylamido) hafnium	N/A
PCM	Phase-change memory	N/A
EDL	Electric double layer	N/A
LiClO4	Lithium perchlorate	N/A
PEO	Polyethylene oxide	N/A
V_{SG}	Side-gate voltage	V
GND	Ground	N/A
FWHM	Full width at half maximum	N/A
ω	Mode frequencies	cm^{-1}
EPC	Electron-phonon coupling	N/A
n-BuLi	n-butyl lithium	N/A
NEB	Nudged elastic band	N/A
m_0	Mass of an electron (9.11 x 10^{-31})	Mass (kg)
g_m	Transconductance	Siemens (L)
D_{it}	Density of Interface Traps	cm^{-2}/eV
C_{ox}	Gate dielectric capacitance	F
SEM	Scanning electron microscope	N/A
FIB	Focused ion beam	FIB

APPENDIX B

SUPPORTING INFORMATION

B.1 DFT Computational Details

DFT calculations were performed by Javad G. Azadani and Prof. Tony Low using the projected-augmented wave (PAW) pseudopotential method [235] as implemented in the Vienna ab initio simulation package (VASP) [236]. Van der Waals corrections and spin−orbit coupling were included in the calculations. The Perdew−Burke−Ernzerhof (PBE) functional [237] was closed within the generalized gradient approximation (GGA) to treat the exchange−correlation interaction of electrons. The plane-wave kinetic-energy cutoff was set at 300 eV. A set of $(21 \times 21 \times 1)$ k-point sampling is used for Brillouin zone (BZ) integration in k-space. All atomic positions were optimized using the conjugate gradient method, where the total energy and atomic forces were minimized. The energy convergence value between two consecutive steps of $10−6$ eV was chosen, and a maximum force of 0.001 eV/Å was allowed on each atom. A minimum of 15 Å vacuum spacing was added along the direction perpendicular to the 2D plane, in order to avoid the interaction between the adjacent supercells. While applying an electric field, a dipole correction was applied to avoid spurious dipole interactions [238].

B.2 XRD and XPS of CVD-grown few-layer 2H and 1T′ MoTe$_2$

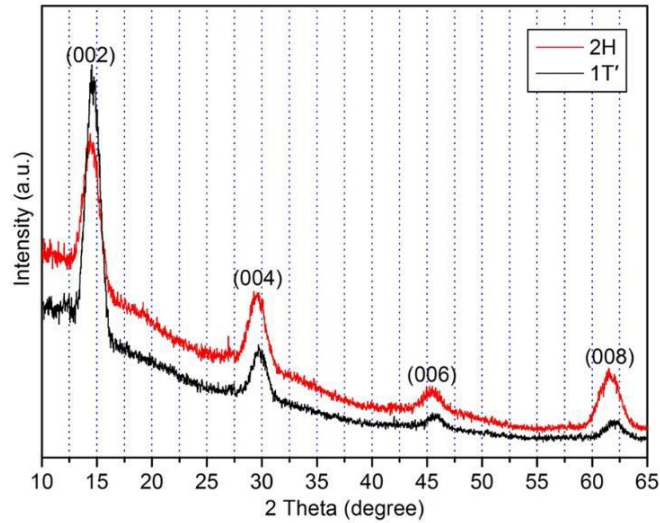Figure B.1: XRD patterns of few-layer 2H (red) and 1T′ (black) MoTe$_2$. The peaks of as-synthesized few-layer 2H and 1T′ MoTe$_2$ are indexed to hexagonal 2H MoTe$_2$ (JCPDS #73-1650) and monoclinic 1T′ MoTe$_2$ (JCPDS #71-2157), respectively. Reprinted with permission from reference [37].
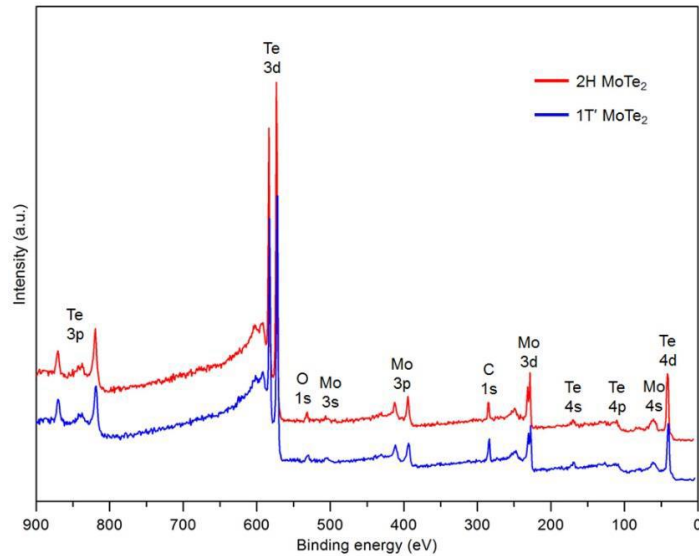

Figure B.2: XPS survey spectrum of few-layer 2H (red) and 1T′ (blue) MoTe$_2$. Reprinted with permission from reference [37].

B.3 Indexed polycrystalline diffraction rings of 1T'-MoTe$_2$

The selected area electron diffraction pattern in Figure 2.4 in Chapter 2.2.3 taken from a region of a diameter of 600 nm polycrystalline 1T′-MoTe$_2$ is well labeled with the crystallographic planes of the 1T′-MoTe$_2$ structure, as shown in Figure B.3, and the corresponding radii of the diffraction rings are listed in Table B.1. The angular deviation of all the planes off the [001] zone-axis is within 5° indicating that the 1T′ polycrystalline MoTe$_2$ film is textured along the [001] direction. The measurement was performed by Huairuo Zhang at NIST.

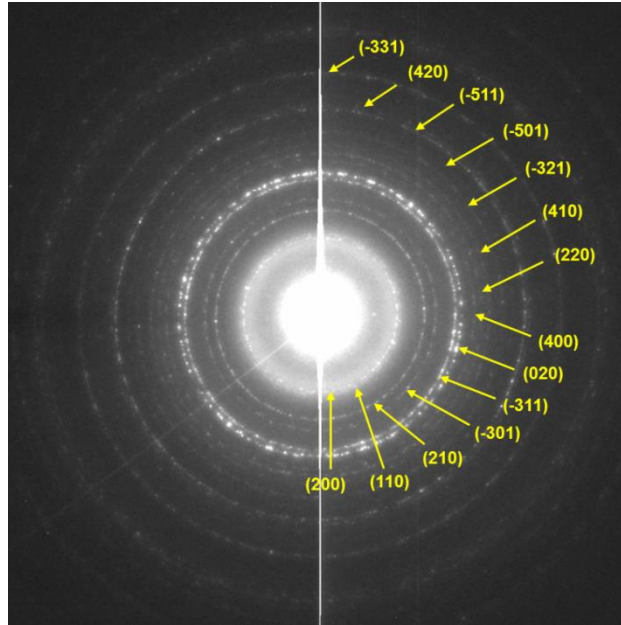Figure B.3: Selected-area electron diffraction patterns taken from a 1T′-MoTe$_2$ region with a diameter of 600 nm showing the polycrystalline diffraction rings. All the rings can be indexed as hk0 crystallographic planes (parallel to [001] zone-axis) or hkl crystallographic planes within a 5° off the [001] zone-axis, which suggests the 1T′ polycrystalline film was textured along the [001] direction.

Table B.1. Experimental and theoretical radiuses of diffraction rings of 1T′ MoTe₂

Experimental radius of diffraction ring (1/nm)	Theoretical radius of diffraction ring (1/nm)	hkl	hkl ∩ (001) (degree)
3.122	3.167	200	90
3.259	3.289	110	90
4.239	4.283	210	90
4.695	4.756	-301	85.19
5.492	5.562	-311	85.89
5.766	5.765	020	90
6.290	6.334	400	90
6.541	6.578	220	90
6.883	6.959	410	90
7.452	7.474	-321	86.94
7.817	7.901	-501	88.68
8.341	8.410	-511	88.76
8.501	8.565	420	90
9.868	9.870	-331	87.69

B.4 TEM/STEM of the thickness variation and misorientation in the 2H region

Figure B.4a is a dark-field (DF) TEM image taken from a round 2H region using a single (100) reflection as shown in Figure 2.4b. There are some small areas presenting a much darker contrast than the surrounding. Selected area electron diffraction pattern (SAEDPs) from the dark region SA-2 shows a very similar 2H pattern as the one from the

large area SA-1 (Figures B.4b and B.4c). Figures B.4d-B.4g show the atomic models and the corresponding simulated diffraction patterns of 2H and 3R structures. It should be noted that the mixture of 2H and 3R stackings can have a similar diffraction pattern as that of 2H, and the DF image using (100) reflection can make the mixture region darker than the pure 2H region, assuming a flat film with a uniform thickness. However, the mixture region of 2H and 3R structures can be easily differenctiated from 2H by atomic resolution HRSTEM imaging, and we have never observed such a mixture in our film. The darker region in the DF images should be attributed to a smaller thickness in local area.
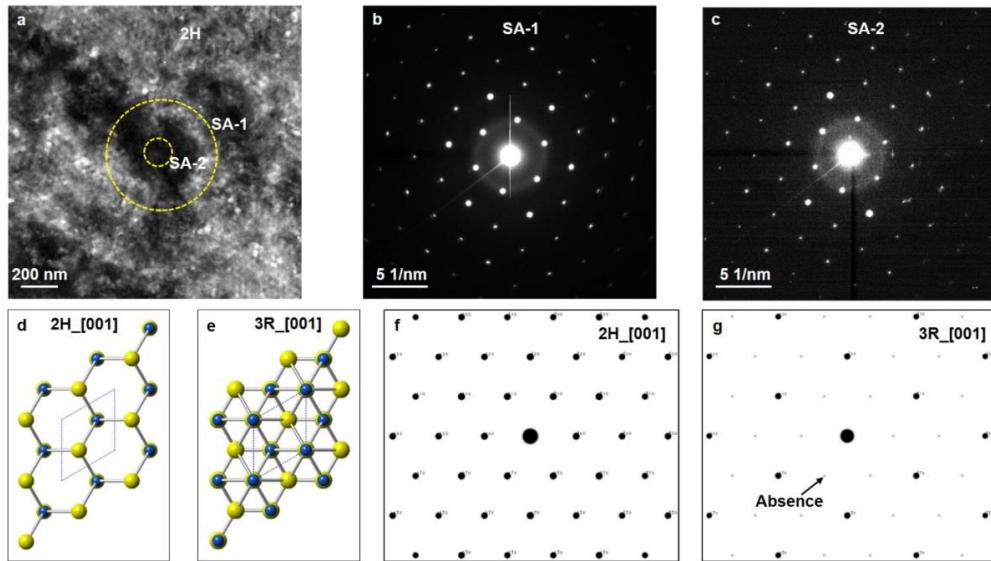

Figure B.4: TEM/STEM of the thickness variation in 2H region. (a) Dark field TEM image taken from a round 2H region using a single (100) reflection. (b)-(c) Electron diffraction patterns taken from the selected areas of SA-1 and SA-2 shown in (a), respectively. (d)-(e) Atomic models of 2H and 3R structures, and (f)-(g) their corresponding simulated electron diffraction patterns.

B.5 Interface Traps Density Calculation

The interface traps density is extracted from the minimum subthreshold swing (SS). SS is extracted by taking the derivative of the I_D-V_{GS} curves and taking the

reciprocal of the derivatives. Then the interface traps capacitance, C_{it}, can be extracted

from the minimum SS by $SS = \ln(10) \times (k_B T/q) \times (1 + C_{it}/C_{ox})$. The interface trap density,

D_{it}, can be approximately calculated by $D_{it} = C_{it}/q$.

B.6 Field-effect hole mobility at different temperatures

We extracted the field-effect hole mobility, μ, from the temperature-dependent

transfer characteristics for the 2H-only and 2H/1T′ devices. The value of μ at a given

temperature and V_{DS} is extracted at the maximum transconductance, g_m, which is defined

as the maximum point in the derivative of the I_D *vs.* V_{GS} curve. The mobility is then

calculated by

$$\mu = g_m \cdot L / (W \cdot C_{ox} \cdot V_{DS}) ,$$

where L and W are the length and width of the device, respectively. C_{ox} is the gate

dielectric capacitance and V_{DS} is the drain-to-source voltage. The extracted μ as a

function of temperature for the 2H-only and the 2H/1T′ devices are shown in Figure B.5a
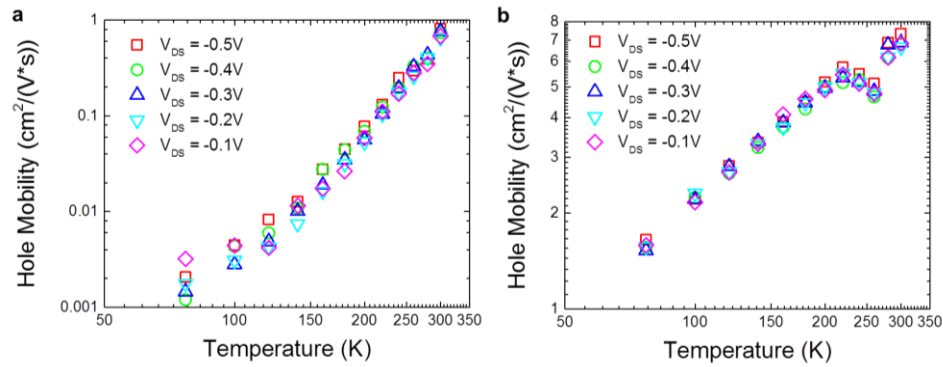
and B.5b, respectively.

Figure B.5: Field-effect hole mobility (log scale) as a function of temperature (log scale) for (a) the 2H-only device and (b) the 2H/1T′ device in Figure 5 at different values of V_{DS}. For the 2H/1T′ device, the average length of the 2H region between the 1T′ ends is used to calculate the mobility.

The 2H/1T′ device shows about 10 times higher field-effect hole mobility than that of the 2H-only device because of the reduced contact resistances at the 1T′/metal and 2H/1T′ interfaces. The mobility is relatively low because of the high defect density in the material. The 2H-only and 2H/1T′ device show a power-law mobility *vs.* temperature dependence, $\mu \propto T^x$, where $x = 5.9$ and $x = 1.3$, respectively. The slope of the 2H/1T′ device is close to the typical factor, $x = 1.5$, for Coulomb scattering dominant transport in the material due to the negligible effect from the contacts, which confirms the Ohmic nature of the metal/1T′ and 2H/1T′ interfaces. Coloumb-scattering-limited (rather than phonon-limited) mobility is not surprising in this material, give the rather high interface trap density in our samples. In addition, the dependence of V_{DS} on the mobility in the 2H/1T′ device is less than that in the 2H-only device, which again confirms the Ohmic-like contacts in the 2H/1T′ device. However, for the 2H-only device, the contact resistance and the sheet resistance are on the same order of magnitude, so we would expect higher V_{DS} dependence.

B.7 Temperature-dependent device behavior for another set of 2H-only and 2H/1T′ devices

Figure B.6 shows the temperature-dependent transport characteristics of another set of 2H-only and 2H/1T′ device from Sample 1, same substrate as the set used in Figure 3.3. The observed behavior is consistent with the results in Figure 3.3.
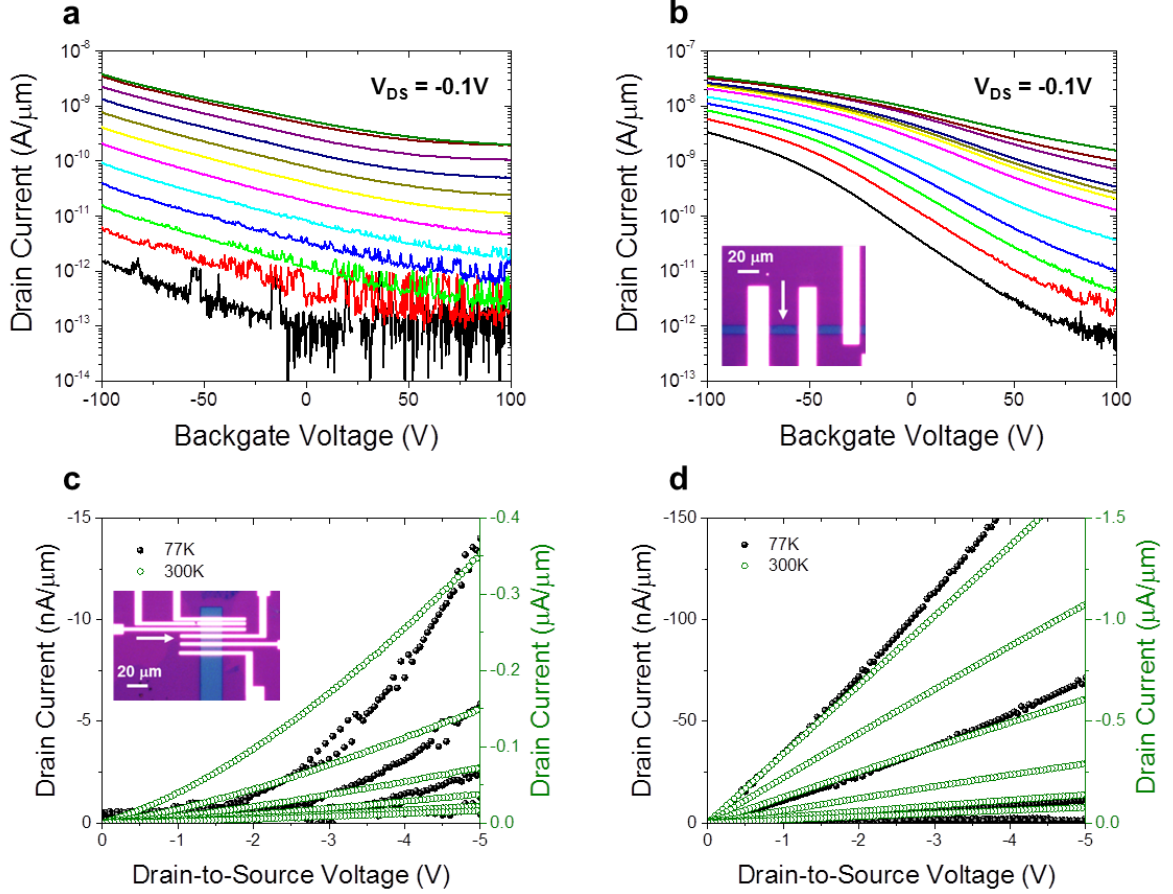
Figure B.6: Temperature-dependent transport characteristics of another set of 2H-only and 2H/1T′ device from the same growth as the set shown in Figure 3.3. (a)-(b) Transfer characteristics (I_D vs. V_{BG}) of (a) 2H-only device and (b) 2H/1T′ device at $V_{DS} = -0.1$ V for temperatures of 77 K (black curve), and from 100 K (red curve) to 300 K (olive curve), in steps of 20 K. (c)-(d) Output characteristics (I_D vs. V_{DS}) of 2H-only and 2H/1T′ device for V_{BG} varying from -100 V (top curve) to +100 V (bottom curve) in steps of +40 V at $T = 77$ K (black points) and $T = 300$ K (olive points). Optical images of the 2H-only and 2H/1T′ device are shown as an inset in (c) and (b), respectively. The dimensions of the 2H-only device are $L_{DS} = 4$ μm and $W = 21$ μm, while the 2H/1T′ device has $L_{DS} = 26$ μm and $W = 9$ μm (the length of the 2H region is about 20 μm).

B.8 Device performance statistics

To show the reproducibility of the devices from growth to growth, we plot histograms of normalized on resistances for devices fabricated on films from four

different growths, as listed in Table B.2. The film thickness of sample 1 is around 6 nm and the film thicknesses of sample 2-4 are around 10 nm.

Table B.2. Number of devices of each type on samples from different growths

Sample Index	Substrate Oxide Thickness	No. of 2H-only Devices	No. of 2H/1T′ Devices	No. of 1T′-only Devices
1	300 nm	10	14	11
2	300 nm	11	14	0
3	110 nm	6	10	2
4	110 nm	6	11	4

Histograms of normalized on resistances for 2H-only and 2H/1T′ devices fabricated on 300 nm SiO_2/Si substrates (Sample 1 and 2) and 110 nm SiO_2/Si substrates (Sample 3 and 4) are shown in Figures B.7a and B.7b, respectively. The on resistances of 2H-only and 2H/1T′ devices were taken at $V_{BG} = -100$ V and $V_{DS} = -0.1$ V for Samples 1 and 2, and at $V_{BG} = -50$ V and $V_{DS} = -0.05$ V for Samples 3 and 4. Overall, 2H/1T′ devices show lower on resistance than that of 2H-only devices owing to the reduced contact resistance at the metal/1T′ interface, in consistent with the results in the manuscript. Figures B.7c shows histograms of normalized on resistance of 1T′-only devices fabricated on two different substrates at $V_{BG} = 0$ V and $V_{DS} = -0.05$ V. It should be noted that the normalized on resistance levels for the same type of devices from two substrates do not match well because of different bias conditions, dielectric thicknesses, and film thicknesses.
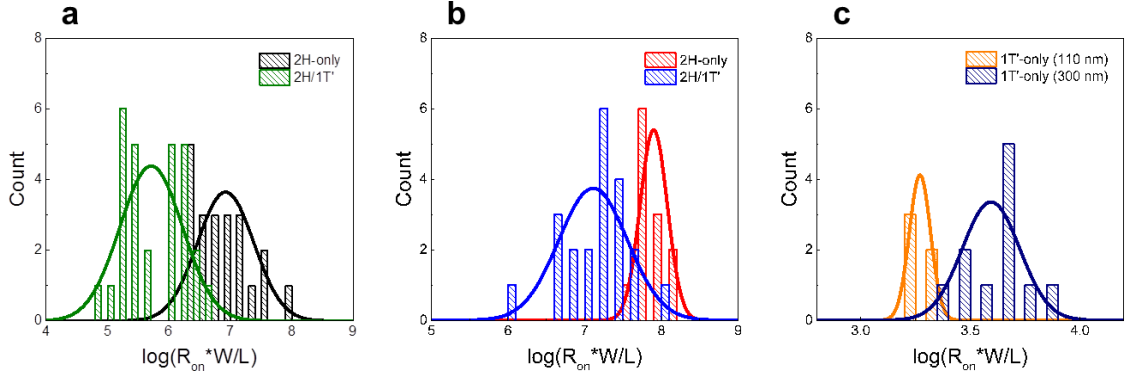
Figure B.7: Histograms of normalized on resistances, R_{on}, in log scale for (a) 2H-only and 2H/1T′ devices made on 300 nm SiO$_2$/Si substrates at V_{BG} = -100 V and V_{DS} = -0.1 V, and (b) 2H-only and 2H/1T′ devices made on 110 nm SiO$_2$/Si substrates at V_{BG} = -50 V and V_{DS} = -0.05 V, with a bin size of 0.2, and (c) 1T′-only devices on 300 nm and 110 nm SiO$_2$/Si substrates at V_{BG} = 0 V and V_{DS} = -0.05 V, with a bin size of 0.1. The 2H-only and 2H/1T′ devices in each histogram come from two different samples, and the 1T′-only devices come from three different samples. All on resistances are multiplied by the channel length, L, and divided by the channel width, W. In (a), the distribution of the 2H-only devices (2H/1T′ devices) has a mean of 6.92 (5.71) and standard deviation of 0.46 (0.5). In (b), the distribution of the 2H-only devices (2H/1T′ devices) has a mean of 7.9 (7.11) and standard deviation of 0.18 (0.45). In (c), the distribution of the 1T′-only devices on the 110 nm (300 nm) SiO$_2$/Si substrate has a mean of 3.27 (3.59) and standard deviation of 0.05 (0.13).

B.9 Effective Schottky barrier height extraction

The slopes of the Arrhenius curves are $(qV_{DS}/\eta - \Phi_{SB})$, so the effective Schottky barrier height, Φ_{SB}, can be extracted by plotting the slopes *vs.* V_{DS} and then extrapolating to V_{DS} = 0. A representative plot of the extraction for a 2H-only device at a given V_{BG} is shown in Figure B.8. Φ_{SB} is extracted for all values of V_{BG}.
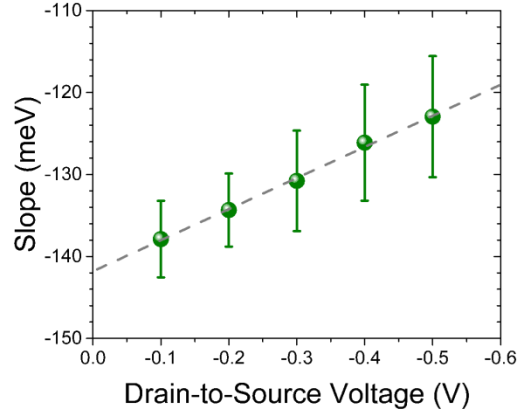
Figure B.8: Slope of the Arrhenius plot for the same 2H-only device in Figure 3.3 of the manuscript plotted *vs.* V_{DS} at $V_{BG} = 0V$.

B.10 Comparison of V_{BG}-dependent effective Schottky barrier heights for different devices

Figure B.9 compares the V_{BG}-dependent effective Schottky barrier heights for devices in Figure 3.3 and devices in Figure B.6. The overall values of the barrier heights and the gate-bias dependence are in excellent agreement with each other.
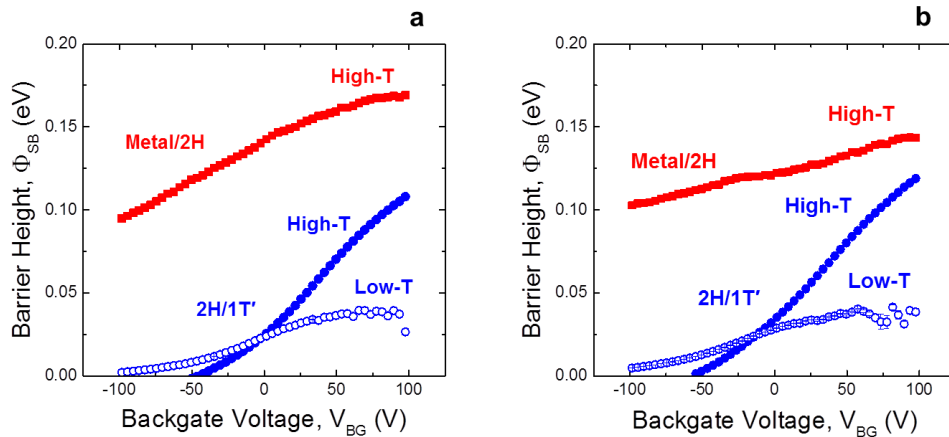

Figure B.9: SBH comparison. (a) Effective Schottky barrier height of the 2H-only device (shown in Figure 3.3) in the high temperature regime (red squares) and 2H/1T′ device (shown in Figure 3.3) in the high- (close blue circles) and low- (open blue circles) temperature regimes as a function of V_{BG}. (b) Effective Schottky barrier height of the 2H-only and 2H/1T′ devices shown in Figure B.6 as a function of V_{BG}.

167

B.11 Effective Schottky barrier height statistics

To further show that the observed large energy barrier difference at the metal/2H and 2H/1T′ interface is not particular to the devices shown in the manuscript, the effective energy barrier heights at $V_{BG} = 0$ for several 2H-only and 2H/1T′ devices were extracted and summarized in the box plots shown in Figure B.10. The channel thicknesses of these devices range from 6 nm to 10 nm. The two box plots are relatively short suggesting that the overall barriers at each interface have a high level of agreement. The barrier heights at the metal/2H interfaces are consistently ~ 100 meV higher than for the 2H/1T′ interfaces.
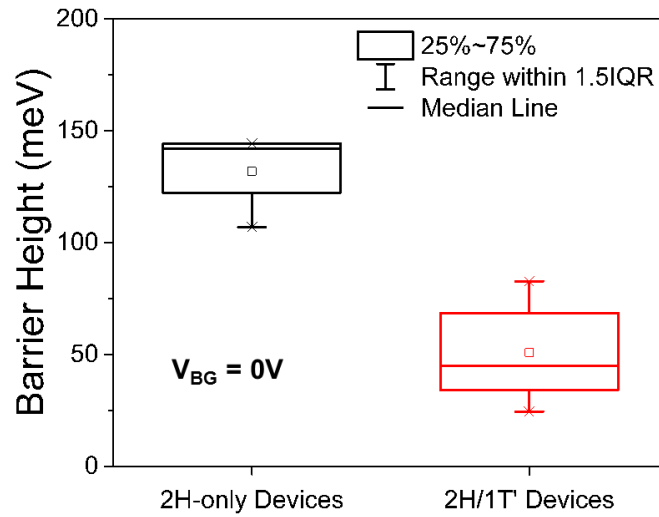

Figure B.10: Box plots for effective Schottky barrier heights at $V_{BG} = 0$ for five 2H-only and five 2H/1T′ devices. The 25th~75th percentiles are shown as boxes, and ranges within 1.5 interquartile range (IQR) are shown as whiskers. The mean (median) are 132 meV (142 meV) for 2H-only devices and 51 meV (45 meV) for 2H/1T′ devices.

B.12 Flat-band barrier extraction at the 2H/1T′ interface

The effective energy barrier height as a function of the back-gate voltage is plotted in Figure B.11 for the 2H/1T′ device from Figure 3.3 in the high-temperature

regime. The flat-band barrier height, Φ_{SB0}, which is the barrier at $V_{BG} = V_{FB}$ (flat-band

voltage), is extracted at the point where the slope deviates the linear dependence on V_{BG}.

As illustrated in Figure B.11, the Φ_{SB0} for the 2H/1T′ device is estimated to be between

20 meV (at $V_{BG} = -6.5$ V) and 40 meV (at $V_{BG} = 19.5$ V). Since there is no thermally-

activated energy barrier at the metal/1T′ MoTe$_2$ interface, this extarcted barrier is at the
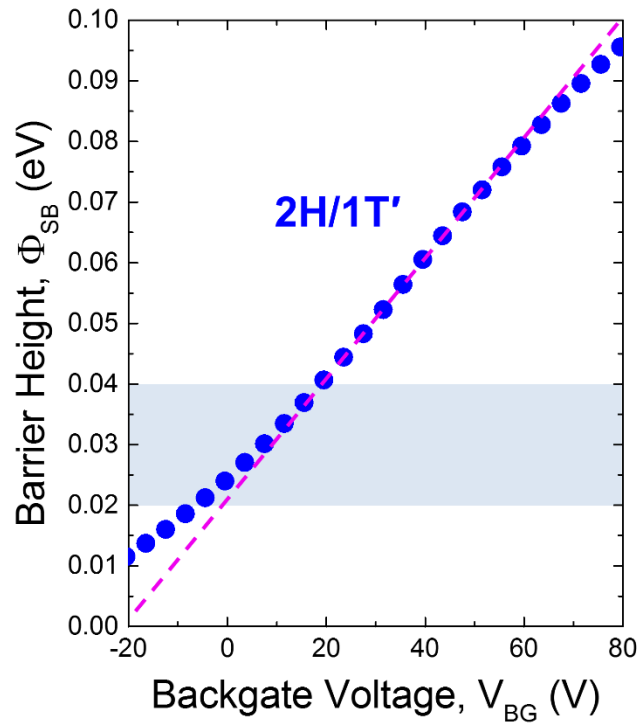
2H/1T′ interface.

Figure B.11: Effective Schottky barrier height of the 2H/1T′ device in the high temperature regime as a function of V_{BG}. The dash magenta line fits the linear portion of the curve, and the flat-band barrier height is estimated to be between ~30 $\pm$ 10 meV.

B.13 Band diagrams for the metal/2H and 2H/1T′ interfaces under

different bias conditions

Figure B.12a shows the Φ_{SB} *vs.* V_{BG} plot for the metal/2H and 2H/1T′ devices

from Figure 3.3 in the high-temperature regime, where Figures B.12b and B.12c show

schematic illustrations of the lateral energy band diagrams. The diagram in Figure B.12b

shows that the weaker backgate voltage dependence is due to the relatively long transfer

length under the contact metal, as opposed to at the edge of the contact as in the case of
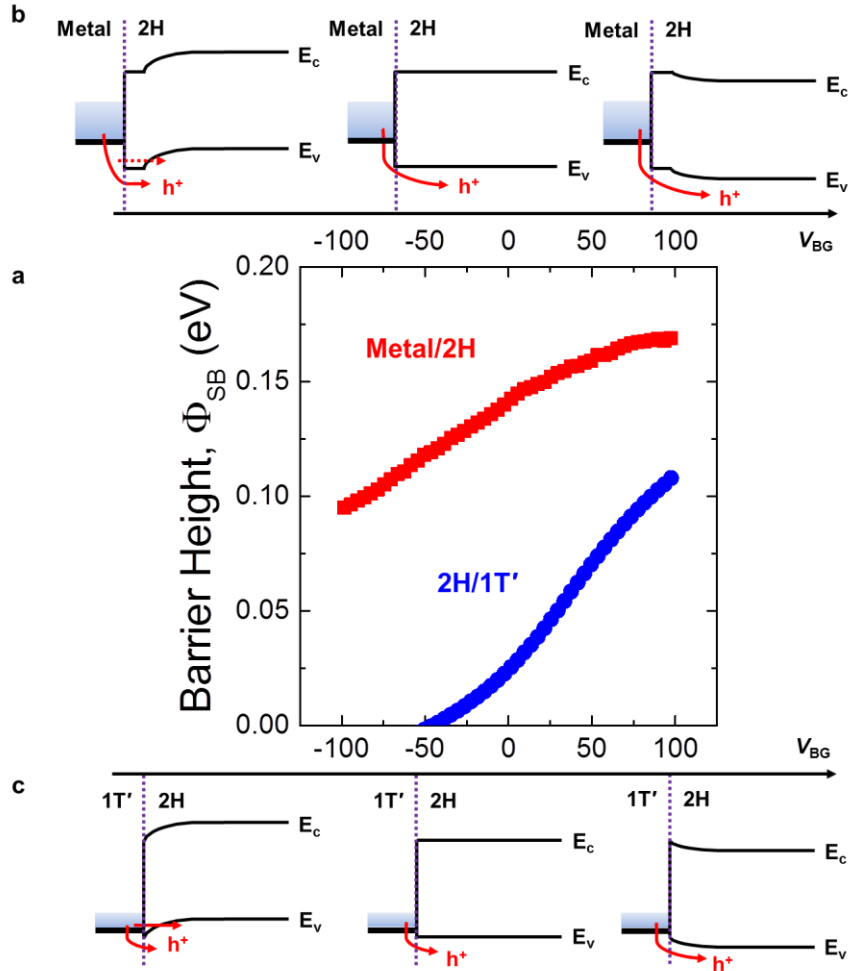
the 2H/1T′ devices (Figure B.12c).

Figure B.12: Band diagrams for the 2H-only and the 2H/1T′ device under different values of backgate voltage, V_{BG}. (a) Effective Schottky barrier height of the 2H-only device (red squares) and 2H/1T′ device (close blue circles) as a function of V_{BG}. (b)-(c) The gate voltage modulations of the band diagrams and hole (h+) injections at the (b) metal/2H interface and (c) 2H/1T′ interface when V_{BG} increases from -100 V to +100 V. The purple dotted lines indicate the metal/2H and 2H/1T′ interfaces, respectively. In (b), the pinned regions underneath the metal contacts inhibits the gate modulation of the effective barrier height, Φ_{SB}, while in (c) the lateral nature of the interface allows stronger modulation of Φ_{SB}.

B.14 SEM of *sequentially*-grown 2H/1T′-MoTe₂ homojunctions using planar deposition

The etching process used to pattern 2H-MoTe₂ channels causes undercutting to the 2H-MoTe₂ film underneath the PMMA patterns, so Mo nanoislands deposited using planar evaporation will not be in contact with the 2H-MoTe₂ film. As a result, the synthesized 1T′-MoTe₂ will not be physically connected to the 2H-MoTe₂ film. Figure B.13 shows SEM images of the as-synthesized 2H/1T′-MoTe₂ homojunctions. A gap is clearly seen at the interface suggesting that Mo nanoislands barely migrate during the synthesis of 1T′-MoTe₂ film. Conformal deposition of Mo nanoislands should be used to ensure direct contacts between Mo nanoislands and the edges of the 2H-MoTe₂ film.
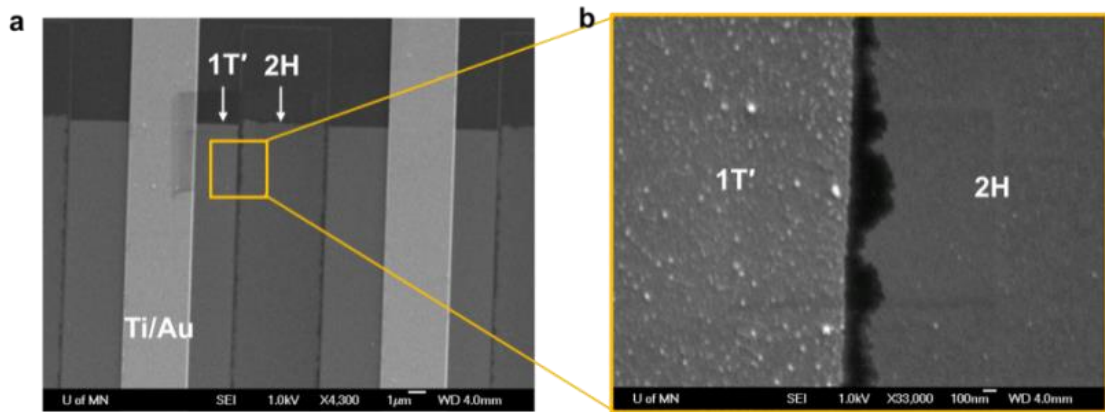

Figure B.13: SEM of *sequentially*-grown 2H/1T′ MoTe₂ homojunctions fabricated using planar evaporation. (a) low-magnification and (b) high-magnification SEM of the 2H/1T′ homojunctions with Ti/Au contacts.

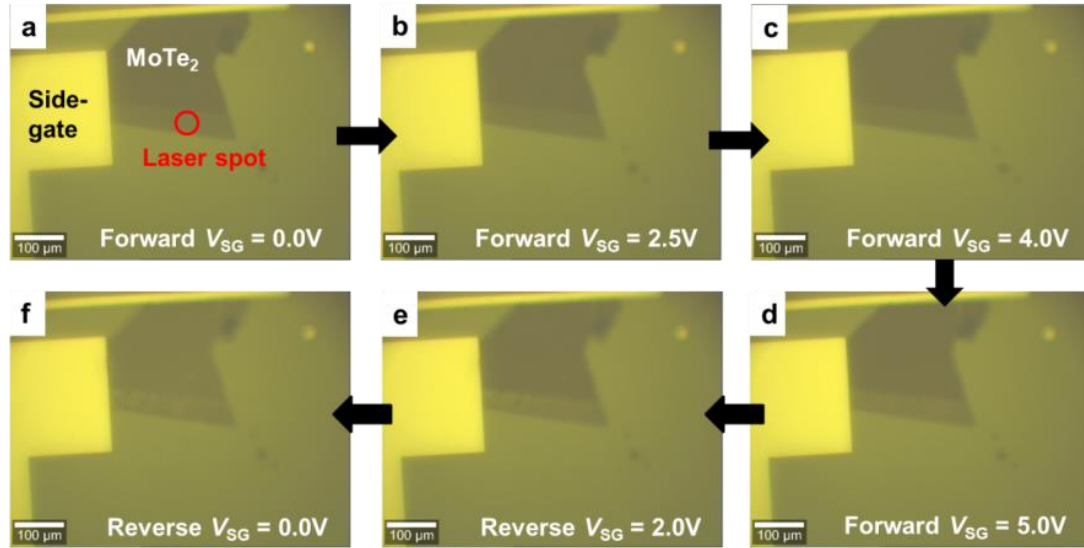## B.15 Degradation of MoTe$_2$ fakes under Li electrolyte gating

Figure B.14: Degradation of exfoliated few-layer MoTe$_2$ flakes during the gated Raman experiment. (a-f) Optical images of the flake at different side-gate voltages. The side-gate voltage is swept from 0 V to 5 V and then from 5 V back to 0 V. The laser power is kept below 1 mW to avoid damages from the laser.

B.16 Raman spectra of MoTe$_2$ flake when sweeping V_{SG} between 0 V and -4 V
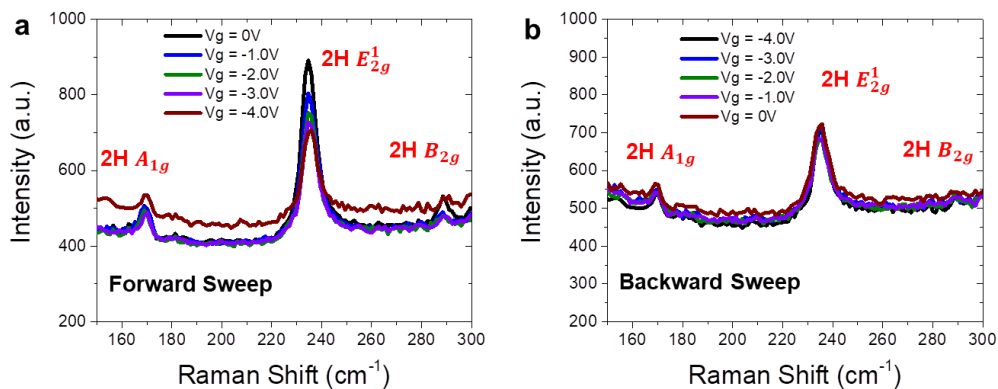

Figure B.15: Gated-Raman characterization of an exfoliated few-layer MoTe$_2$ flake with Li electrolyte gating. (a-b) The evolution of Raman spectra when sweeping V_{SG} from (a) 0 V to -4 V (forward sweep) and (b) from -4 V to 0 V (backward sweep), with step of 1.0 V.

B.17 Raman characterization of a few-layer MoTe$_2$ flake after 3 h immersion in *n*-BuLi solution
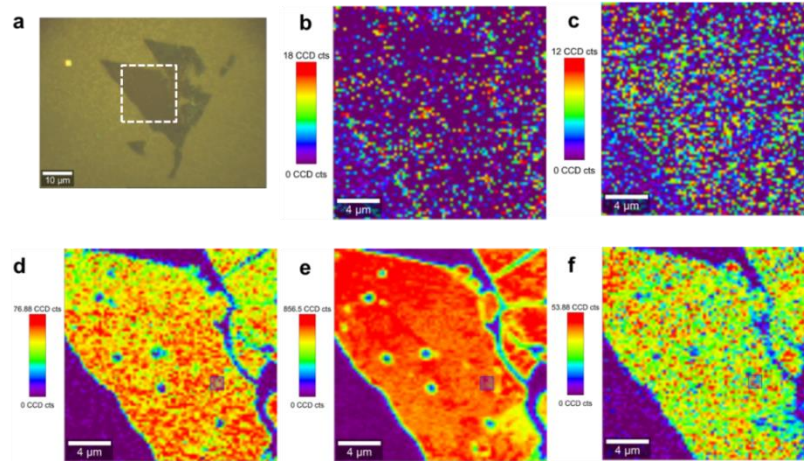
Figure B.16: Raman maps of an exfoliated few-layer MoTe$_2$ flake after 3 h immersion in organic *n*-BuLi solution. (a) Optical image of the flake after the 3h treatment. Raman intemsity maps of (b) 1T$'$ B_g, (c) 1T$'$ A_g, (d) 2H A_{1g} , (e) 2H E^1_{2g} , and (f) 2H B_{2g} of the region in the white dashed box in (a).

B.18 XPS of an exfoliated few-layer MoTe$_2$ flake after *n*-BuLi treatment

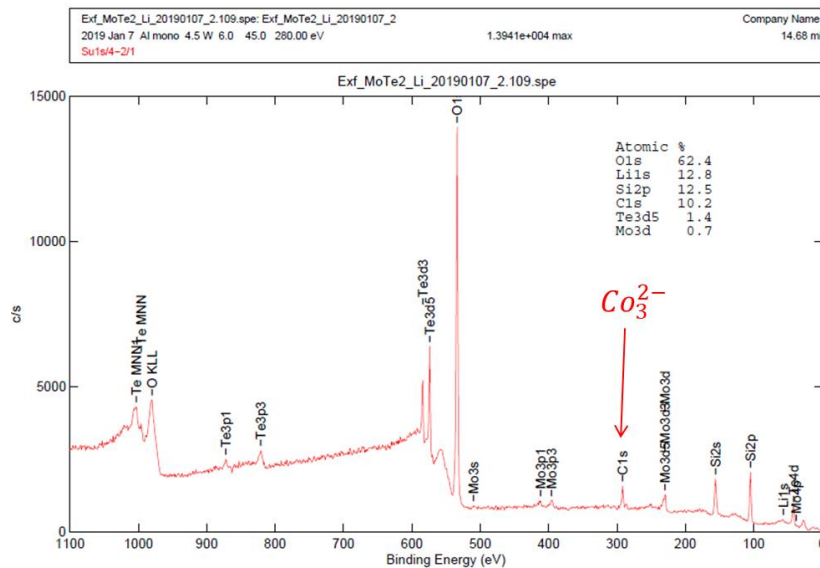Figure B.17: X-ray photoelectron spectroscopy (XPS) of the surface of an exfoliated few-layer MoTe$_2$ flake after 3h immersion in *n*-BuLi solution.

APPENDIX C

SELECTED EXPERIMENTAL PROCESSES

This section describes the details of selected experimental processes.

C.1 Synthesis Details of Few-Layer 2H, 2H/1T′ Homojunction, and 1T′ MoTe$_2$

Few-layer 2H, lateral 2H/1T′ homojunctions and 1T′ MoTe$_2$ are synthesized from Mo nanoislands in a horizontal hot-wall single-zone furnace equipped with mass flow controllers and a vacuum pump. The synthesis started by depositing Mo nanoislands on SiO$_2$/Si substrates through electron beam evaporation (CHA SEC-600) under high vacuum. The deposited Mo nanoislands have heights of about 1-3 nm and widths of about a few hundred nanometers. The Mo nanoislands on SiO$_2$/Si substrates are placed face down on a 5 cm $\times$ 2 cm $\times$ 2 cm alumina boat containing a Te lump placed at the center of the heating zone in a 3-in. quartz tube (MTI Corporation), followed by annealing in Ar/H$_2$ (5 sccm/5 sccm) environment. Te lumps were prepared by annealing Te slugs (0.8 g, 99.999%, Sigma-Aldrich) at 635 °C for 1 h under Ar environment. After the quartz tube was evacuated to < 100 mTorr, Ar flowed at a rate of 500 sccm until the pressure reached atmospheric pressure. At atmospheric pressure, Ar and H$_2$ flowed at rates of 5 and 5 sccm, respectively. For the synthesis of few-layer 2H, lateral 2H/1T′, and 1T′ MoTe$_2$, the furnace was respectively ramped to 635 °C, 585 °C, and 535 °C in 15 min (linear ramp rates $\sim$ 40 °C/min, 37.3 C/min, and 34 C/min), and was kept at the temperatures for 1 h. After the reactions, Ar was turned to the flow rate of 100 sccm and the furnace was rapidly cooled down to room temperature with the furnace lid open.

C.2 Sample Preparation for Plan-View TEM

To prepare the sample for plan-view TEM, the as-grown MoTe$_2$ homojunction film on a SiO$_2$/Si substrate was spin-coated with poly(methylmethacrylate) (950 ka.u. PMMA C4) at 3000 rpm for 60 s, followed by 2 min annealing at 100 °C. The sample was then cut into small pieces with sizes slightly larger than that of a mesh copper TEM grid with a lacey carbon film (Ted Pella product no. 01894). The small pieces were then floated on a 6:1 buffered oxide etch (BOE) solution at room temperature for ∼15−20 min until the MoTe$_2$ films with PMMA were completely detached from the substrates (four sides of the pieces were scratched off with tweezers for BOE etchant access). Next, the MoTe$_2$ films with PMMA were rinsed in DI water three times (∼5 min/each) and transferred onto the mesh copper grids. After the films dried out on the grids, the grids were gently placed in acetone with self-closing tweezers to remove PMMA and rinsed in IPA. The transfer flowchart and images of the transferred films on TEM grids are provided in Figure C.1.
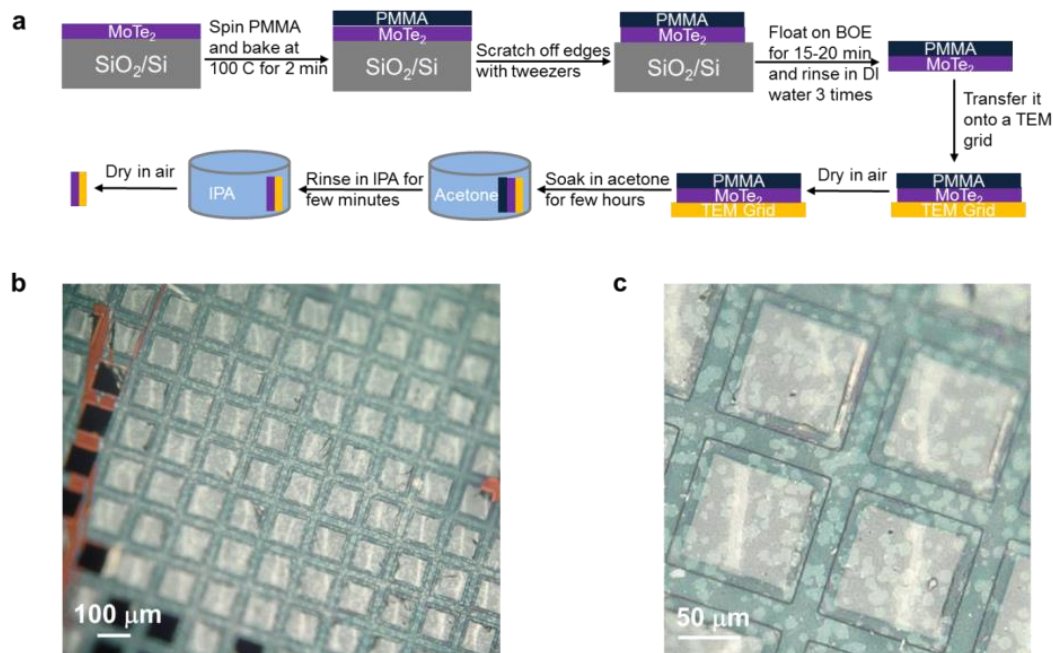
Figure C.1: The transfer flowchart and images of the transferred films on TEM grids. (a) Sample preparation process for plan-view TEM. Zoom-out image (b) and zoom-in image (c) of a transferred MoTe$_2$ homojunction film on copper TEM grid with a lacey carbon film. The grid has good coverage.

C.3 Sample Preparation for Cross-Sectional TEM.

An FEI Nova NanoLab 600 dual-beam scanning electron microscopy and focused ion beam (SEM/FIB) system were employed to prepare the cross-sectional transmission electron microscopy (TEM) samples. SEM was utilized to identify regions of 2H-MoTe$_2$ and 1T′-MoTe$_2$ (due to the electron channeling response of nanocrystalline and single crystals). A region of 20 μm in length across the 2H-MoTe$_2$/1T′-MoTe$_2$ boundary was chosen for lamellar TEM sample preparation. A 100 nm-thick Pt layer was initially deposited on top of the film by electron-beam induced deposition to protect the sample surface, then followed by 2 μm ion-beam-induced Pt deposition. To reduce Ga-ion damage, in the final stage of FIB preparation, the TEM sample was thinned with 2 kV Ga-ions using a low beam current of 29 pA and a small incident angle of 3°.

C.4 Fabrication of *in-situ*-Grown MoTe$_2$ Homojunction FETs

The MoTe$_2$ field-effect transistors were fabricated on a Si substrate with 300 nm SiO$_2$ grown on top, upon which a lateral few-layer 2H/1T′ mixed-phase MoTe$_2$ was grown. Alignment marks were first patterned on the substrate by coating poly(methyl methacrylate) (950 ka.u. PMMA C4) and exposing PMMA with electron beam lithography (Vistec EBPG 5000+ system). After development in methyl isobutyl ketone (MIBK)/isopropyl alcohol (IPA) (1:3) and rinsing with IPA, Cr/Au (10 nm/35 nm) was evaporated using electron beam deposition (CHA SEC-600), followed by a liftoff in acetone/IPA. Then, the channel regions (1T′, 2H, 2H/1T′) were patterned and developed using the same method. After development, exposed regions were etched in a 30% H$_2$O$_2$ solution for 5 min, followed by an acetone/IPA rinse. Finally, source and drain contacts were patterned and developed using the same method as above. After development in MIBK/IPA (1:3), Ti/Au (10 nm/80 nm) was evaporated using electron beam deposition (CHA SEC-600) and lifted off in acetone overnight to complete the device fabrication. The sample was finally cleaned with IPA and loaded into a cryogenic vacuum probe station (Lakeshore CPX-VF) for device characterization. No annealing was performed. Electrical measurements were performed in the vacuum probe station at $\sim 10^{-6}$ Torr using a Keysight B1500A semiconductor parameter analyzer.

C.5 Fabrication of *Sequentially*-Grown MoTe$_2$ Homojunction FETs

2H MoTe$_2$ was first grown on Si substrates with 100 nm SiO$_2$ by tellurization of 0.9 nm Mo nanoislands using the flux-controlled synthetic method discussed in Chapter 2.

To pattern alignment markers, PMMA C4 was spin-coated on the substrate at 3000 rpm for 60 s followed by a bake-out at 180 $^{\circ}$C for 8 min. Patterns of alignment markers were written using electron beam lithography (EBL) at 10 nA current and 1300 μC/cm^2 dose followed by a development in 3:1 IPA:MIBK. Then, 130 nm Mo was deposited as the maker metal using electron beam evaporation (EBE) followed by a liftoff in acetone overnight. Channel regions were patterned with PMMA C4 using EBL and the exposed regions were etched in plasma (5 sccm Ar/25 sccm CHF$_3$/6 sccm CF$_4$ with 175 W RF power, 50 mT pressure, and 15 s stabilization time) for 20-30 s. Next, 1.5 nm Mo nanoisland were deposited using conformal evaporation (CHA) for the synthesis of 1T′ MoTe$_2$. The hardened PMMA patterns (by plasma etch) were then lift off in Acetone with 5-10 s sonication. 1T′ MoTe$_2$ was then grown on the substrate using the flux-controlled synthetic method. Since Mo aligned markers were damaged during the synthesis, 10 nm Ti/35 nm Au markers were patterned and deposited on the substrate. Next, channels consisting of pure 2H, 1T′, and back-to-back 1T′/2H/1T′ regions were patterned using EBL and then etched using 30% H$_2$O$_2$. Finally, 10 nm Ti/80 nm Au contact fingers were patterned and deposited using EBL and EBE, respectively.

C.6 Synthesis Details of monolayer 2H-MoS$_2$

200 μg NaCl (through drop casting 40 μL 5 mg/mL NaCl solution) and 5 mg MoO$_3$ (99.5%, Sigma Aldrich) were placed on two 0.5 cm x 0.5 cm SiO$_2$ /Si substrates separately. NaCl and MoO$_3$ were placed 3 cm apart in a 5 cm x 2 cm x 2 cm alumina boat. A 2 cm x 2 cm SiO$_2$ /Sisubstrate was placed face down on the alumina boat contain NaCl and MoO$_3$ at the center of the heating zone in a 3-in. quartz tube (MTI Corporation).

Another alumina boat containing 0.8 g S (99.98%, Sigma-Aldrich) was placed on the upstream side (S was heated to ~150 °C when the furnace reached 730 °C). After the quartz tube was evacuated to < 100 mTorr, Ar flowed at a rate of 500 sccm until the pressure reached atmospheric pressure. At atmospheric pressure, Ar flowed at the rate of 25 sccm. For the synthesis of monolayer 2H-MoS$_2$, the furnace was ramped to 730 °C in 30 min (ramp rate ~ 23.5 °C/min) and was kept at that temperature for 5 min. After the reaction, Ar was turned to the flow rate of 100 sccm and the furnace was rapidly cooled down to room temperature with the furnace lid open.

C.7 Growth of PTCDA on 2D TMDCs

The growth of PTCDA was carried out in a furnace (Fischer/Blue M HTF55347) using a 1-inch quartz tube (MTI Corporation). A quartz crucible (26 mm L x 10 mm W x 8 mm H) containing 30 mg PTCDA powder (97%, Sigma Aldrich) was placed in the center of the heating zone. CVD 2D TMDCs were placed downstream 5 cm away from the center. The quartz tube was evacuated to < 100 mTorr. The source powder was heated to 250 °C in 15 min (linear ramp rates ~ 15°C/min) and was kept at 250 °C for 20 min before cooling down naturally.

C.8 ALD of HfO$_2$

ALD was carried out at 150 °C and base pressure of ~5 Pa using Tetrakis(dimethylamido) hafnium (TDMAH) and H$_2$O as precursors. 20 sccm N$_2$ was used as carrier gas. The pulse/purge time for Hf and H$_2$O precursors were 250 ms/60 s and 100 ms/60 s, respectively.